POLITECNICO DI MILANO

Facoltà di Ingegneria dei Industriale e dell'Informazione

Corso di Laurea Magistrale in Ingegneria Fisica

TOWARDS ON-CHIP CONTROLLED SINGLE CELL DRUG-DELIVERY VIA MAGNETIC NANOPARTICLES

Relatore:

Prof. Riccardo BERTACCO

Correlatore:

Dott.ssa Daniela PETTI

Candidato:

Marco MONTICELLI

matr. 766446

Anno Accademico 2012/2013

Contents

List of Figures

List of Tables

Sommario

Il lavoro di tesi ha riguardato lo sviluppo di una piattaforma "on-chip" che permetta la somministrazione controllata di un farmaco specifico a una cellula bersaglio, attraverso l'impego di nanoparticelle magnetiche come veicoli per trasportare tali farmaci.
Le funzionalita' implementate in questa piattaforma sono essenzialmente due: rilevare, attraverso dei sensori, il passaggio delle nanoparticelle in una cella microfluidica e manipolarle con un' alta risoluzione spaziale verso la cellula bersaglio. Due diversi sensori sono stati utilizzati per questo scopo: i primi sono basati sull' effetto di anistropia magnetoresistiva (AMR), mentre i secondi su una misura impedenziale. La tecnica di manipolazione, chiamata "DWT" (domain walls tweezers) si fonda sull'accoppiamento tra i "bead" magnetici e le pareti di dominio magnetiche che si formano in condotti di Py a causa della peculiare forma geometrica e la cui posizione puo' essere controllata grazie all'applicazione di un campo magnetico esterno. Questo metodo di manipolazione ha attratto un interesse sempre crescente in ambito medico e biologico poiche' le particelle magnetiche vengono, oggigiorno, comunemente impiegate come veicoli (per sostanze biologiche o farmaci) e/o marcatori specifici.
II lavoro sperimentale svolto puo' essere diviso in 3 parti principali:

- Implementazione della tecnologia "DWT", ottenendo una manipolazione controllata e simultanea di un gruppo di nanoparticelle magnetiche su

un chip nanostrutturato dotato di nanocondotti magnetici. La progettazione e la fabbricazione di tali campioni viene inoltre presentata in questo lavoro.

- Fabbricazione, sviluppo e test dei sensori "AMR" e capacitivi, impiegati per rilevare le nanoparticelle magnetiche.

- Somministrazione controllata di nanoparticelle magnetiche ad una cellula bersaglio, facendo uso della tecnologia "DWT". Le nanoparticelle vengono manipolate su chip dotati di "DWT" e ottimizzati per tale scopo.

Il lavoro sperimentale e' stato realizzato sotto la supervisione del Professore Riccardo Bertacco, responsabile del gruppo NaBiS presso il centro LNESS-Dipartimento di Fisica del Politecnico di Milano, Polo Regionale di Como. Una parte degli esperimenti biologici sono stati svolti al "Istituto Farmacologico di Oncologia molecolare" IFOM, a Milano. Hanno collaborato a questo progetto: per la parte che riguarda la fabbricazione dei chip di sensori il gruppo di "litografia elettronica e grafene" del centro LNESS, per la fabbricazione dei DWTs Andrea Cattoni di LPN (Parigi) e per le misure per la detection dei beads il gruppo di "ingegneria elettronica" del Politecnico di Milano.
Questo elaborato di tesi e' organizzato in sei diversi capitoli. Il capitolo 1 tratta del background tecnologico su cui si fonda il lavoro ed in particolare affronta le tematiche della "drug-delivery" e del "Lab-on-chip". Il capitolo 2 descrive i principi fisici su cui si basa la tecnologia DWT e in quale modo viene utilizzata per manipolare le nanoparticelle magnetiche. Il capitolo 3 si occupa delle tecniche e dei metodi sperimentali utilizzati in questo lavoro. Il capitolo 4 descrive la manipolazione di nanoparticelle magnetiche. Nel capitolo 5 vengono descritti i risultati ottenuti sui sensori AMR e capacitivi. Nel capitolo 6 viene illustrata la somministrazione di nanoparticelle magnetiche a

una cellula bersaglio ed, infine, vengono presentate le conclusioni del lavoro.

Abstract

This thesis work deals with the development toward an on-chip platform for achieving a controlled drug-delivery to a target cell via magnetic nanoparticles exploited as drug carriers.
With this platform two main issue are addressed: sensing the magnetic nanoparticles transit in a microfluidic cell and finely manipulating them at the nanoscale to a target cell, in order to deliver a specific drug. The magnetic beads are detected by means of two different sensors based respectively on the Anisotropic Magnetoresisrance effect (AMR) and on an impedantial measurement. The handling method is founded on the coupling of magnetic beads with externally controlled magnetic domain walls and it is called domain walls tweezers (DWT).
This recent manipulation technique has attracted a growing interest in biology and medicine as functionalized magnetic particles are commonly used as molecular and cellular carriers or markers.
The experimental work can be divided in three main parts:

- Implementation of the DWTs technology to achieve a synchronized manipulation of a magnetic nanoparticles batch over magnetically patterned magnetic chip. The design and the fabrication of the employed devices is also described in this work.

- Fabrication, development and test of AMR and capacitive sensors for the detection and transport of magnetic beads.

- Controlled administration of magnetic nanoparticles to a target cell by means of the DWTs technology. The particles are handled over patterned magnetic devices, properly projected and fabricated.

The work has been realized under the supervision of Professor Riccardo Bertacco, responsible for the NaBiS group at the LNESS Center-Dipartimento di Fisica of the Politecnico di Milano, Polo Regionale di Como. A part of the biological experiments have been performed at the "Istituto Farmacologico di Oncologia molecolare" IFOM, in Milan. The fabrication of the sensors has been executed in collaboration with the "e-beam litography and graphene" group of LNESS, while sensor testing and detection measurements have been carried out with the "Electronic engineering" group of the Politecnico di Milano. The fabrication of DWTs chip has been performed in collaboration with Andrea Cattoni of LPN (Paris).
The thesis is organized in 6 sections. In chapter 1, an oveview of the technological background concerning drug-delivery and lab-on-chip devices is illustrated. Chapter 2 discusses the physics principles of the DWT technology and the principles exploited to handle magnetic nanoparticles. Chapter 3 explains the experimental methods which have been employed. In chapter 4, the manipulation of magnetic nanoparticles is described. Chapter 5 explains the results related to the AMR and capacitive sensors. In chapter 6 the controlled administration of nanoparticles to the target cell is illustrated and, finally, the conclusions are presented.

Chapter 1

Introduction and technological background

This thesis work deals with the development of an on-chip magnetic-based platform for achieving a controlled drug-delivery to a single cell by means of magnetic nanoparticles exploited as drug-carries.
The purpose of this chapter is to illustrate the motivations behind the miniaturization of medical and biological addressed devices and the use of magnetism in this context. Moreover, the current state of the art concerning drugs-delivery via nanoparticles is illustrated. Finally, the organization of this thesis and a brief summary of all the chapters is presented.

1.1 Bionanotechnology and nanomedicine

Bionanotechnology is a branch of nanoscience which deals with biological applications of nanotechnologies and with the study of biological entities in the nanometric scale (i.e.1nm-1μm) [1]. It ranges from the biological application of nanomaterials, to the development of nanostructured devices for biological tests (e.g. biosensors), and even to possible future applications of molecular nanotechnologies. The side of bionanotechnology concerning medical appli-

cations is called *nanomedicine*. It has two main goals: understanding how the biological entities inside living cells are organized and operate at the nanoscale, and employing this information to re-engineer these structures and to develop new technologies applications such as diagnostics, diseases treatment and/or damaged tissues repairing.[2].
From an economic point of view, nanomedicine represents now a large industry with at least 3.8 billion of dollars invested in research and development funding every year. In this context this work involves two main branches of nanomedicine:

- the first one concerns the use of nanomaterials for drugs encapsulation and delivery.
- the second one is related to the application of nanotechnology to miniaturized laboratories (Lab-on-chip) performing complex biological operations on minute biological samples quantities.

The following sections will describe the state of the art in these two central topics and will explain in which way they are exploited in the present work.

1.2 Drugs delivery

One of the main problems in contemporary medical science is the invasiveness of many diseases treatment. In particular, the assimilation of a specific drug might potentially produce a large amount of side effects mainly due to the absorption of such drug from the entire organism instead of being localized in the specific area requiring the treatment. Nanomedical approaches to drug delivery focus on developing nanoscale particles and molecules to improve drugs effectiveness while reducing their side effects. Optimization of drug delivery aims to spatially and temporally control the drug release in the body. This can be potentially achieved by modifying and targeting

molecules to specific cells [3],[4] by means of nanoengineered materials. One of the main goal of this research branch is the non-invasive cancer diseases treatment. Because of quantum size effects and large surface to volume ratio, nanoparticles and nanomaterials have unique properties compared with their respective bulk materials. These properties, such as the high chemical and physical reactivity, can be employed to bind specific molecules to the particles surface so that they could interact with target cells. In addition to that, cells usually take up nanoparticles because of their small size with no specific distinction exploiting various bio-chemical mechanisms described in section 1.2.2. However, the toxicity of these materials and the long term effects on the body still remain one of the main issues.

Triggered response is one way for efficient molecules delivery. It can be based on lipid or polymer nanoparticles [5], designed to improve the pharmacological and therapeutic properties of drugs. Moreover, thermo and pH-responsive nanoparticles which react to an environment modification in temperature and pH, by releasing drugs molecules to cells, have been developed in the last years [6] [7].

Nevertheless potential nano-drugs behaviors are difficult to foresee in a very complex and, in some cases, not well-understood environment such as the human body. In this framework new in-vitro tools, mimicking the physiological conditions of the human environment are fundamental for testing the effects of new drug release nanoplatforms and/or new drugs. Many efforts have been done to develop nanocarriers able to mask the drug molecules and selectively release the drug content to the disease site [8]. Although drug encapsulation has been used to reduce the toxicity of many drugs, the low effectiveness in their accumulation in the area of interest still represents the main problem. The dilution and dispersion of the carriers in the bloodstream dramatically reduces their accumulation in the diseased area. Besides passive accumulation mechanisms, active retention mechanisms that rely on the spe-

cific targeting of unhealthy tissues via recognition units at the nanocarrier's surface have been exploited so far [9]. However, there is a strong interest in developing alternative ways to remotely enhance drug accumulation and delivery.
In this framework, magnetic nanoparticles have been widely used. It is due to the possibility to confine them in a certain area, by means of an external magnetic field.

1.2.1 Nanoparticles Transport methods

The integration between medicine, biology and nanotechnologies is often realized by the use of functionalized micro- and nanoparticles. New diagnostic and therapeutic testing procedures, both in-vivo and in-vitro, were introduced by the controlled synthesis and manipulation of such objects, which can be used as carrier for biological systems such as molecules, cells or antigens. Fig.1.1 shows the concept of a functionalized particle, illustrating in a single comprehensive picture the different goals for which it can be employed. Many materials are used for various purposes. For example, quantum dots (QDs) core or gold nanoparticle can be used for nanoimaging, while dielectric or magnetic materials can be employed for manipulation. Polymeric coating is common for surface modification protocols in order to covalently bind biological entities to the particle and thus convey them. By exploiting the intrinsic properties of particles, the handling can be obtained through the application of mechanical, fluidic, optical, electrokinetic and magnetic forces and practically allows for the control and transport of the smaller and inert biological entity. Examples of mechanical manipulators are micro-tweezers for cells [11] or tips of atomic force microscopes, used to position particles [12]. However it is difficult to scale down the size of mechanical manipulators in order to increase the parallel yield of the device.
Moreover in biology non-invasive methods, where there is no contact between

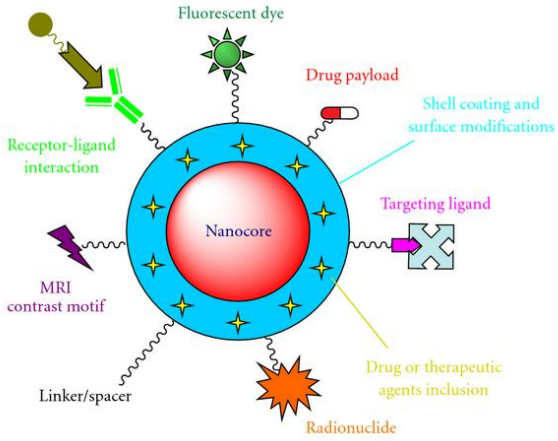

Figure 1.1: Scheme of multifunctional nanoparticle for molecular imaging, drug delivery and therapy. Specifically functionalized and devised nanoparticles can be realized for individualized diagnosis and treatments [10].

the probe and the sample, are preferred. The use of hydrodynamic forces is an example of a non-contact method for cell manipulation. These forces have been exploited successfully in trapping [13] and selecting [14] individual cells. However, these devices require complex pumping and control systems and the high amounts of fluid in the microfluidic channel can induce shear stresses to cells, changing their behavior. Cell manipulation can be accomplished via optical methods, either by radiation pressure [15] or by the force exerted by the gradient of a highly focused laser beam field [17],[16]. Optical tweezers are devices that allow to manipulate particle sizes ranging from tens of micrometers to tens of nanometers. However, the photo-damage to biological entities and the limited area of action impedes the application of these device to highly parallel handling and transport of particles for long paths. Dielectrophoresis (DEP) depends on the force gradient of an electric field rather than an optical one [18]. DEP electrode devices are capable of handling in parallel, but have a limited flexibility; for this reason, it is difficult to isolate

a single particle of interest. Another limitation is induced by the fact that conductive solutions cannot be always used in biology.
The ability of magnets to act on objects at a finite distance makes them valuable medical tools since they represent a non-invasive technique. Magnetism is exploited through the use of magnetic particles to label biological species. The use of phenomena related to magnetism brings several advantages with respect to other techniques. First, magnetic particles are poorly affected by the environment in which are floating and their properties do not depend on the biological molecules which are bound to. Furthermore they are stable over time, because magnetism is usually not affected by reagent chemistry or subject to photo-bleaching (a problem which instead characterizes fluorescent labels). There is also no significant magnetic background present in biological samples and magnetic fields are not screened by aqueous reagents or biomaterials. As an example, once a magnetic functionalized particle is bound to the cellular membrane, it is possible to act indirectly on it in order to measure its mechanical properties or activating ionic channels.
Magnetic particles have a wide range of applications in modern medicine. They can be used to deliver an anticancer drug to a previously targeted tumor region of the body. They also can be engineered to resonantly respond to a time-varying magnetic field in order to transfer energy to the biological target through hyperthermia [19]. In this way the local excess of heat generated induces the death of the tumor cells.

1.2.2 Interaction between nanoparticles and living cells

In the previous chapter different methods to manipulate nanoparticles are illustrated. The next step is understanding the mechanisms of interaction between nanoparticles and cells. In particular, the internalization processes of such nanoparticles by living entities are fundamental to deliver drugs.
Because of the cell membrane has in almost the totality of cases a negative

Zeta-potential, nanoparticle surface can be functionalized with particular chemical groups which produce a positive Zeta-potential that favors the electrical interaction between particle and membrane [20]. The Zeta-potential is the electrical potential in a solution, due to the formation of a double-layer (DL) interface between a charged surface and ions which are electrically attracted. In other words, Zeta-potential is the potential difference between the dispersion medium and the stationary layer of fluid attached to the dispersed particle or cell. Entities with an opposite Zeta-potential are electrically attracted to each other. For this reason, nanoparticles decorated with carbossylic acid ($COOH^-$) are widely used in biological applications.
Moreover a large amount of various ligands are exploited to target specfic cells. For example, folic acid is employed to activate folate receptors (in cancer cells) which promote the uptake of particles functionalized with such acid molecule [21].
In general, there are two main factors for which various uptake mechanisms occur: the nanoparticles size and the stimulations of specific cell receptors in a mechanical or chemical way. Even if the way in which a cell internalizes an external body is still not well known, it is possible to distinguish four major endocytic processes all based on the formation of intracellular vescicles (see Fig.1.2) [22]:

- **Phagocytosis** ('cell eating') It is associated with the formation of big vescicles used to uptake large entities such as bacteria or particles larger than 500nm.

- **Pinocytosis** ('cell drinking') It is used to internalize fluids surrounding the cell through the simoultaneously formation of small vescicles due to the membrane invagination.

- **Endocytosis mediated by clathrin** It is the most important endocytic mechanism involving a receptor (clathrin). It is used to internal-

ize particles that range between 50 and 300 nm, togheter with a large amount of biological nutrients.

- **Endocytosis mediated by caveolae** It is employed to internalize particles up to 100 nm and some virus. It is characterized by caveloine-1 receptors which cover the surface of small invaginations of cellular membrane.

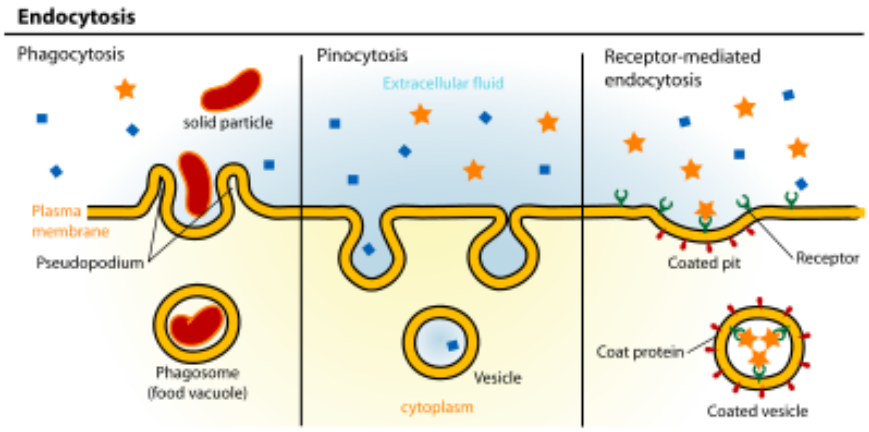

Figure 1.2: Sketch of the main endocytic mechanisms: Phagocytosis, Pinocytosis, Endocytosis mediated by receptors [25].

In literature is possible to find many others receptors-mediated endocytosis that can be employed to internalize specific nanoparticles properly functionalized. Other uptake processes don't involve the formation of vescicles but the cellular membrane is 'penetrated' by small particles. This mechanism is called 'passive uptake' to distinguish it from the first one [23].
Apart from the different uptake mechanisms, another important factor is the uptake rate (i.e. the percentage of particles successfully internalized over the total number of particles in solution). In-vitro experiments show as it strongly depends on the nanoparticles size, concentration and surface coating [24]. It is difficult to find in literature an uptake rate larger than 20% and

it is mainly due to the dispersion of nanoparticles in a liquid environment. The aim of the thesis is to develop a system able to increase such rate by mechanically keep a single nanoparticle in proximity to a target cell exploiting a confined magnetic force. This can be achieved thanks to an on-chip technolgy that will be introduced in the next paragraphs.

1.3 Lab on a chip

In the last two decades, the field of the methodologies applied to the biological and chemical laboratories has been revolutionized by the *miniaturization* processes. In particular, the way in which the research and the analysis are carried out was completely upset by the nanoscience progress.
This trend towards miniaturization began in the second half of twentieth century applied mainly in the field of electronic components and integrated electronics. The driving force for miniaturization is the aim of increasing processing power while reducing the economic cost and environmental impact. Microfabrication technologies were soon applied to other devices, such as pressure sensors and accelerometers, allowing the development of complex microelectromechanical systems (MEMS) and, at the end of the 20th century, devices for chemical and biological analysis: the so called Lab on-Chips (LOCs). Their major feature is the integration of one or several laboratory functions on a single chip of few square centimeters in size. LOCs deal with the handling of extremely small fluid volumes down to less than pico liters. The controlled motion of the fluids, the DNA amplification, drug screening and many others analytical techniques have been miniaturized in LOC platforms. Many of today's applications and possibilities of microfluidic lab on-chip systems have been reviewed by Weigl et al. [26] and more recently by Dittrich et al. [27]. The advantages brought to biology and diagnostics by the miniaturization are mainly related to the following points:

- **Velocity** It has been demonstrated that the size reduction brings advantage when transfers of mass and/or heat are involved. Smaller volumes imply faster heating and cooling cycles, shortening the completion time of a large number of cycles. For example, in the DNA amplification by PCR [30], the operational time has been reduced from several hours to few minutes.

- **Parallelism** Like in the microelectronic industry, the miniaturization can bring to a massive parallelism. The need of increasing parallelism in the discovery of the genomic information has been the major driving force. Lithographic techniques allowed the synthesis of more than 500k samples of DNA on a single chip [28].

- **Low consumption of reagents** Another benefit of the miniaturization is the costs reduction in the pharmaceutical test on the potential effectiveness of certain drugs. This compounds are very expensive and reducing their volume by order of magnitude implies a significant saving.

- **Functional integration** Although the previous point are important, the most interesting opportunity due to the miniaturization is the functional integration. It allows to carry out complex analytical protocols involving several steps or tasks in a faster and cheaper way on the same platform.

Several commercial products already exist in the market like the Agilent LabChip 2100 BioAnalyzer, which uses a lab-on-a-chip approach to perform capillary electrophoresis and a fluorescent dye that binds to RNA to determine both RNA concentration and integrity. The chip format together with the computer for the analysis of the results, dramatically reduces sample consumption but also the time needed for the test. Many application and

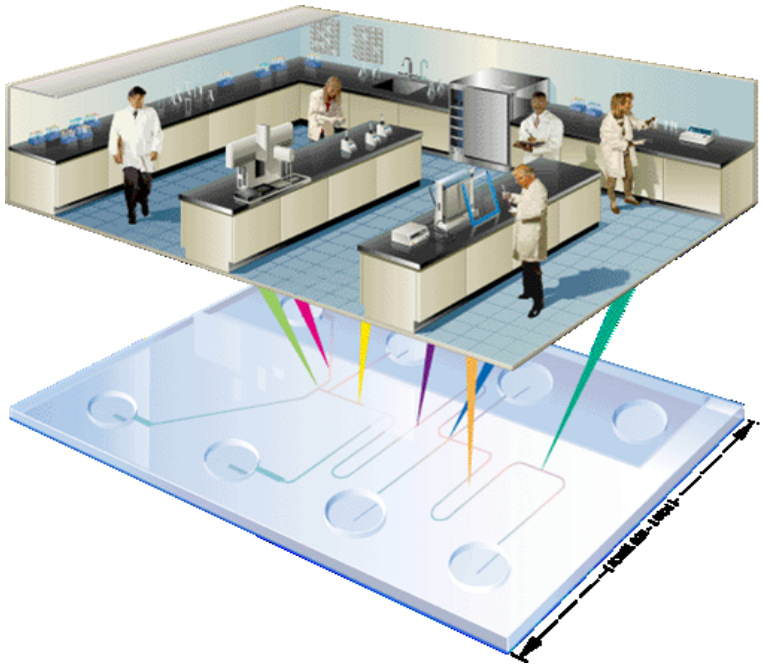

Figure 1.3: Sketch of Laboratory on-chip [29].

different devices can be envisaged in the area of lab-on-chip platforms: Micro total analysis systems (μTAS) are miniaturized and highly integrated chemical analysis systems initially designed in the late 80's [31]. Micro reactors are used for chemical synthesis or energy production. They provide methods to synthesize, on request, unstable, valuable or even dangerous materials. Finally, exploiting physical and chemical properties that are unique for microfluidic systems (e.g. laminar flow and the high surface to volume ratio) complex biological experiments, are indeed possible.

1.3.1 Magnetic based LOC's devices

The integration of microfluidic lab-on-chip devices and magnetic nanoparticles permit a large amount of biological applications that range from sorting target biomolecules in a solution, detecting the presence of a specific molecule

or to manipulate biological entities or cells.

The main commercial use of magnetic manipulators concern the separation of biological species in solution (see Fig.1.4). In this application, magnetic

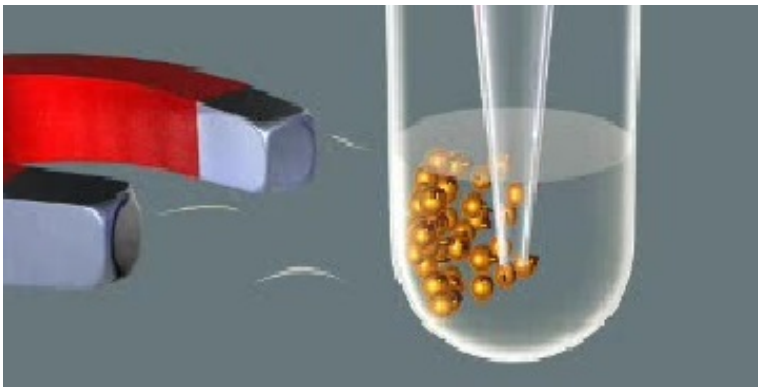

Figure 1.4: Magnetic separation of labelled biomolecules via magnetic nanoparticles.

nanoparticles are decorated with particular probes which bind a specific biomolecule. Exploiting a permanent magnet, an external field is applied to attract nanoparticle so that the concentration of such molecules is increased in a certain region of fluid [32]. However this system doesn't allow a single particle control together with an high parallelism. In order to increase the spatial resolution, a much more confined field has to be applied to trap a target particle. This can be achieved patterning the chip surface with magnetic elements. The joint action of an external magnetic field and the stray field due to the magnetization of such elements, permits to trap the nanoparticles in a confined region. A variation in the direction of the external magnetic field can be employed to manipulate the particles in solution over magnetic structures (Fig.1.5)[33],[34].

The NanoBiotechnology and Spintronics (NaBiS) group of L-NESS Center in collaboration with the Spanish research centre nanoGUNE, has developed a system for trapping and moving magnetic nanoparticles by means

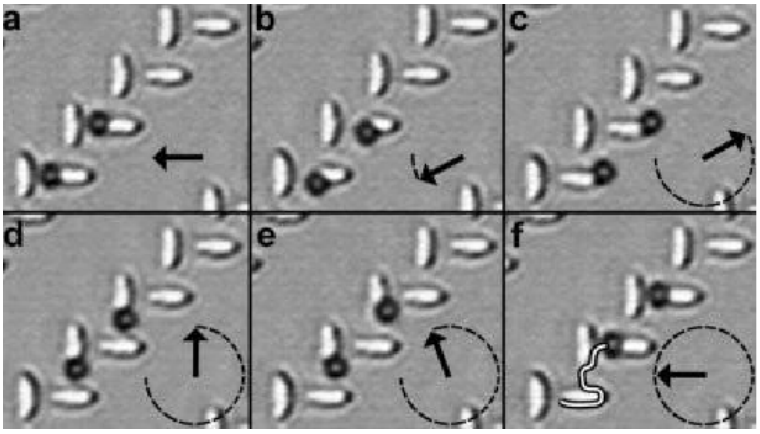

Figure 1.5: Manipulation of 2.8 μm magnetic beads on a staircase pattern of Permalloy ellipses by in-plane 80 Oe rotating magnetic field. The arrows indicate the direction of the field. After one complete field revolution, the beads have moved one step in the pattern as indicated by the white curve in (f)[33].

of *magnetic domain walls* (DWs) confined in magnetic nanostructures [35]. Transverse Neel DW (see chapter 2) generates a considerable stray field that attract a single nanoparticle on the top of the structures. Besides DWs displacement along ferromagnetic conduits applying a proper sequence of magnetic fields, is employed to achieve an high spatial control (down to 100nm) of the nanoparticles which follow the DWs movement. Two different nanostructures geometries are used to this goal: zig-zag and curved structures as illustrated in figure 1.6. This topic will be deeply discussed in the next chapters, considering both the theoretical aspects (Chapter 2), the development and the applications of this technology (Chapter 3,4,5 and 6).
Another fundamental application of LOC devices is to detect and record the presence of biomolecules in solution. A large amount of high resolution and miniaturize sensors for this purpose can be found in literature [37]. In particular, sensors which combine electrical and magnetic properties such

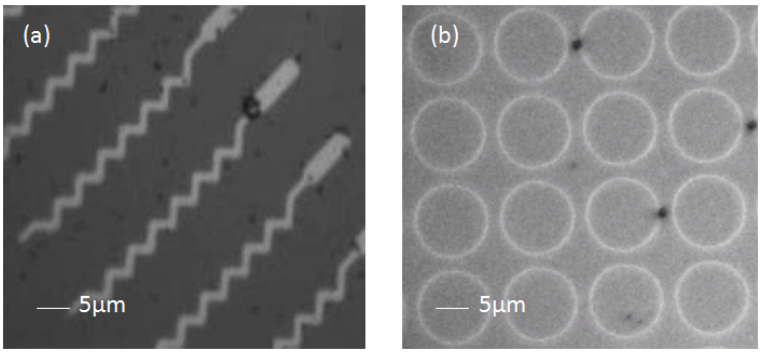

Figure 1.6: Ferromagnetic conduits geometries: zig-zag shaped (a) and curved (b) structures.

as giant-magnetic resistance (GMR), tunneling-magnetic resistance (TMR), anisotropic magnetic resistance (AMR) and hall-effect are widely employed in nanomedicine [38],[39],[41],[40]. In this work, in order to exploit magnetic nanoparticles properties, not only as biomolecules carriers, but also as labels, two different MNPs detection paradigms have been developed:

- **Anisotropic-magnetic resistance based sensors** This system is able to electrically detect the crossing of a DW between two micro electrical contacts by an electrical signal variation through a magnetoresistive effect. The presence of a MNP on the top of a DW is detected, because of it induces a variation of the depinning field (the minimum field required to displace the DW) that can be recorded.

- **Electrical sensors based on impedance measurements** A particle driven between two micro-electrical contacts in a buffer solution produces a voltage drop due to the high impedance of such nanoparticle that can be detected by a capacitance measurement.

A full analysis of the working principle, fabrication and application of such sensors is illustrated in chapters 2,3,5.

1.4 Thesis outlook

The aim of this thesis is to develop an innovative on-chip platform for drugs-delivery through magnetic nanoparticles. This technology permits the controlled administration of a single particle to a target cell by means of magnetic tweezers based on magnetic DWs, briefly introduced in section 1.2.2. Superparamagnetic nanoparticles are injected in a microfluidic cell and their flow in a channel is magnetically activated via the manipulation of DWs in magnetic conduits. The passage along the channel is then detected by a sensor (AMR or impedance-variation based). Then, particles are trapped and manipulated to an area of chip where living cells are cultured, studying the interaction between a single particle and cell. The final goal is to observe a particle uptake in order to complete the vehiculation of the drug inside cell membrane.
Despite the complexity of the presented work, involving different area of knowledge and competences, some relevant progress have been done during this thesis. In particular the activation and detection of the passage of the bead over a magnetic conduit has been demonstrated. Furthermore preliminary experiments of cellular uptake have been carried out. The experimental activity has been performed mainly in the L-NESS laboratory under the supervision of Prof. Riccardo Bertacco. The sensors development has been performed in collaboration with the 'Electronic engineering' group of 'Politecnico di Milano' leaded by Prof. Marco Sampietro. The biological part of this work has been carried out in collaboration with 'IFOM' (Istituto Farmacologico di Oncologia Molecolare) and 'Istituto farmacologico Mario Negri'.
Here an overview of each chapter is presented:

- **Chapter 1: Introduction and scientific background** This chapter gives a brief description of the scientific background and a summary of

this thesis work.

- **Chapter 2: Micromagnetics and magnetic nanoparticles** In this chapter the theoretical aspects such as the physics and the working principles of magnetic nanostructures are illustrated. Besides, a description of magnetic nanoparticles behavior and the interaction of such particles with DWs is provided, together with an explanation of the AMR effect.

- **Chapter 3: Experimental methods** This chapter shows the experimental techniques used in this work. The fabrication of devices, the simulations performed to optimize the working conditions, the characterization techniques, the different setups used for measurements and tests are presented here.

- **Chapter 4: Movimentation of nanoparticles over magnetic conduits** The manipulation of magnetic nanoparticles over thin film nanostructure is presented here. The first part is a description of a single-particle manipulation on zig-zag shaped and curved structures. In the second part, the simultaneous motion of a nanoparticle batch over curved conduits is illustrated.

- **Chapter 5: Detection methods of magnetic nanoparticles** In this chapter the detection and counting of MNPs exploiting two different sensors, based on AMR and electrical impedance, is described.

- **Chapter 6: Controlled administration of nanoparticles to a single cell** This chapter deals with the use of magnetic manipulation system described in Chapter 4 to bring a single magnetic nanoparticles in proximity of a living cell, studying the interaction between particles and cells as fundamental aspect of drug-delivery.

- **Conclusions and Perspectives** This section summarizes the conclusions of this thesis and outlines the future perspectives.

Chapter 2

Micromagnetics and magnetic nanoparticles

The behavior and the properties of a magnetic material are described by the relation between the magnetization vector and the magnetic field $\mathbf{M(H)}$. The calculation of this parameter is a complex matter because there are several physics phenomena that compete to determine what is the magnetic configuration for a certain material. This chapter has the goal to describe these different contributions through simple equations and parameters which are basic to explain the behavior of a magnetic body. The knowledge of these parameters allows to foresee the behavior of nanostructured magnetic materials and thus to properly design the devices employed in this thesis work.
The first part of the chapter deals with the existence of magnetic domains with a focus on magnetic domain walls (DW) confined in nanostructures. In the second part, instead, a second ingredient of the employed manipulation methods will be discussed: the superparamagnetic beads and their interaction with the DWs stray field. Finally, the anisotropic magnetic resistance effect exploits in AMR sensors will be described.

2.1 Micromagnetism

The main mechanisms leading the formation of the different magnetic configurations are *exchange interaction, magnetic anisotropy, magnetostatic self energy* (due to dipole-dipole interaction) and *Zeeman Energy*.
In a thermodynamic approach, the most stable configuration of $\mathbf{M}$ arises from the minimization of a Free Energy functional which include all the contributions listed before. Domains formation helps to minimize the energy in most cases. The main issue of this approach is that each energy term (in particular exchange and anisotropy) depends on the atomic structures of materials, consequently the energy minimization has to be calculated in an infinite dimensional space including infinite spatial coordinates. This approach belongs to the theoretical framework of *micromagnetism*. It is based on the idea that a magnetic body can be divided into small volume elements ΔV in which the value of Magnetization vector $\mathbf{M}$ can be considered uniform. These partitions of the volume are small compared to the characteristic length of variation of the magnetization, but they are big enough so that thermodynamics and statistics rules can be applied. Free Energy in micromagnetic theory is expressed in the *continuum approximation*, where atomic structure is averaged away and $\mathbf{M(r)}$ is a smoothly varying function. Morover, another assumption of micromagnetism is that the relaxation time for which a single volume element ΔV reaches the thermal equilibrium is much shorter than the relaxation time for the whole system.
The micromagnetism history starts in 1935 with a paper of Landau and Lifschitz on the structure of the wall between two antiparallel domains. William Fuller Brown gave this theory the name *micromagnetism* in 1963 to distinguish it from *Domain theory* which considers domains but neglects walls.
In the following sections there will be a description of all the physics mechanisms that lead magnetization in a magnetic material.

2.1.1 Exchange Interaction

The *exchange energy*, which is the base of ferromagnetism, is a quantum mechanic effect concerning the spin-spin interaction. It favors the parallel (ferromagnetic) or antiparallel (antiferromagnetic) orientation of spins along interatomic distances. It can be expressed by the *Heisenberg Hamiltonian*:

$$H_{exchange} = -\sum_{i=j=1}^{N} J_{ij}\mathbf{S}_i \cdot \mathbf{S}_j \tag{2.1}$$

where $\mathbf{S}_i$ is the spin angular moment related to an ion located in position i in a certain lattice and the exchange parameter J_{ij} gives information on the strengthness of the interaction between spins i and j. The exchange interaction decreases quickly with the interatomic distance, so that the exchange energy can be calculated considering only the first neighboring atoms.
Considering spin operators as classical vectors, it can be written:

$$E_{exchange} = -JS^2 \sum_{i=j=1}^{N} cos\phi_{ij} \tag{2.2}$$

where ϕ_{ij} is the angle between two classical spins vectors and J is considered uniform for all the coupled spins in a lattice (taking into account only the first neighbors). The angle between neighbors spins is usually very small, consequently, the cosine function can be written as a Taylor sum and the equation 2.2 becomes:

$$E_{exchange} = \frac{1}{2}JS^2 \sum_{i=j=1}^{N} \phi_{ij}^2 \tag{2.3}$$

The zero point energy of exchange energy is removed neglecting the constant term of cosine expansion. Equation 2.3 can be usually expressed in another form adopting the unitary magnetic moment $\mathbf{m} = \mathbf{M}/M_s$. For small angles $|\phi_{ij}| = |\mathbf{m}_i - \mathbf{m}_j| = |(\mathbf{r}_{ij} \cdot \nabla)m|$ where $\mathbf{r}_{ij}$ is the vectorial distance between ions in position i and j. In this way the 2.3 becomes:

$$E_{exchange} = -JS^2 \sum_{i,j}^{N} \sum_{\mathbf{r}_{ij}} [(\mathbf{r}_{ij} \cdot \nabla)m]^2 \tag{2.4}$$

Substituting the sum with an integral on small volume portions, equation 2.4 can be written as follow:

$$E_{exchange} = \int_V A[(\nabla m_x)^2 + (\nabla m_y)^2 + (\nabla m_z)^2]dV \tag{2.5}$$

It is the proper form of free energy term due to exchange. A [J/m] is the exchange constant defined by:

$$A = \frac{2JS^2c}{a} \tag{2.6}$$

where a is the lattice parameter and c is an integer depending on the crystalline structure of a body. For example, it is 1 for a cubic lattice, 2 for a BCC lattice and 4 for a FCC structure. From the exchange energy contribution we can derive the most important length scale in micromagnetism: the exchange length l_{ex}.

$$l_{ex} = \sqrt{\frac{A}{\mu_0 M_s^2}} \tag{2.7}$$

It represents the distance over which the magnetization can twist by considering only exchange and magnetostatic interaction, while neglecting magnetic anisotropies. It gives also the boundary between "small" objects with uniform magnetization (single domain state) and "large" objects which tends to develop a complex and non-uniform magnetization (multi-domain). Furthermore, the size of the cells ΔV in which the structure is divided should be smaller than l_{ex} in order to consider magnetization constant inside each cell.

2.1.2 Magnetic Anisotropy Energy

Magnetic anistropy is the tendency for magnetization in a ferromagnet or antiferromagnet to lie along preferred directions, called *easy axis*. If the magnetization of a certain body is oriented along another direction an energy penality has to be considered in the total free energy (which is exactly

the work to align M with a direction different from an easy one). As discussed before, considering an uniform value of magnetization ($\mathbf{M} = M_s\mathbf{m}$) in each small volume portion, it is possible to write an expression of anisotropy energy density $e_{AN}(\mathbf{m})$ as a series of trigonometric functions:

$$e_{AN} = K_0 + K_1 sin^2\theta + K_2 sin^4\theta \tag{2.8}$$

where θ is the angle between $\mathbf{M}$ and the anisotropy axis. K_0, K_1, K_2 have the unit of J·m^{-3} Values for K_1 may range from less than 1 kJm^{-3} to 30 MJm^{-3}. It depends on temperature and must tend to zero at the Curie temperature T_C.

This expression is valid only for an uniaxial anisotropy. There are different expressions of anisotropy energy in different symmetries (depending on the atomic lattice geometry) which can be found in literature.

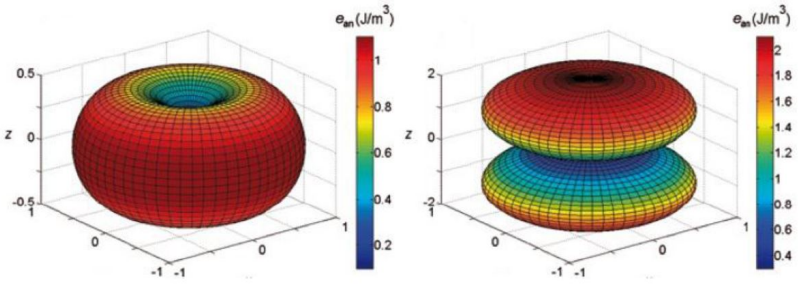

Figure 2.1: Uniaxial anisotropic energy density. (left) Anisotropy with easy axis (K1 $>$ 1). (right) Anisotropy with easy plane (K1 $<$ 1).

K_1 can be bigger or smaller than zero. In the first case there will be a preferred (easy) axis for magnetization, in the second one a preferred (easy) plane (see Fig. 2.1).

For small values of θ (small angle between magnetization and easy direction),

equation (2.8) becomes:

$$e_{AN}(\mathbf{m}) = 2K_1 sin^2\theta - \mu_0 M \cdot \mathbf{H}_{AN} \tag{2.9}$$

where H_{AN} is the anisotropy field defined as follow:

$$H_{AN} = \frac{2K_1}{\mu_0 M_S} \tag{2.10}$$

It is not a real field but simply a parameter which measures the strengthness of the anisotropic effect.

In order to write an equation for the entire body an integration on the total volume has to be performed:

$$E_{AN} = \int_V e_{AN}(\mathbf{m}) dV \tag{2.11}$$

In a three dimensional picture, easy directions are related to minima of anisotropy energy density function instead maxima and saddle points are associated with hard and medium axis.

So far, magnetic anisotropy has been treated without considering what is the origin of the phenomenon. There are two main sources of anisotropy related to sample shape and crystalline structure.

Magnetocrystalline Anisotropy

Magnetocrystalline anisotropy is an intrinsic property due to the fact that the magnetization process is different when the field is applied along different crystallographic directions because the anisotropy reflects the crystal symmetry. Its origin is in the crystal field interaction and in the spin-orbit coupling. There are two different mechanisms which drive magnetocrystalline anisotropy: *single ion contributions* and *two ions contributions*

Single ion anisotropy is essentially due to the electrostatic interaction of the orbitals containing the electrons responsible of magnetism with the potential create at the atomic site by the rest of the crystal. The crystal field interaction tends to stabilize a particular orbital, and by spin-orbit

interaction, the magnetic moment is aligned in a particular crystallographic direction. In a ferromagnetic crystal the contributions of all ions are summed producing a macroscopic effect.

Two ions anisotropy reflects the anisotropy of the dipole-dipole interaction. Comparing the broadside and head-to-tail configurations of two dipoles, each with moment **m**, the head-to-tail configuration is lower in energy (magnets tend to align head-to-tail). However, the dipole sum has to be extended over the entire lattice, and it vanishes for certain lattices (including all the cubic lattices). In noncubic lattices, the dipole interaction is an appreciable source of ferromagnetic anisotropy.

Shape Anisotropy

This phenomenon is strictly related to the geometry of the body. The origin of the *shape anisotropy* is the magnetostatic energy, in particular it arises from the demagnetizing field at which the self-energy of the body is associated. In order to minimize the magnetostatic energy, magnetization pointing perpendicular to the surface is not favored in thin films because an high energetic cost should be paid. In the nanoworld this contribution is often fundamental to drive the magnetic configurations.

2.1.3 Magnetostatic and Zeeman Energy

Magnetostatic Energy is defined as the mechanical work required to bring all the magnetic moments forming the body from the infinity to their final positions, so as to form the macroscopic material. It is essentially due to dipole-dipole interactions. Compared to exchange, magnetostatic interactions are long range ones.

Considering a magnetic body in a certain region of space, it obeys to Maxwell

equations so that in absence of currents:

$$\nabla \times \mathbf{H} = 0 \tag{2.12}$$

$\mathbf{H}$ is the field induced by the magnetization of the body. From 2.12 is possible to write:

$$\mathbf{H} = -\nabla U \tag{2.13}$$

where U is *magnetostatic potential*. Introducing the fundamental relation $\mathbf{B} = \mu_0(\mathbf{H} + \gamma_B \mathbf{M})$ (where γ_B is the Brown constant, equal to 1 for the "international system of units" -S.I.-) and remembering that $\mathbf{B}$ is a divergenceless field ($\nabla \cdot \mathbf{B} = 0$), it is possible to obtain the following expression:

$$\nabla^2 U = \gamma_B \mathbf{M} \tag{2.14}$$

The last equation is different to zero only inside the magnetic material ($\mathbf{M} \neq 0$). From the previous expressions is possible to obtain the following boarding conditions:

$$U_{int} = U_{ext} \tag{2.15}$$

and

$$\frac{\partial U_{int}}{\partial n} - \frac{\partial U_{est}}{\partial n} = \gamma_B \mathbf{M} \cdot \mathbf{n} \tag{2.16}$$

in which $\mathbf{n}$ is the direction perpendicular to the surface. The solution of 2.14 is unique with the adequate conditions and it is possible to demonstrate the following expression for the magnetostatic energy:

$$U = E_{magstat} = -\frac{1}{2} \int_{\Omega} \mathbf{M} \cdot \mathbf{H}_d d\Omega \tag{2.17}$$

where the integration is over the whole magnetic material. $\mathbf{H}_d$ is the *demagnetizing field* induced by magnetization and defined as follow:

$$\mathbf{H}_d = -N\mathbf{M} \tag{2.18}$$

N is the shape dependent demagnetizing tensor. Equation 2.17 represents the so called "self-energy" because is the energy associated to a magnetic body

in absence of an applied field and in a static condition. When an external magnetic field is applied, the magnetic moment will try to reduce its energy by aligning itself parallel to it. The energy that describes the interaction of a magnetic moment with an external field $\mathbf{H}_a$ is called *Zeeman energy* and it is given by the following relation:

$$F_{Zeeman} = \int_V \mathbf{H}_a \cdot \mathbf{M} dV \tag{2.19}$$

It is a long range interaction.

2.1.4 Magnetic domains

In 1906 Weiss first identified the presence in magnetic materials of small regions, called domains, where the Magnetization is almost uniform and the orientation of $\mathbf{M}$ varies from one domain to another [42]. Domains are separated by domain walls. However Weiss didn't properly explain why domains exist. In 1935 Landau and Lifshitz showed that domains formation is the consequence of minimization of the total free energy functional (E_{TOT}) of a magnetic system [43], which gives rise to the different magnetization configurations. E_{TOT} can be written by adding up the energy contributions arising from the exchange coupling, magnetocrystalline anisotropy energy, demagnetization and the external field as:

$$\begin{aligned} E_{TOT} = \int_V \{A[(\nabla m_x)^2 + (\nabla m_y)^2 + (\nabla m_z)^2] + \\ + e_{AN} - \frac{1}{2}\mu_0 M_S \mathbf{m} \cdot \mathbf{H}_d - \mu_0 M_S \mathbf{m} \cdot \mathbf{H}_a\} dV \end{aligned} \tag{2.20}$$

where $\mathbf{m}$ is the magnetic moment, H_d and H_a are respectively the demagnetizing field and the external magnetic field and $\mathbf{M}$ is expressed as $\mathrm{M}_S\mathbf{m}$. As mentioned before, the local energy minima correspond to the metastable states of the system. Therefore, the existence of domains is the result of the combination of all the energy terms that appear in this functional.

The exchange energy favors the parallel allignment of $\mathbf{m}$ throughout the

whole volume. The direction of **m** is not important for such contribution, but each configuration in which **m** spatially varies costs in terms of energy. The magnetocrystalline anisotropy promotes local alignment of **m** with easy axis or planes within the material. This means that an energy cost has to be paid if **m** is not directed in that way. Moreover, the magnetostatic energy favors any configurations in which magnetization follows close paths inside the object in order to minimize the stray field outside. This fact can be in competition with requirements for lowering the exchange energy and the anisotropic energy contribution. A parameter to evaluate the relative importance of the magnetostatic interaction respect to the anisotropic term is:

$$k_{M-A} = \frac{2K_1}{\mu_0 M_S} \tag{2.21}$$

Generally, the magnetostatic contribution leads in isotropic materials where $k_{M-A} \gg 1$. Instead, the anisotropic energy is the dominant term in crystalline material where $k_{M-A} \ll 1$.

The break up of magnetization in localized regions which provides for flux closure at the ends of the specimen, is mainly due to the need of minimizing the magnetostatic energy. On the other hand, a large number of domains are associated to a large number of *domain walls* (region between two neighboring domains) that implies an exchange energy cost.

As an example, figure 2.2 shows three different configurations for the domain structure in a ferromagnetic sample. The single domain structure (a) has no domain walls, but has a large dipolar energy because the magnetic moments are directed perpendicular to two edges of the object. The dipolar energy can be reduced by the formation of different antiparallel domains (b). The so-called closure domain structure (c) eliminates the dipolar energy, since there are no "magnetic charges" on the edges, but introduces a larger number of domain walls.

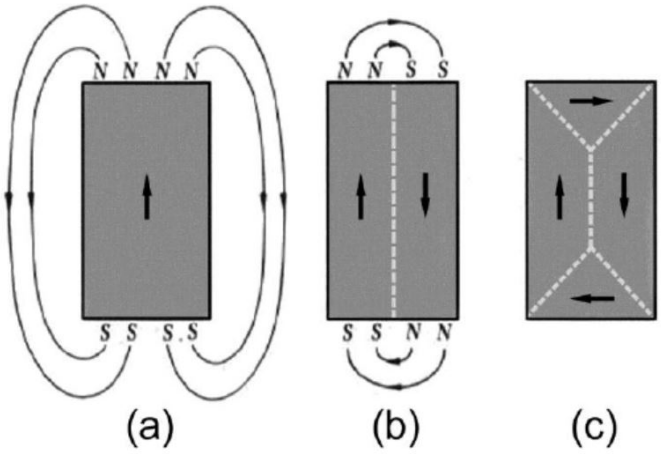

Figure 2.2: Domain formation: from left to right the magnetostatic energy is decreased due to domains creation [44].

2.1.5 Domain walls

In order to create domains, a certain work has to be performed against exchange interaction which would favor spin alignment. To limit this energetic penalty *domain walls* (DWs) exist. DW is a region between two magnetic domains where the magnetization changes gradually from one direction to another. This is true since the exchange energy, as explained in section 2.1.1, is a short range term. Considering a piece of material with two domains, where the orientation of magnetization is in opposite directions (see Fig. 2.2(b), there is not a substantial variation of anisotropic energy if the two antiparallel domains are aligned along the uniaxial anisotropy easy axis compared to the single domain case (Fig. 2.2(a)).

Anisotropy tends to form thin walls (where only few spins are not aligned to the easy axis), while the exchange interaction promotes thicker walls. The more gradual is the angle variation between spins, the lower is the exchange energy cost.

Depending on the spin rotation across the wall, two main types of domain

walls can be distinguished: Bloch and Neel wall. In a Bloch wall, the spins rotate in a plane perpendicular to the domain wall plane. In a Neel wall the spins rotate in the domain wall plane. Both types are illustrated in figure 2.3. The former one is promoted in bulk samples. The Neel wall is instead favored when thin films are considered, since it removes the magnetostatic energy cost due to spins pointing out of the film plane. The contribution of magnetic poles on the two surfaces is eliminated, but the configuration of the elementary magnetic moments inside the wall creates an additional stray field.

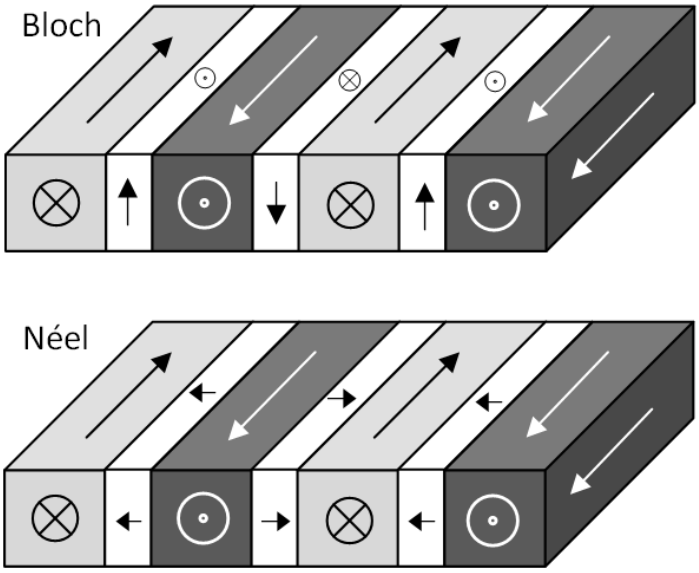

Figure 2.3: Two domain wall types, Bloch wall (above) and Neel wall (below).

2.1.6 Neel domain walls in thin film materials

In thin films, the magnetic configuration is not only determined by the intrinsic material properties but also the morphology and geometrical shape plays a fundamental role. This is particularly true for soft magnetic material in which the magnetocrystalline anisotropic energy is negligible and the

equilibrium magnetic state is related essentially to the geometric shape. This permits to properly fix the magnetic configuration and the magnetization reversal by choosing the morphology and the applied external field.
It is due to the fact that, in soft magnetic nanostructures, the magnetostatic energy promotes the alignment of magnetization along the edges of the structures, in order to minimize the stray field.
In elongated elements, such as stripes or conduits, the magnetization is aligned to the long axis and this mono-domain state is very often the lowest energy magnetic state. In multi-domain configurations, instead, domain walls (DWs) are created, forming mobile interfaces that separate regions with opposite magnetization. Two spin structures can be found, classified as Neel wall variants: the transverse DW and the vortex DW, shown in figure 2.4(a). A DW can be either head-to-head (HH) or tail-to-tail (TT), if the magnetization is pointing towards or away from the wall. As an example, in figure 2.4(a) both the configuration are HH. In the transverse DW, spins rotate in the plane of the structure, from one domain to the adjacent one. The vortex wall shows a completely different configuration. The spins rotates clockwise or counterclockwise around the vortex core where the magnetization points out of plane. The energy of the two configurations varies with the dimensions of the stripes and with the material used. The phase diagram between the transverse and vortex state was calculated by McMichael et al. [45]
They considered only the magnetostatic and exchange energy terms for a patterned stripe of Permalloy of thickness t and width w coming to the equation:

$$wt = const \cdot \delta^2 \tag{2.22}$$

The results, expressed as function of the dimensionless variables t/δ and w/δ, where $\delta = l_{ex}/2$, are shown in figure 2.4(b).The graph shows that for relative thin and narrow geometries, the transverse wall is preferred, whereas the vortex wall is favored in thicker and wider stripes. For example, in a

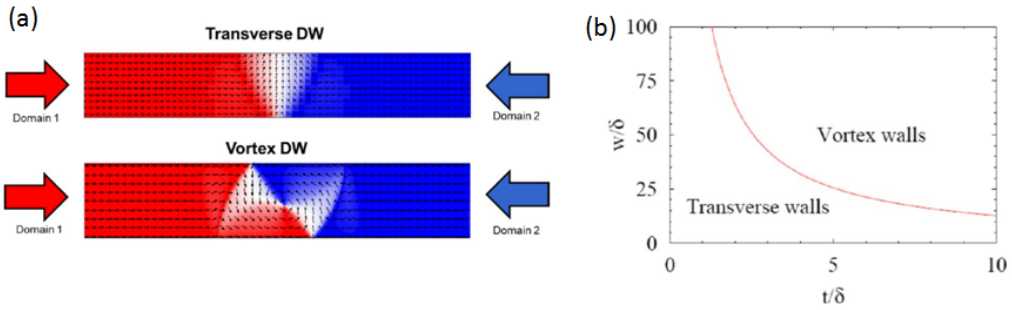

Figure 2.4: Top view of a Permalloy infinitely long strip with two opposite domains (red and blue arrows) and a DW which divides the two regions. Both transverse spin structure and vortex spin structure DW are shown (a). Phase diagram of a transverse HH DW in thin magnetic stripe. δ is equal to $l_{ex}/2$ (b) [45].

Permalloy conduit 20 nm thick the transverse wall is favored for width under 200 nm.

2.1.7 Pinning and propagation of Domain walls

In this section, the quasi-particle approach to describe the DW behavior will be presented. As discussed in the previous sections, the particular spin configuration of the DW is the result of the energy minimization process. The terms, involved in the process, do not only depend on the material but also on its shape and on the external magnetic fields. Shape variations change the potential landscape that a DW feels. By using different geometries we are able to engineer well-defined attractive potentials which acts as stable positions for DWs. Moreover, such potential landscape can be modified by applying external magnetic field, so that equilibrium stable positions depend both on geometry and on the applied field. Intuitively, DWs should achieve an energy minimum in positions where the wall is small, since, in first approx-

imation, the DW energy scales with its dimension . Thus the DW nucleation is energetically favored in constriction and in narrowed conduits. A constriction pins a DW, generating an attractive potential well. Every well is characterized by a characteristic length and depth. The depth is related to the magnetic field intensity needed to push the DW out of the constriction and move it to a new stable position, or annihilate it. An example of relevant pinning sites for DWs are corners. Figure 2.5 shows the transverse DW configuration in a corner and the potential well generated by this geometry.

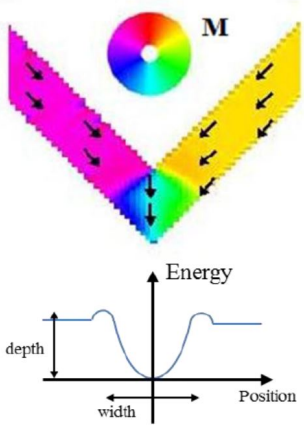

Figure 2.5: Simulated behavior of a transverse DW at a corner site. The figure shows the magnetization structure of the DW and below the sketch of the potential well, whose minimum is centered on the tip of the corner.

The magnetization and DW dynamics are described by the Gilbert equation:

$$\frac{\partial \mathbf{M}}{\partial t} = \gamma \mathbf{M} \times \mathbf{H}_{eff} - \alpha\gamma \mathbf{M} \times \frac{\partial \mathbf{M}}{\partial t} \tag{2.23}$$

where γ is the electron gyromagnetic ratio, α is the experimental damping coefficient and H_{eff} is the effective field. It is a fictitious magnetic field that takes into account all the energetic contributions: the external and mag-

netostatic field, but also the exchange interaction and the anisotropy. The effective field exerts a torque to the magnetization vector. The first term describes a pure gyroscopic effect. If $\mathbf{M}$ is not at the equilibrium, it will start to precede continuously around the field without reaching the equilibrium. The second term, experimentally introduced, takes into account the dissipative effects. The thermodynamic forces lead $\mathbf{M}$ to the equilibrium. Similarly to the viscous forces, the damping term is proportional to the temporal variation of the quantity of interest, in this case the magnetization.
When an external magnetic field is applied to the system, the DW feels a change in the potential landscape. If the field intensity is high enough to overcome the local pinning site, the DW will propagate towards the new equilibrium position. The propagation process of a transversal DWs along a conduit has been studied by Walker and Schryer [46]. They found that the DW moves with a velocity v:

$$\mathbf{v} = \frac{\gamma\Delta}{\alpha} \cdot \mathbf{H} \tag{2.24}$$

where Δ is the DW length. The velocity is thus proportional to the applied field. The relationship is valid until a critical field, called Walker field $\mathbf{H}_W$, is reached. Above this field the DW magnetic configuration is transformed and it reduces the wall velocity.

2.2 Magnetic micro and nanoparticles

In this section, the magnetic particles and their interaction with magnetic fields in a liquid environment will be described.
Many properties of magnetic materials can be explained by their volume magnetic susceptibility χ, which describes the magnetic response, i.e. its magnetization, to an applied field: $\mathbf{M} = \chi\mathbf{H}$. In presence of a magnetic

material the total flux density **B** results to be:

$$B = \mu_0(\mathbf{M} + \mathbf{H}) = \mu_0(1 + \chi)\mathbf{H} = \mu_0\mu_r\mathbf{H} \tag{2.25}$$

where μ_0 is the permeability constant in vacuum and μ_r the relative permeability of the material. Depending on the interaction of the solid material with an external magnetic field, various types of magnetic behaviour can be distinguished, such as diamagnetism (μ_r <1), paramagnetism (μ_r >1), ferromagnetism ($\mu_r \gg 1$).

When the size of a magnetic object is reduced below a certain dimension, as in the case of nanoparticles, a different magnetic effect can arise. It is called *superparamagnetism*, corresponding to the situation in which each particle behaves as a macrospin (where spins are ferromagnetically aligned) fluctuating in an external field as in the case of magnetic moments within a paramagnet.

Considering a magnetic spherical particle of volume V with an uniaxial anisotropy and two possible magnetization states: parallel or antiparallel to the easy axis. They are separated by an energy barrier proportional to the anisotropy constant K_1 of the material and to the volume V. If the activation energy (K_1V) for flipping the magnetization from parallel to antiparallel is small compared to the thermal energy k_BT, where k_B is the Boltzmann constant, the magnetization is continuously inverted by thermal fluctuations. The average time between two thermally activated transitions is given by:

$$\tau = \tau_0 exp(\frac{k_1 V}{k_B T}) \tag{2.26}$$

where τ_0 ranges 10^{-9} 10^{-11} s for isolated particles and T is the absolute temperature. By reducing the particle size, the energy barrier K_1V decreases and, inversely, the flipping rate increases. Superparamagnetism is a size effect that depends both on the temperature T and on the observation time t. A magnetic particle appears blocked, i.e. ferromagnetic, if the observation

time t is much smaller than τ. Above the blocking temperature, defined as the temperature at which τ is equal to the measuring time, the particles behave as a superparamagnet. At room temperature the typical diameter of a superparamagnetic particle is in the range from 5 to 128 nm [47].The superparamagnetic state provides to nanoparticles high saturation magnetization M_S, comparable to those of ferromagnets, and no remanence M_R as a paramagnet. Those properties make them suitable for different biological applications. The magnetic behavior of such superparamagnetic particles can be described through the Langevin function ($L(x) = cot(x) - 1/x$) so that:

$$\mathbf{M}(H) = mL(\frac{\mu_0 mH}{k_B T}) \tag{2.27}$$

where m is the magnetic moment of the particle.

A typical nanoparticle is formed by a superparamagnetic core surrounded by a nonmagnetic coating. The last one is necessary to form selective bonds with biomaterials of interest. Standard particles have a total diameter between 5 and 50 nm. Iron oxides such as magnetite (Fe_3O_4) or maghemite (Fe_2O_3) are employed for the core because they are biocompatible and potentially non-toxic for biological entities.

In order to maintain the properties of superparamagnetic particles, but achieving a greater volume and magnetic moment, larger magnetic bead (0.1 to 5 μm in diameter) have been introduced. They are obtained by embedding several superparamagnetic nanoparticles, not magnetically interacting, in a non-magnetic matrix. A sketch of a magnetic bead made by superparamagnetic particles core in a polymeric shell is illustrated in figure 2.6. In this thesis work, three main different types of commercial superparamagnetic beads are employed. *Dynabead My-One* (Invitrogen) are widely used for the experiments described in chapter 4 and 5. They have a diameter of 1 μm and they are functionalized with COOH. In chapter 6 *nanomag-CLD-redF* (Nanomag) particles are employed. They have a diameter of 300 nm and are functionalized with COOH. The latter are also covered by a TRITC red

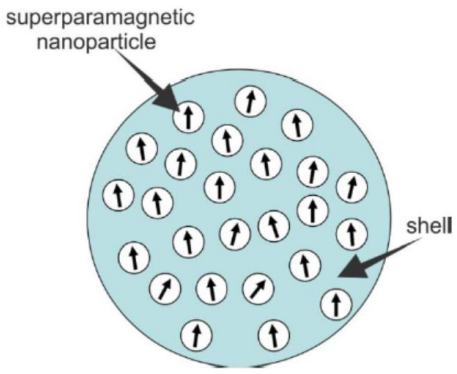

Figure 2.6: Sketch of magnetic bead formed by magnetic nanoparticles in a non-magnetic matrix/shell.

fluorescent marker to get images in fluorescence. In chapter 5, micromer-M-Streptadivin (Nanomag) particles are also used to test capacitive sensors. They have a diameter of 2 μm and are fuctionalized with the Streptavidin protein. COOH and Streptavidin functionalizations are highly hydrophillic and, consequently, they are suitable for experiments in wet environments. Moreover, they offer a low non-specific binding, excellent dispersion abilities and easy handling in a wide variety of buffers.

2.2.1 Interaction forces on magnetic beads

To understand how the magnetic field can be used to transport and manipulate magnetic beads it is important to know which forces act on a particle suspended in a fluid. In all the experiments magnetic bead are subjected to gravity forces, to the viscous force and magnetic force.
The buoyancy force $\mathbf{F}_b$ opposes to the gravity force $\mathbf{F}_g$ giving a net contribution expressed by:

$$\mathbf{F}_g - \mathbf{F}_b = -V(\rho_{bead} - \rho_{fluid})g \tag{2.28}$$

where ρ_{bead} and ρ_{fluid} are respectively the density of bead and liquid. V is the volume of the particle and g the gravitational acceleration. For *Dynabead My-One* particles which have a density of about 4 g*cm^{-3}, this contribution is around 80 fN in water.

The magnetic interaction between a bead and a certain magnetic field can be described by the magnetic potential energy density $u_b = \mathbf{M}_b \cdot \mathbf{B}$, where M_b is the bead magnetization.

The force per unit of volume that is related to the magnetic interaction is $\mathbf{f}_M = -\nabla u_b$. it is possible valuate the total force acting on the entire particle by integrating $\mathbf{f}_m$ over the bead volume:

$$\mathbf{F}_m = -\mu_0 \int_V (\mathbf{M}_b \cdot \nabla)\mathbf{H} dV \tag{2.29}$$

It is valid if $\nabla \times \mathbf{B} = 0$ as in the magnetostatic case, and exploiting the equivalence of the equation 2.25. In this thesis work, this integral has been calculated through numerical methods via *Matlab* (see chapter 4 and 6).

A particle moving with velocity $\mathbf{v}$ in a fluid of velocity $\mathbf{u}$ is subjected to the hydrodynamic drag force. This force $\mathbf{F}_{drag}$ obeys to the Stokes law:

$$\mathbf{F}_{drag} = -6\pi\eta R_b(\mathbf{v} - \mathbf{u}) \tag{2.30}$$

where η is the fluid viscosity and R_b the bead radius. It opposes the magnetic interactions in the magnetic handling process.

Finally, Brownian motion leads to superimposed velocities in random directions which become more important as the size of the particles decreases. The diffusion constant D and the related diffusion length l_{dif} for a spherical particle in a fluid at temperature T are inversely proportional to the bead radius and are respectively equal to [48]:

$$l_{dif} = \sqrt{Dt} \tag{2.31}$$

with

$$D = \frac{K_B}{\xi} = \frac{k_B T}{6\pi\eta R_b} \tag{2.32}$$

where ξ is the friction coefficient. For example, after 1s of diffusion in water at room temperature, a 1 μm diameter particle travels an average distance of 700 nm. For a magnetic particle with a diameter of 100 nm the diffusion length on the same time scale is almost three times larger.
In the next section, the description of the physical mechanism of the DW assisted manipulation of magnetic particles will be given.

2.2.2 DWs assisted manipulation of magnetic nanoparticles

As discussed in section 2.1.8 the DWs can be nucleated, pinned and propagated along magnetic conduits. Moreover, Neel walls produce a highly inhomogeneous stray field, up to few kOe which can be employed to trap a MNP in suspension. This stray field is spatially localized at the nano scale

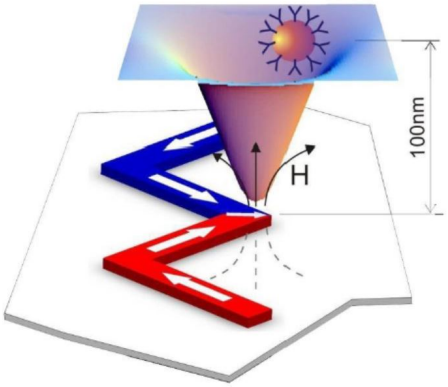

Figure 2.7: Sketch of the magnetic attractive potential well generated by a HH DW pinned at one corner of the magnetic conduit. Such potential is able to trap a superparamagnetic antibodies functionalized bead at a distance of 100 nm from the chip surface. From [49]

on the plane of the conduit thanks to the very confined geometry of the DW.

The DW, nucleated by the application of an external magnetic field, acts as movable attracting pole (see Fig.2.7). The gradient, together with the intensity of the stray field produces an attractive force on a superparamagnetic particle which is moving in the proximity of the DW location. The DW field induces a magnetic moment in the particle that then is attracted towards the minimum of the potential. In this way, when the DW is depinned from one pinning site to another, applying an external field, the particle also moves, following the modification of the attractive landscape potential. This technology allows a maximum transport speed of 15μm/s which is affected by the viscosity of the medium where particles are diluted. This technology, called "domain wall tweezers" (DWT), has been invented by the NaBis group of LNESS in collaboration with nanoGUNE research center [60]. In this thesis work, two different geometries for the magnetic conduits are employed: zig-zag shaped and curved conduits; they are illustrated in chapter 4.

2.3 Anisotropic Magnetic Resistance

Magnetoresistance refers to the change in electrical resistance of magnetic materials with the application of a magnetic field and was first discovered by William Thomson (Lord Kelvin) in 1851. Changes in resistance of up to 5% were observed and this discovery was later referred to the Ordinary Magnetoresistance (OMR). More recently anisotropic (AMR), giant (GMR), colossal (CMR), and tunnelling magnetoresistance (TMR) effects have been discovered with larger changes in resistance reported. In this thesis the AMR will be employed in magnetic based sensors in order to count the particle transit in lab on chip for drug delivery.

Anisotropic Magnetoresistance is the property of a material in which the electrical resistance depends on the angle between the direction of electrical current and orientation of magnetization. The AMR effect is based on

the anisotropic scattering of conduction electrons of the band with uncompensated spins (e.g., 3d electrons for the first series of transition metals Fe, Co and Ni). Theoretical analysis of AMR are given in terms of the electron density-of-states diagram at the Fermi level. The difficulty is that the anisotropic part of the resistance depends on the exact three-dimensional shape of the Fermi surface (3d-envelope of the Fermi level), which is not precisely known except for very few magnetic materials. If we indicate the resistivity in the direction parallel and perpendicular to the direction of M as $\rho_{\parallel}$ and $\rho_{\perp}$, in most of the magnetic materials is observed that $\rho_{\parallel}>\rho_{\perp}$. In this case, the AMR is defined as:

$$R_{AMR} = \frac{\rho_{\parallel} - \rho_{\perp}}{\rho} \tag{2.33}$$

where ρ is defined as

$$\rho = \frac{\rho_{\parallel} + 2\rho_{\perp}}{3} \tag{2.34}$$

For example, let us consider a ferromagnetic strip in presence or absence of a DW as illustrated in figure 2.8.

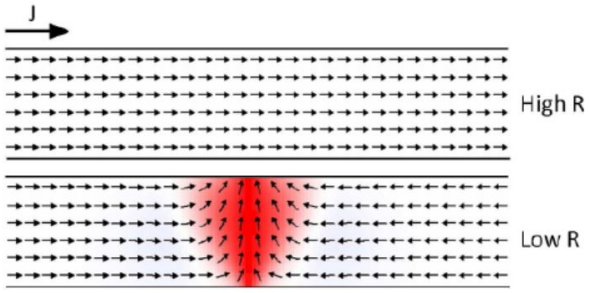

Figure 2.8: AMR effect in a ferromagnetic strip in presence of a DW; the resistance is higher when **J** and **M** are parallel. Image from OOMMF.

If a current density **J** flows in the strip and a DW is present in the conduit segment considered, the magnetization in the DW points perpendicularly to

the current flow. This means that the resistance is lowered respect to the case when there is no DW and **J** and **M** are parallel. Sensors based on the AMR effect will be described in Chapter 5.

Chapter 3

Experimental methods

In this chapter an overview of all the experimental methods used in this thesis work is presented, starting from the fabrication of samples and devices, to the device characterization techniques but also the experimental setups exploited for biological assays.
Three main different microfluidic-devices have been developed, produced and tested in this work: nanopatterned samples for particles manipulation, AMR sensors and capacitive sensors for bead detection.

3.1 Micro- and nano-fabrication techniques

The fabrication of microfluidic-devices requires the patterning of magnetic nanostructures over a SiO_2 (1000nm)/Si substrate. The material mainly used for the magnetic micro and nanostructures is Permalloy ($Ni_{80}Fe_{20}$, Py). The choice of this material is particularly suitable for the fabrication of the magnetic conduits, since Py has many favorable properties such as a negligible magnetocrystalline anisotropy, high saturation magnetization, low coercivity. Due to these characteristics, the magnetization is mainly driven by the shape of the nanometric conduits (See section 2.1.6) and the magnetic stray field gradient generated by DWs is large enough to trap magnetic particles

in suspensions over the magnetic structures. Moreover, Py thin films display a high AMR.

The micro and nanostructures employed in this work are fabricated by means of electron beam lithography (EBL) and optical lithography and a lift off procedure. The deposition of Py and Au contacts of the AMR devices are deposited by electron beam evaporation. Besides, nanopatterned chips are capped with an uniform thin film of different materials (such as SiO_2 or Al_2O_3), grown by magnetron sputtering, to prevent damages from the wet environment. Finally, a Poly-DiMethylSiloxane (PDMS) cell is placed on the summit of the chips to contain the fluid in which MNPs are dispersed.

In the next sections, the different techniques above mentioned are in depth described.

3.1.1 Optical and Electron-beam lithography

Once the geometries of the devices have been designed, the patterns are transferred on the top of the substrate by means of electron beam or optical lithography. The EBL has been used to write patterns with submicrometer resolution (such as the magnetic structures and fine electrical contacts), instead optical lithography is employed to transfer structures tipically larger than 1 μm (such as the external electrical contacts -see Fig. 3.1(a)-). The EBL fabrication of the magnetic rings array presented in chapter 4 was carried out by the LPN-CNRS (Laboratoire de Photonique et de Nanostructures, A. Cattoni) of Paris. The zig-zag shaped magnetic nanostructures (see Chapter 4 and 5) and the "fine" electrical contacts were made by the EBL group in the L-NESS laboratory (see Fig. 3.1(b)). The optical lithography process to pattern the external electrical contacts is performed by me at the L-NESS clean room.

In principle the lithography process always consists of the following steps: a) wafer cleaning from contaminants b) prime coating for improving the resist

adhesion to the substrate, c) resist spin coating, d) resist soft bake (only for optical lithography), e) exposure of specific part of the resist to UV light or electron beam, f) development: the soluble zones of the exposed resist are dissolved by using a developer (solvent) while leaving the others undisturbed. The entire lithographic process is illustrated in Fig. 3.1(c).

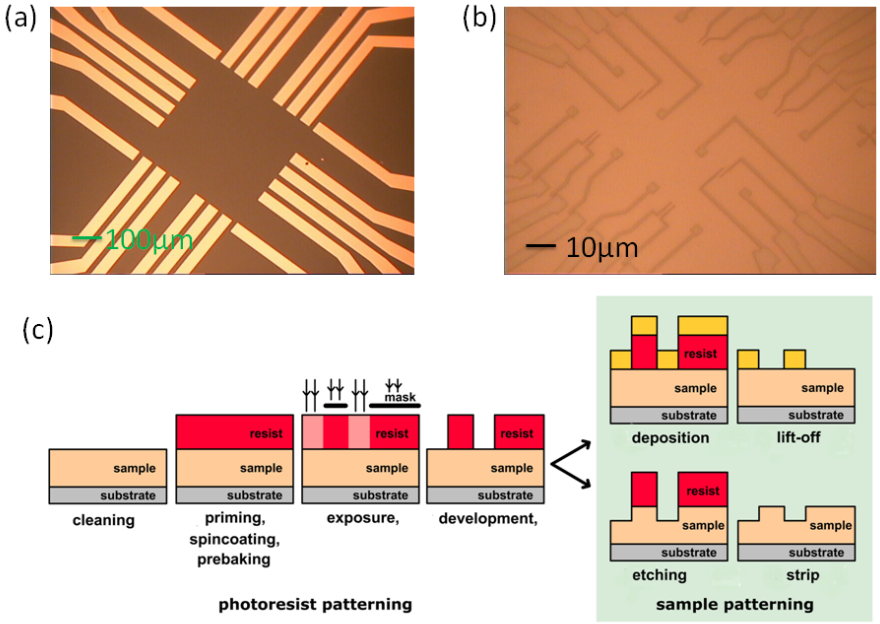

Figure 3.1: Microscope images of optical lithography patterning of external contacts (a) and EBL patterning of fine contacts (b). Sketch of the entire lithography process (c)

Two types of photoresist (PR) can be used: "positive resist" which is removed in the exposed area or "negative resist" whch is removed in non-exposed area. The patterned resist can be employed as an open mask for metallization (as it is always the case in this thesis) or as a protective mask for etching. After that, the resist can be completely removed leaving on the

substrate the metallic nanostructures or the non-etched parts. This process is called *Lift-off* and the resist is dissolved in an organic solvent like acetone, AZ 100 remover (Sigma Aldrich, USA) or n-ethyl-pirrolidone (NEP) for e-beam resist, removing the resist and consequently all the material parts not directly in contact with the substrate. This procedure is performed heating the remover at 60^{o}C on an hot plate and leaving the sample immersed for a time varying between 1h, for the AZ 100 remover or acetone, and 2h for NEP.

For the optical lithography a mask aligner is exploited to align the mask with sample and in this case it is *Karl Suss MA56* (figure 3.2), which can work both in full-contact and in proximity mode; it can support wafers of 4" and masks of 5". The lamp used for expositions mainly emits light at a wavelength of 365 nm, with a power density of about 13 mW/cm^2.

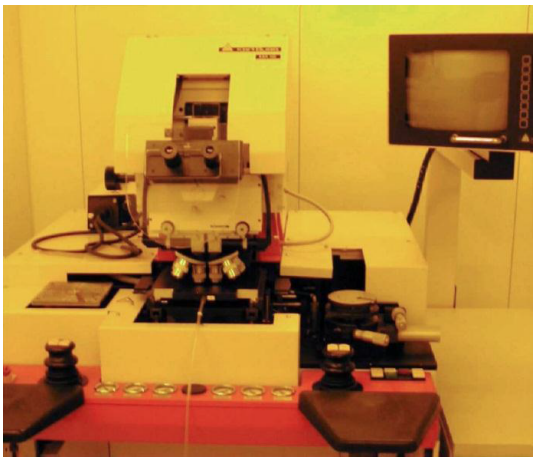

Figure 3.2: Mask aligner Karl SussMA56.

For the fabrication of the external contacts in AMR and capacitive sensors (see Fig. 3.1(a)), the image reversal AZ5214E photoresist (Microchemicals, USA) was used. This positive resist can be inverted through an extra backing

after exposition and a "flood exposure" before developing. In order to obtain an undercut profile suitable for the lift-off technique, the inverted mode has been exploited. All the parameters of the process have been optimized in order to be able to precisely define features with dimension of 2 μm or smaller:

- Substrate cleaning with acetone and isopropanol, drying with Nitrogen.
- Prime spinning and subsequent bake on hot plate at 120^0 C for 120 s
- Spinning of AZ5214E at 5000 rpm
- Soft bake at 110^0C for 50 s
- Exposure with positive mask at broadband light at a dose of 29.9 mJ/cm^3
- Reversal bake (the most critical step): 117^0C for 100 s.
- Flood exposure at a dose bigger than 455 mJ/cm^3
- Development: 25 s in AZ726 MIF developer (Microchemicals, USA)

3.1.2 Electron beam evaporation

Once the resist is developed a thin film of magnetic material or a bilayer of Ti (as adhesive layer) and Au is deposited by electron beam evaporation. This process consists in an electron beam heating a crucible containing the evaporation material above the melting temperature in a vacuum chamber. Evaporated atoms can move from the crucible (made of refractory material in order to prevent evaporation if the electron beam is misaligned) to the substrate along an almost linear path, since atoms do not undergo collisions in vacuum. In fact, the mean free path (the distance covered by atoms between two collisions), at a pressure of less than 10^{-5} mTorr, is greater than the typical distances of a deposition chamber.

The deposition process has many limitations imposed by the resist: it must, for example, occur at temperatures not exceeding 200°C because of the thermal stability of the resist. The deposition rate, once the target-substrate distance and the material are fixed, just depends on the electron beam power. The parameters used during the evaporation are listed in table 3.1.

Material	**Base pressure**	**Deposition distance**	**Rate**	**E-beam power**
Permalloy	$2*10^{-6}$ mTorr	10cm	0.1nm/s	9% of the full scale
Gold	$2*10^{-6}$ mTorr	10cm	0.1-0.2nm/s	6% of the full scale
Titanium	$2*10^{-6}$ mTorr	10cm	0.1nm/s	7% of the full scale

Table 3.1: Parameters used in the evaporation processes and the relative deposition rate

In the L-NESS lab, the machine employed is a Leybold "Heraeus L560" evaporator.
The deposition rate was monitored with an integrated thickness monitor (a quartz microbalance) which has been calibrated by direct measuring the thickness of the deposited films.
In order to facilitate the resist removal, the deposition technique should be strongly directional with low capacity of step coverage. In this view the evaporation technique is better for lift-off than the sputtering deposition (described in the next section)which is more isotropic. The process described in the last two sections (3.1.1 and 3.1.2) can be repeated to grow complex structures in which many lithographic steps have to be performed or different materials have to be deposited on the same surface. For example, AMR and capacitive sensors require two EBL steps (for the deposition of magnetic structure and the fine electrical contacts) and one optical step for the external contacts.

3.1.3 Capping and microfluidic cells

Once the devices are properly patterned with the nanostructures, a "capping" thin film is deposited on the top of the entire chip to prevent it from damages due to the wet environment, to favor the adhesion of the PDMS cells and to planarize the surface. Two different materials have been tested as capping layer: SiO_2 and Al_2O_3. All of these are deposited by *Magnetron Sputtering*.

Magnetron Sputtering is a physical deposition method where ions from an argon (Ar) plasma are focused through a magnetic field to transfer momentum to the atoms of a target, which are then deposited onto the substrate in a vacuum chamber. A detailed description of the sputtering process can be found in [50]. The machine employed for this purpose is the *AJA Orion 8 system* aviable at the L-NESS.

The system is provided with 10 confocal magnetron sputtering sources which can be also used for co-deposition. In order to deposit the insulating cover layers a radio-frequency (RF) source is used, in order to avoid the formation of a charged layer on the top of the target which would diminish the effectiveness of the sputtering process. The deposition parameters are illustrated in table 3.2.

Material	**Base pressure [mTorr]**	**Rate [A/min]**	**Power density [W/cm^2]**
Al_2O_3	3	4.84	15.79
SiO_2	2	12.46	9.87

Table 3.2: Parameters used in magnetron sputtering processes and the relative deposition rate.

After the protective layer deposition, a PDMS microfluidic cell is placed

on the summit of the chips to contain the liquid. The PDMS (Poly-DiMethylSiloxane) is a flexible and transparent polymer which is bound to the surface of the samples after being properly preparated. PDMS is prepared using the Sylgard 184 Silicone Elastomer Kit, according to the following protocol:

- The elastomer is mixed with its curing agent. The elastomer and curing agent are carefully mixed in the 10:1 ratio for few minutes;
- The mixture is placed in a vacuum chamber until all the bubbles, due to the mixing, disappear;
- The PDMS is then slowly poured to a smooth and clean surface (for example, a silica wafer was exploited for this purpose). Bubbles should be avoided because they would otherwise create defects in the solidified sample;
- The PDMS sample is put in the oven for about 3 hours at 65^oC
- Once the PDMS is cured and cooled to room temperature, it can be cut as the shape of the chip substrate and peeled out.

The PDMS gasket is then bonded to the capping layer on the chip, with the use of an oxigen plasma in a *Plasma Asher Machine*. In such equipment, the RF plasma at low energy and sufficient pressure is used to assist and control surface chemical reactions, modifying the hydrophobicity of both PDMS and capping layer surface to hydrophilic ones. The chip and the PDMS are placed in the vacuum chamber of the plasma asher and exposed to oxygen plasma at 1 mbar of pressure and 150 W of power for 2 minutes. After this treatment, the PDMS is placed directly in contact with the capped sample within 1 minute, since the surface modification is temporary. Additionally, the entire structure could be put on a hotplate at 75^oC for 15 minutes in order to increase the bond force.

3.1.4 Process flow

In the previous sections an overview of the fabrication techniques exploited in this work, was performed. In the next sections the process flow to fabricate samples for beads manipuation, AMR sensors and impedantial based sensors will be described.

Devices for beads manipulation

The results described in chapter 4 and 6 are obtained by means of magnetically patterned chips that permit to manipulate superpara magnetic nanoparticles as described in chapter 2.
The fabrication process is the following:

- Patterning of rings array by electron beam lithography on a Si/SiO_2 substrate (see Fig. 3.3). The rings have a diameter of 5 or 10 μm and width of 300 nm.

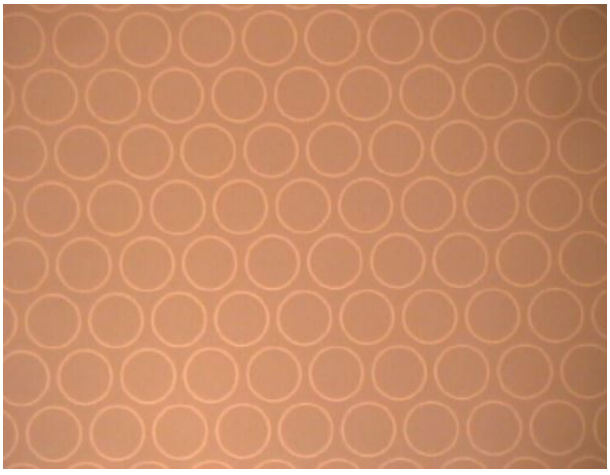

Figure 3.3: Rings array pattern obtained by EBL.

- Deposition of a thin film (30-60 nm) of Permalloy by electron beam evaporation

- Lift-off procedure to remove the resist (2 h in NEP at 60^{o}C)
- Sputtering of a capping layer (50-70 nm) by magnetron sputter. Different materials were tested to this purpose (such as Al_2O_3 or SiO_2)

AMR sensors

The devices used to detect the beads transit, through a magneto-electrical measurement based on AMR effect, are fabricated as follows:

- Patterning of fine electrodes by EBL on a Si/SiO_2 substrate (see Fig. 3.4(a)).
- Deposition of Ti as adheisve layer (3 nm) and Au (20 nm) by electron beam evaporation.

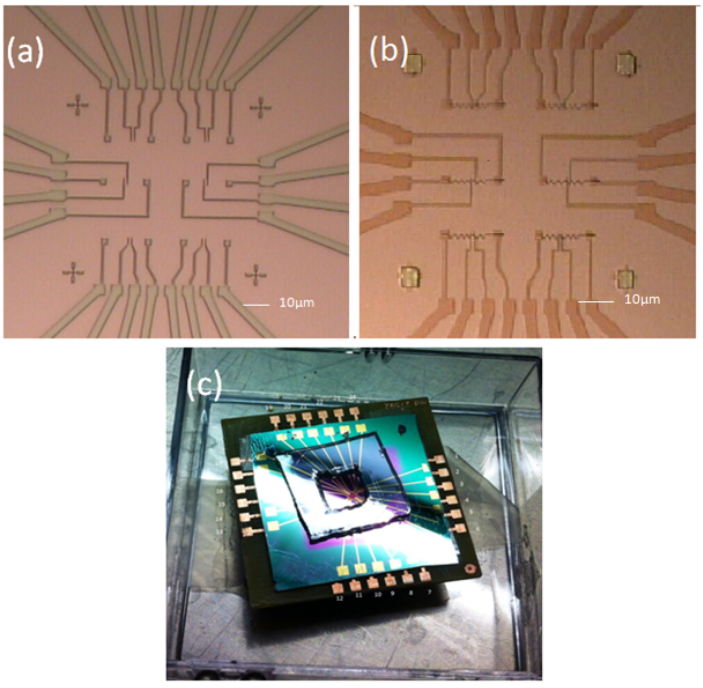

Figure 3.4: Optical image of the AMR device: after the first (a) and the second (b) step. Picture of the final device (c).

- Lift-off procedure (2 h in NEP at 60^oC).
- Patterning of zig-zag shaped structures by EBL (see Fig. 3.4(b)). Zig-zag segments are long 2 μm and the conduit width is 200 nm.
- Deposition of Permalloy (25-30 nm) by e-beam evaporation.
- Lift-off procedure (2 h in NEP at 60^oC).
- Patterning of external electrical contacts by optical lithography.
- Deposition of Ti (5 nm) and Au (65 nm) by e-beam evaporation.
- Lift-off (1 h in AZ remover at 60^oC).
- Sputtering of a capping layer (40-50 nm) of SiO_2.
- Positioning of a PDMS gasket on the top of the chip (see Fig. 3.4(c)).

Finally, it is worth to notice that the thickness of magnetic conduits is 25-35nm, lower compared to rings structure, in order to guarantee the formation of completely transverse Neel walls, enhanching the AMR effect (see section 2.3).

Capacitive sensors

The sensors based on impedential detection of beads have been manufactured in the following way:

- Patterning of zig-zags shaped conduits by EBL (see Fig. 3.5(a)).
- Deposition of $Ni_{80}Fe_{20}$ (30-40 nm) by electron beam evaporation.
- Lift-off procedure (2 h in NEP at 60^oC).
- Sputtering of a thin film of SiO_2 (30 nm) to cap zig-zags.

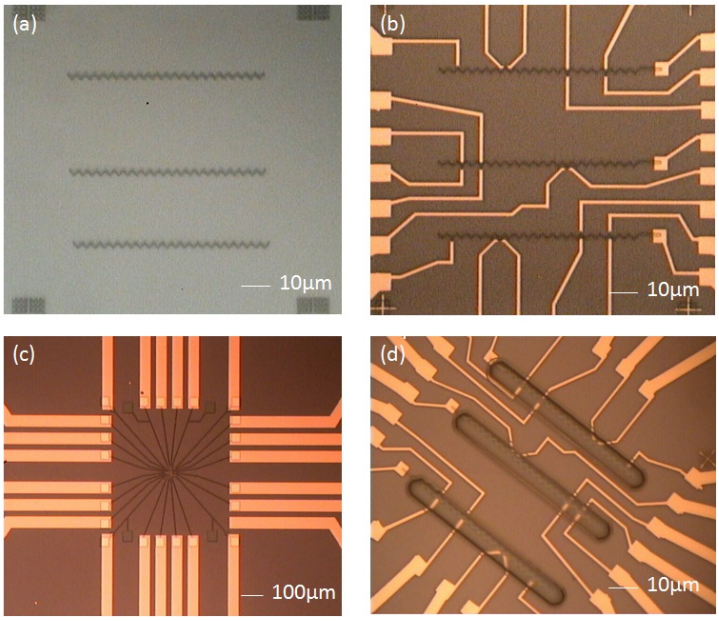

Figure 3.5: Optical microscope images of the fabrication process for a capacitive sensor.

- Patterning of fine electrical contacts by EBL (see Fig. 3.5(b)). Various geometries of coupled electrodes have been tested.
- Deposition of Ti (5 nm) as adhesive layer and gold (65 nm) by e-beam evaporation.
- Lift-off procedure (2 h in NEP at 60^{o}C).
- Patterning of external electrical contacts by optical lithography.
- Deposition of Ti (5 nm) and Au (80 nm) by e-beam evaporation.
- Lift-off (1 h in AZ remover at 60^{o}C).
- Patterning of the protective layer: micrometric strips are patterned by optical lithography in order to protect the chip by the fluids, while

maintaining exposed the sensing area (contacts near the zig zag). (see figure 3.5(c)).

- Sputtering of SiO_2 or Al_2O_3 (50 nm) as capping layer.
- Lift-off procedure (1 h in AZ remover at 60^oC).
- Positioning of a PDMS gasket on the top of the chip (see Fig.3.5(d)).

As alternative, the capping layer was replaced by the resist used for the last litographic step. It is employed because, due to its thickness (2μm), it guarantes a good insulation of contacts from the liquid. An extra backing (at 120^oC on a hot plate) was performed in order to increase the hardness of the resist.

3.2 Characterization methods

The main technique employed to characterize the samples morphology is *atomic force microscopy*. In order to study and draw the magnetic configuration of such samples a variant of this method called *magnetic force microscopy* has been used.

3.2.1 Atomic force microscopy(AFM)

AFM is a scanning probe microscopy technique which permits to provide topographical maps of the sample surface with sub-nanometric resolution. A sharp tip (few angstrom in width) mounted on a cantilever is positioned within a few nanometers above the surface of the sample, then the probe is moved laterally (in the plane of the sample) by a piezoelectric manipulator which can provide sub-nanometric motion increments. The change in height of the surface causes a variation in the interatomic forces between tip and

sample. As a consequence, deflections are produced in the cantilever. These deflections are measured using a laser beam which reflects on the cantilever and is collected by a photodetector. Figure 3.6 shows the schematic of an AFM working principle.

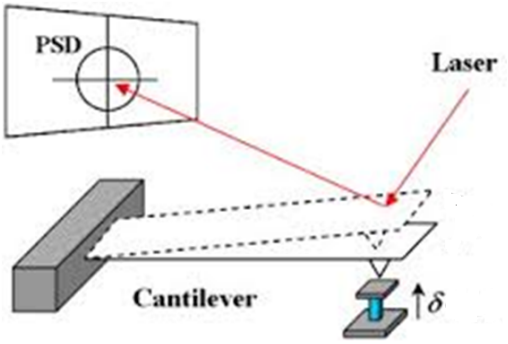

Figure 3.6: Sketch of the AFM working principle

The interatomic forces between tip and sample is described by the empirical Lennard-Jones potential:

$$V(\mathbf{r})_{LJ} = \frac{A}{r^{12}} - \frac{B}{r^{6}} \tag{3.1}$$

where the r^{-6} term describes attractive interaction due to the Van der Waals force and the r^{-12} component represent the Pauli repulsion due to the overlap of interatomic orbitals. Three possible operational modes for the AFM, depending on the the tip sample distance, exist: contact mode, non-contact mode and tapping mode. In contact mode, the tip scans the sample in close contact with the surface and thus experiences strong repulsive forces. Due to the large variation of the force with distance, it is possible to achieve extremely high resolutions. However, the dragging motion of the probe tip, combined with adhesive forces between the tip and the surface, can cause substantial damage to both sample and probe and create wrong images. In non-contact mode the tip is kept from 5nm to 15nm above the surface and is

forced to oscillate at a frequency slightly above its resonance frequency with a typical oscillation amplitude of a few nanometers (<10 nm). The increased tip-sample distance lead to a reduced damaging of the sample but, since the force on the tip is far less intense than in contact mode, the resolution is much lower. The last operational mode for the characterization of the surface topology, is the tapping mode [52]. In this mode, the cantilever is driven to oscillate up and down near its resonance frequency with an oscillation amplitude which typically ranges from 100 nm to 200 nm and a frequence between 50 and 70 KHz. A tapping AFM image is therefore produced by imaging the force of the intermittent contacts of the tip with the sample surface. Due to the forces acting on the cantilever when the tip comes close to the surface, the amplitude of the oscillation is reduced. A feedback cycle then restores the nominal amplitude by adjusting the tip height through the piezoelectric vertical motion so that it provides point-by-point the information about the surface topography. The machine used in this work is a *VEECO innova system* illustrated in figure 3.7.

Figure 3.7: Atomic force microscope *VEECO innova*

3.2.2 Magnetic force microscopy (MFM)

The magnetic force microscope [51] is a variant of the AFM in which the magnetic force or the force gradient is employed to visualize the magnetic configuration of a sample with a high resolution. The tips are covered by a ferromagnetic material and the basic idea is measuring the cantilever deflection due to the interaction between the tip and the stray field generated by the sample. The competition between Van der Waals forces and magnetic forces has to be considered: for short distances (tipically less than 10 nm) the Van der Waal forces lead, instead for larger distances the magnetic forces (the magnetic force gradient) are the dominant term in the tip-sample interactions. Two different working behaviour occur as a function of the distance between the tip and the sample: the so called *far field* regime and the *near field* regime. In the first case the signal, related to the force gradient, is dominated by the surface magnetic properties of the sample, while in the second case by the changes in the sample topography. As in the AFM case the tapping mode is used. In order to separate the magnetic image from the topography, the signal detection by the MFM is realized through a two-step procedure, also called lift mode (see Fig.3.8)[54]. During the first

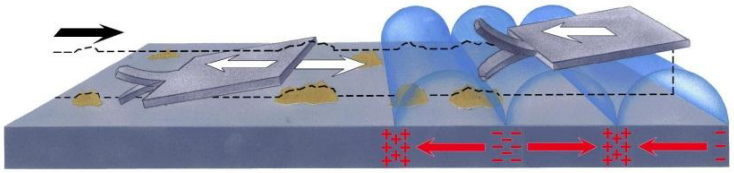

Figure 3.8: Magnetic force microscopy: lift mode. In the first step the topography of the surface is recorded, while in the second step, the magnetic image arising from the stray field of magnetic domains in the sample is captured.

step, outwards, the cantilever oscillates close to the surface, recording the

topography. In the second step, on the way back, the cantilever is lifted up at a selected height in the range of 10-200 nm and the magnetic image is registered at constant height (without feedback) on the basis of the topography saved outwards. The distance is kept at sufficient high value in order to make the Van der Walls force contribution negligible; thus the cantilever is sensitive to the magnetic forces only. The magnetic image gives us direct information about the presence of surfaces domain walls and in general on the magnetization of the thin film sample. Note that the magnetic force can be attractive or repulsive for a tip with permanent magnetic moment. The MFM image contrast tells us the nature of the interaction. Considering, for example, in figure 3.9, the tip repulsion leads to brighter spots while attractive forces means darker spots.

Figure 3.9: MFM image of a zig-zag magnetic conduit: dark and bright spots represent respectively an attractive or repulsive magnetic force, acting on the ferromagnetic tip.

The tip height while registering the magnetic signal was set from 80 nm to 200 nm, depending on the fabrication quality of the structures tested. Fabrication defects like impurities bumps or high peaks at the structure edge require to set high tip-surface distance in order to avoid detrimental contacts with magnetic material during the backward scan. For the image acquisition MAGT magnetic tips (App Nano, USA) have been used. They are covered by a thin film of 50±5 nm of CrCo with a magnetic moment (10^9-10^{11} Am^2) and a minimum coercivity of 500 Oe.

3.3 Experimental setups

In the following sections a description of the experimental setups employed in this work is illustrated. In particular, the next paragraph shows the system used for manipulation of beads and for biological tests, instead in section 3.3.2 the setups for magneto-electrical measurement on AMR and capacitive sensors are presented.

3.3.1 Setup for biological experiments and beads manipulation

The experimental results shown in chapter 4 and 6 have been mainly obtained by means of the setup illustrated in Figure 3.10.

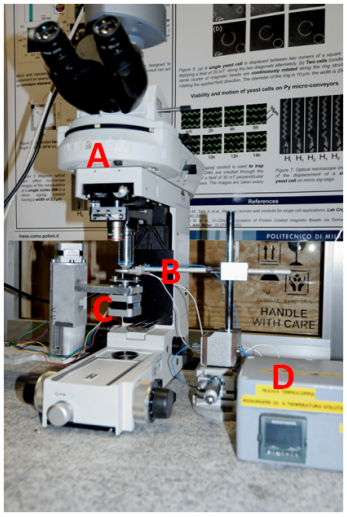

Figure 3.10: Experimental setup for biological tests and beads manipulation. A indicates the optical microscope (Nikon Eclipse FN-1), B the entire sample stage, C the stepper motors system and D the thermostat.

In such system an alluminium (Al) sample stage is mounted on a metallic arm which is connected to a micromanipulator, allowing a fine control of the

in-plane sample position. Besides the sample stage is able to contain 800 μl of liquid so that experiments can be performed in a wet environment (as it always the case).

For biological tests in which the temperature control is fundamental to guarantee the cells viability, a thermo-couple is placed close to the sample in order to measure the temperature in the liquid. A PID thermostat, connected to the thermo-couple, is employed to control and set the temperature by means of a thin conductive heater made of silicon rubber and properly mounted just under the alluminum stage. A good thermal contact is ensured by a heat-sink paste.

The nano-objects and the cells have been monitored by the optical microscope "Nikon Eclipse FN-1" equipped with 60x water immersion objective (Nikon NIR-APO, numerical aperture 1.0) so that a water environment or, at least, a drop of water as focusing lens is required between the objective and the sample. A second 4x objective was used to center the area of interest. The light was provided to the microscope by an arc-discharge mercury lamp (NIKON intensilight C-HGFI). The microscope is equipped by an electronic fine controller of the objectives displacements along the direction perpendicular to the plane. Two additional filters have been installed in the light pathway of the microscope: FITC (Fluorescine IsoThio-Cyanate) and TRITC (Tetramethyl Rhodamine Iso-Thiocyanate) fluorescence filter blocks. FITC filter provides an excitation light bandwidth of 465-495 nm (blue spectral region) and an absorption bandpass from 515 nm to 555 nm (green spectral region), TRITC filter block have an excitation bandpass of 525-540 nm (green spectral region) and an absorb in the red spectral region from 605 nm to 655 nm. Fluorescence has been employed in biological experiments to distinguish magnetic nanoparticles, functionalized by a TRITC marker and cells "coloured" with a FITC one. The data acquisition is performed by a fast electron-multiplying charge-coupled device (EM-CCD) camera (ANDOR

Luca-S, Belfast UK) which has a resolution 658 x 496 pixel, max 50 fps. It is Peltier cooled down to -20^{o}C in order to reduce the thermal electronic noise. The external in plane magnetic field which is needed for beads manipulation through the DWs formation and displacement is applied exploiting two couple of permanent cilindric magnets made of NdFeB and properly placed over an Al plate as illustrated in figure 3.11. The maximum stray field produced

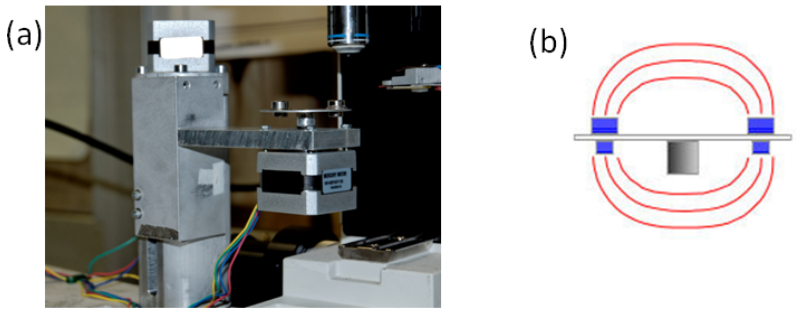

Figure 3.11: Image of stepper motors used to control the rotation and the height of a plate containing two couples of permanent magnets (a). Sketch of the lines of force from the permanent magnets field (b)

in-plane by the magnets (located at 2 cm of distance each other) is 400 Oe at 5 mm over the plate, in the center of it. In order to achieve a variation of the magnetic field direction, the plate is connected to a stepper motor which allows a controlled rotation. A similar stepper motor is employed to finely regulate the height of the plate by means of a screw connected to the motor shaft. A stepper motor is a DC powered component that divide a full rotation in an equal number of steps. The working principle is the following (see Fig.3.12)[53]: a multiple "toothed" electromagnet is arranged around a central iron gear. The electromagnets are sequentially energized by an external control circuit. In order to turn the motor shaft, the first electromagnet is powered so that the gear's teeth are magnetically attracted to the electro-

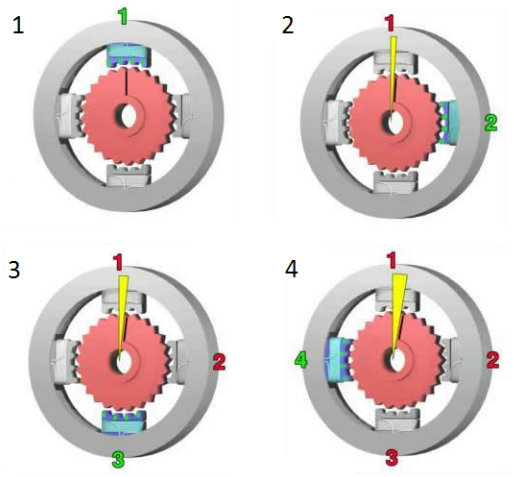

Figure 3.12: Sketch of the stepper motors working principle. The electromagnets around the central gear are sequentially powered to get a single step rotation.

magnet's teeth. When the gear's teeth are aligned to the first electromagnet, they are slightly offset from the second electromagnet. In this way when the second electromagnet is turned on and the first is turned off, the gear rotates slightly to align with the second one, and from there the process is repeated. Each one of those pieces of rotations is called "step", with an integer number of steps making a full rotation. In that way, the motor can be turned by a precise angle. In this work SM-42BYG011-25 stepper motors are used. A precise control of the plate rotation down to $1{,}8^o$ (200 steps for the entire revolution) is achieved.

The stepper motors are powered through proper drivers and they are controlled by means of an *Arduino-uno* microcontroller. Arduino can be easily interfaced with a *labview software* to achieve an efficient and remote control of the whole system.

In order to apply an out of plane magnetic field, a small hollow cilinder shaped coil was designed and placed around the microscope objective. This

electromagnet exercises a maximum field of 100 Oe, 1 cm far from the bottom side (where the sample is located). The current is supplied by a *Kepco*^{TM} bipolar power generator and controlled by a Labview software via GPIB-USB connection.

A part of the experimental results described in chapter 6 have been performed at the IFOM center using the same setup described in this chapter except for the optical microscope that has been substituted with *TCS-SP5, LEICA*, a confocal microscope. This machinery permits a higher spatial resolution and sharpness of fluorescent images, by using a point illumination based on a laser and a spatial pinhole to eliminate out-of-focus light in specimens that are thicker than the focal plane.
A full descrption of confocal microscope working principle can be found in[55].

3.3.2 Setup for sensors measurements

The setup employed to test the AMR and capacitive sensors is illustrated in figure 3.13. A four coils electromagnet is used, replacing the stepper motors system, because a fine control of the field absolute value has to be performed. This electromagnet was projected to apply a maximum field of 700 Oe when the distance between poles is 4 cm. It is powered by two Kepco^{TM} bipolar generators.
The sample stage is shown in figure 3.14. A small electrical board transfers the electrical signal from coaxial cablets to smaller electrical wires which end with "tulip" shaped contacts. They are connected to electrical pins of a second small board. The chip glued on the top of it is electrical connected via wire bonding to the boards pads. The bonding procedure deals with the connection of two electrical pads through a gold wire having a diameter of some micrometers, whose extremities are sealed by thermal heating to the contacts. This procedure was performed by the "electronic engineering" group in Milan.

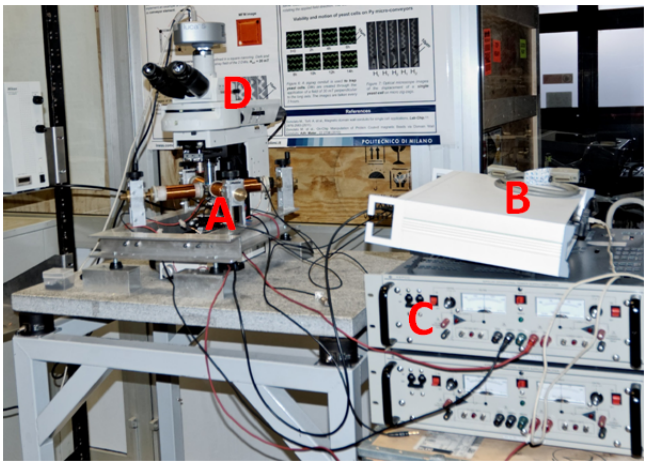

Figure 3.13: Experimental setup for sensors measurement. A is the four poles electromagnet, B is the Lock-in amplifier (HF2LI), C is a bipolar generator (Kepco^{TM}) and the optical microscope (Nikon Eclipse FN-1).

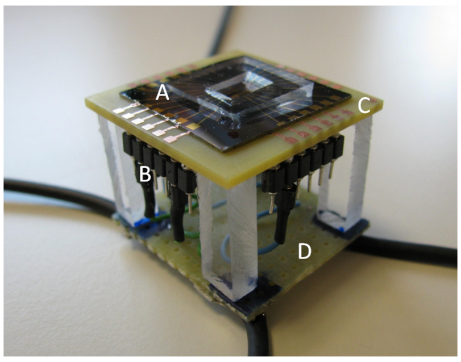

Figure 3.14: Sample stage employed in electrical measurements. A is the AMR or capacitive device, B the electrical pins connected to the "tulip" wires. C and D indicate the small electrical boards

The entire sample stage is held up by four plexiglass legs and it is mounted on a micromanipulator to control the position of the device in plane.

The microscope used to monitor the sensors is the same described in the previous section and it is employed in bright field mode (BF).

AMR sensors measurements

AMR sensors, whose fabrication process is described in section 3.1.4, are used to detect and count the MNPs which are trapped and manipulated over a zig-zag shaped magnetic nanoconduit. A magneto-electrical measurement which is based on the AMR effect described in section 2.3 is performed. The working principle of such sensors is the following: when a magnetic DW, which is in this case a Neel trasverse wall with the magnetization pointing perpendicular to the conduit direction, is located between two electrical contacts. A voltage drop along that piece of conduit is measured due to the AMR effect. The zig-zag structure permits to control the displacement of a single DW from one corner to another by means of a sequence of magnetic fields applied in the direction of the straight segments (see chapter 4). In this way the crossing of a DW between two electrical contacts can be electrically detected. If a MNP is trapped over the DW, a variation of the depinning field (the minimum field required to displace a DW from one corner to another) occurs. In this way, synchronizing the electrical signal acquisition and the applied field, it is possible count the beads passing over the conduit.
The electrical measurements are performed through a *four point probes technique* in which a couple of contacts are used to apply a certain signal, and the other two contacts are employed to detect the electrical response. In order to reduce the electrical noise, a modulation technique and a lock-in amplifier (*HF2LI Zurich instrument*) was used. A schematic view of the equivalent circuit is illustrated in figure 3.15.

The external contact A is supplied by the HF2LI instrument with an AC signal, instead D is connected to ground. The applied voltage amplitude is

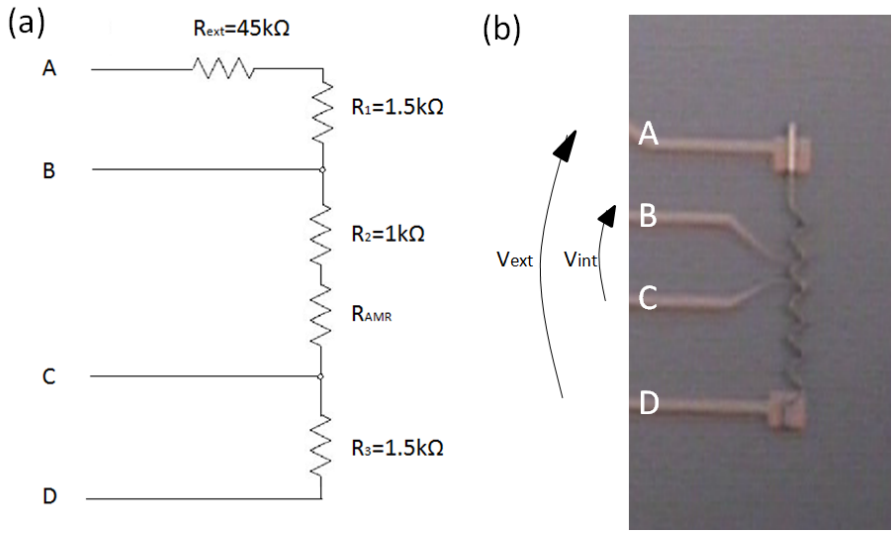

Figure 3.15: Schematic of the equivalent circuit of AMR sensors measurements (a) and optical microscope image of the device which shows the electrical contacts and the magnetic zig-zag shaped conduit.

50 mV-200 mV (the current that flows in the zig-zags is 1-4 μA) and the frequence is set between 10-100 kHz. The voltage drop between B and C is measured by means of the HF2LI machinery.
R_1, R_2 and R_3 are mainly related to the zig-zag shaped nanostructure resistivity, because the gold electrodes conductivity is very high. R_{AMR} (which is the resistance encountered by the current flowing along the conduit) varies if the magnetization is parallel or perperndicular to the nanostructure direction, as it is the case when a DW is located between B and C. The output signal is acquired and demodulated by the lock-in amplifier, in order to remove the periodic, low frequency noise.
The external magnetic field is controlled remotely by a Labview software. A proper sequence of magnetic fields is applied to nucleate and displace a single DW in the zig-zag structure to the corner between electrodes B and C (the full description of this procedure can be found in chapter 4). Moreover

magnetic field sweeps along a fixed direction can be performed. In that way it is possible to synchronize the voltage acquisition with the applied field value so that the depinning field can be electrically taken over. The AMR experiments are executed in a H_2O environment where beads are diluited with a concentration of $1\mu g/ml$. The variation of depinning field in presence or absence of bead over the DWs is exploited to detect and count the number of MNPs which transit on the top of the zig-zag (see chapter 5).

Impedantial sensors measurements

Capacitive sensors exploits an impedantial measurement to record the transit of MNPs diluted in a buffer saline solution (PBS). The fabrication of such sensors is described in section 3.1.4. The idea behind these detectors is the following: beads are trapped and manipulated applying external magnetic fields along the same magnetic zig-zag shaped nanoconduit used for the AMR sensors. When a MNP crosses a couple of electrodes, the low value of bead conductivity, compared to PBS, produces a voltage drop that can be measured.

Differently from AMR measurements, only two electrodes are involved (*two point probes technique*). The same HF2LI instrument is used to apply the electrical signal and to detect the electrical response. The applied voltage amplitude ranges between 100 mV and 500 mV and the frequence is set at 2 MHz. A schematic view of the equivalent circuit is illustrated in figure 3.16(a).

In that picture C_{DL} is the "double layer capacitance" which is formed at the interface between the electrical contacts and the saline solution. It is due to the ions in PBS that are attracted by the electrical field generated at the contacts extremities. This produce a charge accumulation that has to be taken into account. R_L is related to the conductivity of the liquid. It depends on the ions concentration and valence, together with the distance

between the electrodes immersed in PBS, which was set to 2μm.
The chip is affected by some parasitic capacitances due mainly to the interfaces between different material layers on the devices (see Fig.3.16(b)).

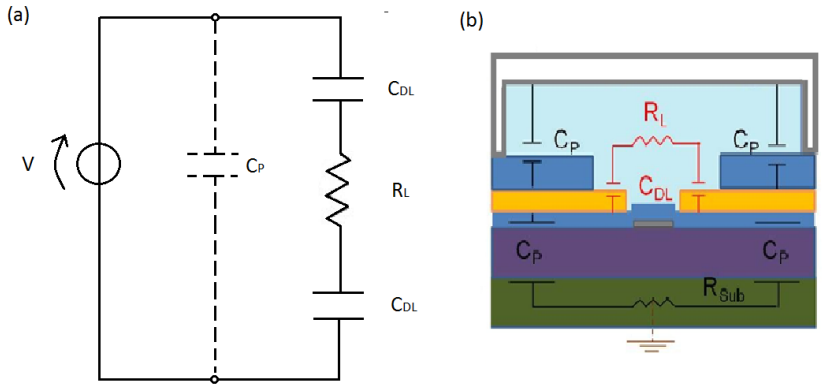

Figure 3.16: Equivalent circuit for capacitive sensors measurements (a) and schematic transversal section of the device (b).

At the working frequence, the effect of parasitisms has to be negligible, in order not to disrupt the electrical response. However an active compensation circuit can be used in order to eliminate all the capacitive effects not related to beads detection. A *Dammy circuit* was employed to this purpose (see chapter 5).
The magnetic nanoparticles manipulation is achieved using the same electromagnet described for AMR measurements, applying a rotating continuous field of 250 Oe. In this way an alternate sequence of head-to-head and tail-to-tail DWs in the zig-zag corners are simultaneously displaced along the corners in the conduit, driving the magnetic nanoparticles captured on the top. The experimental results concerning capacitive sensors are illustrated in chapter 5.

3.4 Micromagnetic simulations

Since the functionalities of magnetic DW conduits are strongly related to the geometry of the nanostrips, micromagnetic simulations were performed in order to study the magnetization equilibrium states and the magnetic force generated. Public OOMMF (Object Oriented Micro Magnetic Framework) platform has been used with the following parameters for Permalloy: saturation magnetization M_s =800*10^3 Am^{-1}, exchange stiffness constant A = 1.3*10^{-11} Jm^{-1}, damping coefficient = 0.5, no magneto-crystalline anisotropy has been considered. The damping coefficient is high, compared to the experimental one (0.01); this leads to a faster computation of the equilibrium state, that is what we are interested in, even though a lower accuracy in describing the transient behavior must be taken into account. A unit cell of 20 nm side and 10 nm high is used for the simulation of zig-zag shaped and curved conduits. This is greater than the exchange length of 5.2 nm but still the smallest ones compatible with the computational time. In chapters 4 and 6 the results of simulations are illustrated and discussed.

Chapter 4

Manipulation of nanoparticles over magnetic conduits

This chapter presents the results related to the implementation of an on chip magnetic based technology to trap and manipulate micro and nanoparticles over a surface in a microfluidic device. This technology, called domain walls tweezers (DWTs), can be potentially used for a large amount of interesting applications. It is a central part of this thesis work because it can be employed to control the position of magnetic beads in a 2D space with a high spatial resolution, down to 100 nm.
In this work, it is employed to bring MNPs in close proximity with a target cell, studying the interaction with the cellular membrane (see chapter 6) which is a fundamental aspect of the drug-delivery process. Curved geometries are used to this purpose.
Moreover, AMR and capacitive sensors exploits zig-zag shaped magnetic conduits to capture and transport magnetic nanoparticles while detecting their passage through a given point.
DWTs have been developed by the NaBiS group at L-NESS, in collaboration with Nanogune Center in San Sebastian [60] [59]. In the first part of the chap-

ter, a description of the optimization of a single particle manipulation over zig-zag conduits is performed. Instead, in the second part, curved structures are employed to achieve an innovative, simultaneous and controlled motion of a nanoparticles batch over a single chip.
The physics behind DWTs technology is fully discussed in chapter 2.

4.1 Single particles manipulation on zig-zag conduits

In order to magnetically control the transit of a bead over AMR or capacitive sensors, zig-zag shaped nanostructures are used. DWTs approach relies on the precise control of the motion of DWs that can be achieved in ferromagnetic stripes (magnetic conduits) and on the robust coupling between a DW and a magnetic particle in suspension over the conduits [58]. The injection and displacement of a single DW in a zigzag shaped stripe results in the capture and dragging of a particle. In order to create a DW in a magnetic conduit an injector pad is needed. The injector pad is the initial part and the element capable to inject the DW in the conduit. Starting from a mono-domain configuration, the injector pad, wider than the conduit, reverses its magnetization, upon the application of a small field, while leaving unchanged the conduit magnetization, thus creating a DW (see Fig.4.1). A sequence of magnetic fields propagates the DW from one corner to the following one, since every corner represents a pinning site for the DW. The magnetic particle, in suspension above the conduit, is dragged by the motion of the DW along the conduit. This reduces the average velocity of transportation which is limited by the diffusion of the magnetic bead from one pinning site to the following one.
In this thesis work, the zig-zag shaped conduits in AMR and capacitive sensors are made of Py, they have a width of 200 nm, a thickness of 25-35 nm

and the zig-zag segments are 2 μm long. The injector is 600 nm large and long 4 μm. In figure 4.1 a MFM image shows the single H-H DW (dark)

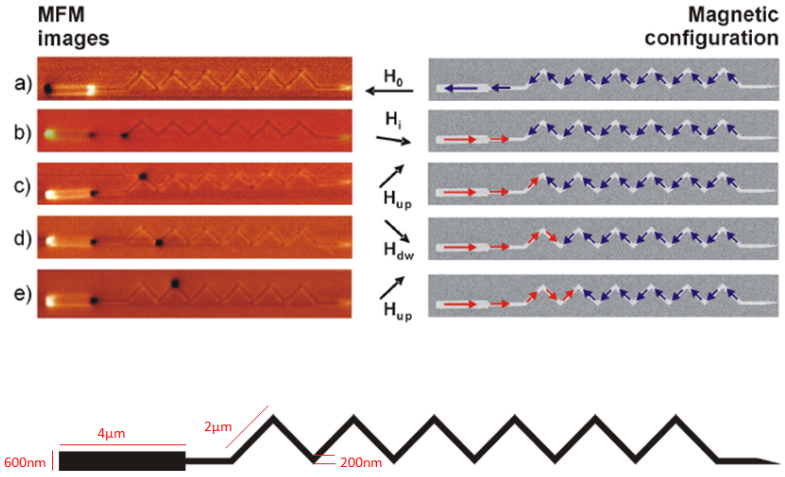

Figure 4.1: Top: sequence of magnetic force microscopy images and micromagnetic configurations (right) showing the injection and propagation of a domain wall under the action of external magnetic fields H_i, H_{up}, and H_{dw} directed as sketched in the figure. The dark and bright re contrast in the image is due to the inward and outward local stray fields. At the zig zag corners the stray field is generated by a domain wall, while in the case of the injection pad is only due to the magnetization stray field. Bottom: sketch of the zig-zag conduit dimensions.

nucleation and displacement applying a sequence of magnetic field pulses, 1 second long, in a specific direction. The applied field changes the magnetic configuration because the equilibrium condition is different due to the adding of an extra energy term (Zeeman interaction) to the total energy functional (see chapter 2). The sequence of field pulses applied to nucleate and displace a single DW is listed in table 4.1.

Field name	Field value [Oe]	Angle [^{o}]
H_0	1000	180^o
H_i	150±10	15^o
H_{up}	180±10	45^o
H_{dw}	180±10	-45^o

Table 4.1: Sequence of applied field pulses to nucleate and displace a DW in a zig-zag shaped conduit.

Experiments are executed in a wet environment: water (AMR sensors) or PBS (capacitive). A 0,5% (V/V) of SDS (Sodium Dodecyl Sulfate) which is a surfactancts based solution (soap) was added to reduce the friction and the non-magnetic interactions between beads and surface. *MyOne*^{TM} *dynabeads* with a diameter of 1 μm have been diluted to reach a MNPs concentration of 1μg/ml. The chip surface was previously treated with an Oxigen plasma to make it hydrophillic (3.1.3).

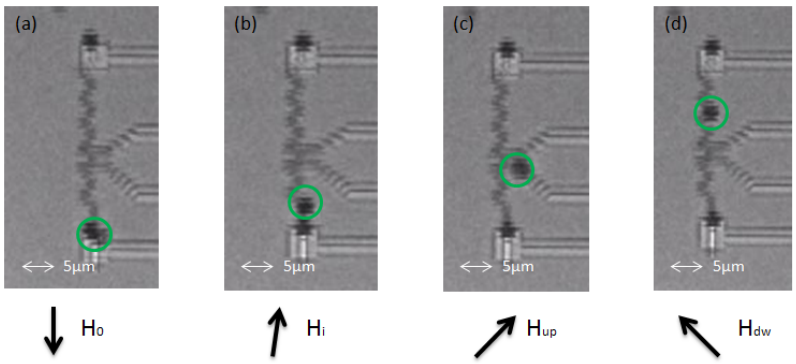

Figure 4.2: Transport sequence of a 1μm bead over a zig-zag shaped conduit in an AMR sensor. The DW is nucleated (a) and (b) and displaced over the nanostructure (c) and (d), dragging the MNP.

Figure 4.2 shows the displacement sequence of a single bead recorded by means of the optical microscope, applying the sequence of field pulses described in table 4.1. The electromagnet used to apply the magnetic field is described in section 3.3.2 together with the whole experimental setup.

4.2 Free 2D manipulation of many particles over curved conduits

The major limitation of zig-zag shaped nanostructures is that the particle is forced to follow the predetermined path of the conduit, even if more than one pathway is available [61]. In this paragraph a method for transporting magnetic particles without any a priori determined path will be presented which is based on array of nanometer sized rings of Py.
Such system allows to implement an innovative and simultaneous controlled motion of many particles thus achieving, an high parallelism in beads transport. In this way, some processes like the drug delivery to cell cultures could be not only well controlled, but also efficient.
In the following, the operation principles of this new manipulation technique will be illustrated and discussed.

4.2.1 Working principles

The basic element of the device is a soft-magnetic ring made of Py. The diameter of the designed and tested rings is variable between 5 and 10 μm, the width is 300 nm and the thickness ranges between 30 nm and 60 nm.
The pattern design consists of a matrix array of such rings. The design parameters are the diameter of the ring, its width and the minimum distance between neighboring rings. The rings are "packed" in two different ways: square matrices in which every rings has four neighbors and hexagonal

matrices in which there are 6 neighbours. The entire fabrication process is described in section 3.1.4. The total patterned area was 600 μm x 600 μm on a chip of 150 mm^2. The figure 4.3 shows the optical images of two portions of

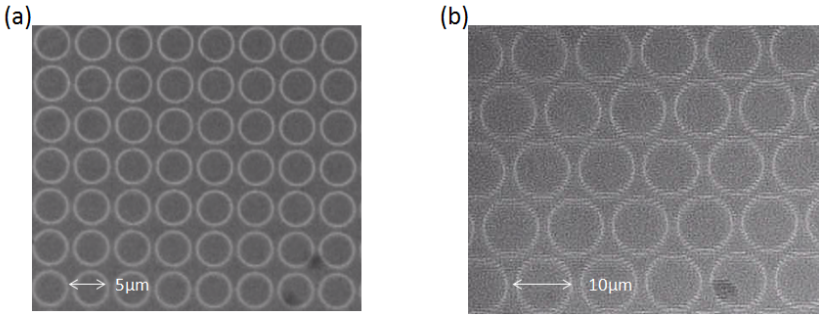

Figure 4.3: Square matrix (a) and hexagonal matrix (b) of Permalloy rings.

square and hexagonal arrays with rings of 5 μm (left side) and 10 μm (right side) diameter.

The distance between the center of two neighbor rings, is 6 μm for the left side array and 12 μm for honeycomb array of magnetic rings. The minimum distance between the four neighbours rings has been always chosen smaller than 2 μm with a lower limit of 1 μm. This parameter is fundamental for a correct and reliable manipulation of the beads. The elemental step of this manipulation method relies on the motion of beads over the magnetic rings with a geometry that allows the nucleation of two Neel magnetic domain walls.

By applying an in-plane external magnetic field (H_{sat}), two DWs, one HH and the other one TT, are generated. The DWs lie along the direction in which the field has been applied. As shown in figure 4.4 by the MFM images and by the sketch of the micromagnetic configuration, once created, the two DWs can be moved around the circumference by a smaller in-plane magnetic field H_R. By rotating the field, both the DWs rotate by the same angle, thus achieving smooth and fully controllable DW motion.

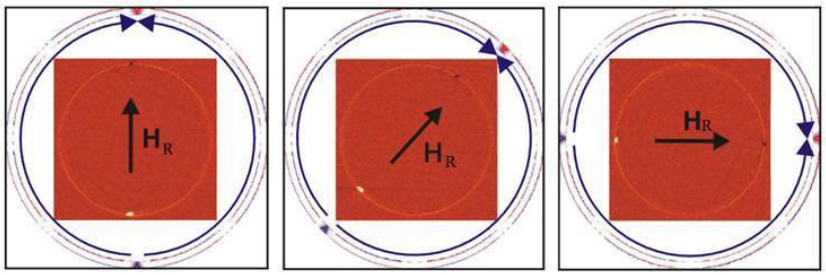

Figure 4.4: Outer figures: sketches of the micromagnetic configuration of a circular ring showing the nucleation and displacement along the perimeter of the two, HH and TT, DWs obtained by applying a continuous rotating field H_R. The inner images are the corresponding MFM data.[35]

However up to now, the manipulation is strictly confined on a single ring. In order to achieve a free 2D motion, an out-of-plane external magnetic field, called H_z, must be applied, in order to modify the magnetic potential landscape felt by the magnetic beads in suspension above the DWs. In the absence of an out-of-plane magnetic field, a superparamagnetic bead is equally attracted by the stray field emanated from the HH DW and the TT DW because it does not possess any spontaneous magnetic moment. This is at variance with what happens for the MFM tip, being coated with a hard magnetic material, which has a fixed magnetic dipole moment and thus is able to distinguish between the two DW type (white and black contrast). In fact, HH DW generates a magnetic stray field with a positive out-of-plane component, i.e. pointing outward; while the TT DW creates a stray field with a negative out-of-plane component, i.e. pointing inward. The application of an external magnetic field H_z, which can be considered homogeneous over the volume of the bead-DW interaction, increases the magnetic potential well created by the DW with the stray field parallel to the z-field. On the contrary, the potential well of a DW with stray field antiparallel to the external one is weakened. Furthermore, by properly choosing the intensity

of H_z, the total field (H_{TT}+ H_z) can cancel out the potential energy well felt by the magnetic bead, at the typical interaction distance. In this condition, even though the ring always possesses two DWs of opposite polarity, only one of them is able to trap a superparamagnetic particle in suspension.
In the following a simple system of two aligned magnetic rings separated by the same distance of the matrix is considered. This system represents the basic unit model to describe the free 2-dimensional manipulation method. The first step (see Fig. 4.5 (a)) is the application of an in-plane magnetic field H_{xy} in the -x direction and of a positive H_z field. The intensity of H_z is 60 Oe while, H_{xy} has a value of 300 Oe. This combination brings the magnetic

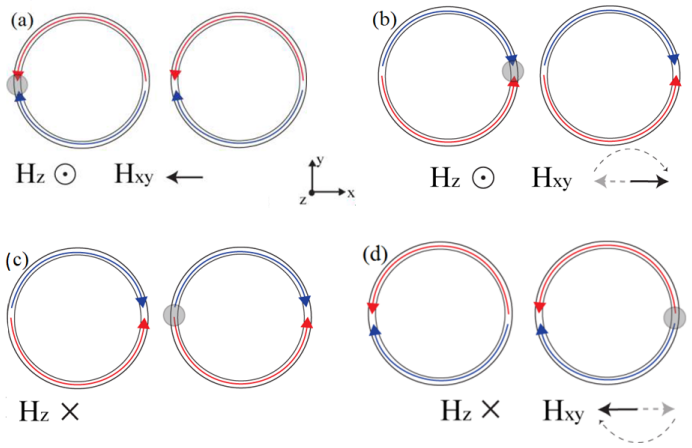

Figure 4.5: Schematic representation of the two rings system, after the application of the magnetic fields sketched below. Red and blue arrows show the micromagnetic configuration of the magnetic structures. Step (a): a magnetic bead, in grey, is trapped by the HH DW of the left ring. Step (b): the magnetic bead is moved to the point closest to the next ring. Step (c): by switching the polarity of the out-of-plane field and removing the in-plane field, the magnetic bead is attracted and coupled to the TT DW of the second ring. Step(d): the magnetic bead is moved by rotating again of 180^o the in-plane magnetic field.

rings in a state with two DWs but allows for the trapping of a bead only by the HH DW. Let's suppose now that the left ring of fig. 4.5 (a) captures a magnetic bead on its HH DW, as show in figure. By continuously rotating H_{xy} by 180^o the magnetic bead can be finely displaced to the opposite point of the ring, facing the neighboring structure. The situation, named step (b), in which the bead coupled to the HH DW is close to the TT DW of the other ring, is illustrated in figure 4.5 (b). In this condition the in-plane magnetic field H_{xy} is decreased to zero and the polarity of H_z is reversed, from positive to negative. This modifies the attractive potential landscape felt by the bead, that jumps from the HH DW to the TT DW of the next ring (figure 4.5 (c)).

Indeed, in this configuration the magnetic potential well of the HH DW is now negligible while the TT DW becomes strongly attractive and drags the magnetic bead on the right. This is possible because the new attractive well is spatially close enough to the bead for capturing it. After that, the in-plane field H_{xy} is restored and can be continuously rotated by other 180^o in order to displace the bead to the diametrically opposite site of the second ring. The situation is illustrated in figure 4.5 (d).

Upon application of this sequence of fields, the bead undergoes a displacement of approximately two ring diameters. The key point of the method is the switching of the polarity of H_z which allows for the jump of the bead from a structure to the closest one, so that the bead motion is no longer limited to a rotation along a single circular ring but, in principle, to the whole rings-patterned space. The example illustrated before shows the way for moving along a linear array of rings. However, in a squared matrix of rings any of the four directions ($\pm$x,$\pm$y) in the 2-dimensional plane can be addressed by rotating the magnetic field H_{xy} by 180^o and 90^o respectively. In an hexagonal matrix, instead, 6 different directions are allowed by rotating the in-plane field of a multiple of 30^o.

4.2.2 Micromagnetic simulation

In the previous section, the free 2-dimensional manipulation method has been illustrated and discussed qualitatively. However, in order to understand deeply the physical mechanisms at the basis of the presented method, a more quantitative analysis has been carried out.

The most critical step in the manipulation process is the decoupling between the bead and the underlying DW, and the subsequent coupling with the DW of the next ring.

By means of OOMMF simulations, the micromagnetic configuration of two adjacent magnetic rings was studied, upon saturation with a strong in-plane magnetic field (500 Oe). The two simulated rings are made of Py, have a diameter of 5 μm and a width of 300 nm. The paramters used in the simulations are listed in section 3.4. The minimum distance between the two rings is 1 μm along the x axis. The saturating magnetic field creates a couple of DWs in both rings, in order to obtain two DWs facing each other. Upon the application of the field the magnetic spin structure of the DWs assumes a "vortex" configuration due to the balance between the shape anisotropy of the structures and the magnetostatic energy contribution (see fig.4.6).

In particular, in the area of interest where the two rings are closer, we obtain a vortex-like DW with a HH feature on the right ring and a vortex-like DW with a TT feature on the left ring, as it is illustrated in figure 4.6. The image displays the magnetization inside the two adjacent rings upon the application of a strong saturating magnetic field in the x direction in the case of no out-of-plane magnetic field. The tendency to close the field lines of the magnetization on the upper and lower part of the two arches of the rings is an artifact due to the finite area of the simulation which did not consider the entire ring.

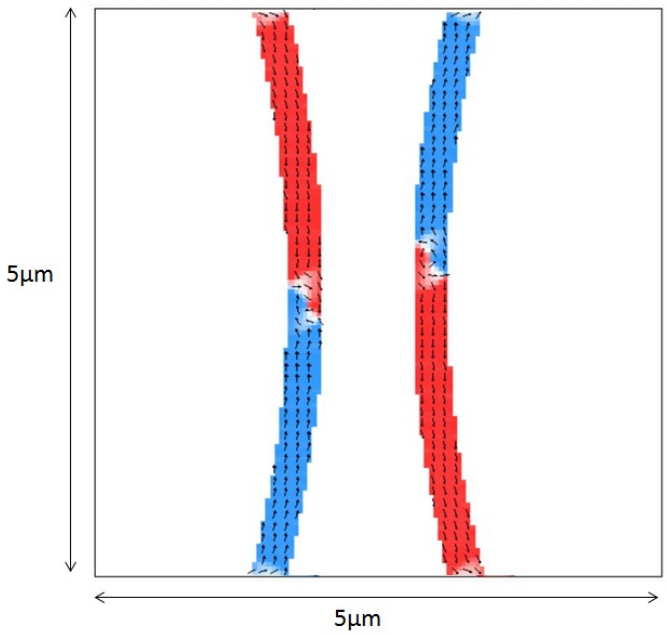

Figure 4.6: OOMMF simulation of the magnetization of a portion of the two rings facing each other from OOMMF. The arrows show the direction of the magnetization in the xy-plane. Blue and red pixels indicate positive and negative values of the magnetization along y. HH and TT vortex DWs are nucleated by an external in-plane field (500 Oe).

The simulations show that, applying an out-of plane field H_z of 60 Oe, the nanostructures produce a stray field H_{dw} only slightly different (within 5 Oe) from the case without H_z. Nevertheless the total magnetic field $H_{tot} = (H_{dw+} H_z)$ is directly affected by H_z and it can even change sign when H_z is applied. This is illustrated in figure 4.7 where the maxima in absolute value of the z-component of the total field are plotted with respect to the z position. The total field near the HH vortex DW is positive and increased by H_z. The total field near the TT vortex DW is instead negative and the application of H_z reverses its polarity at a distance of 400 nm.

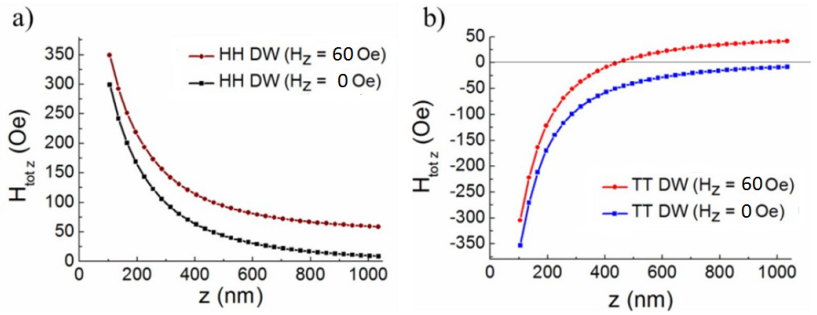

Figure 4.7: a) z-component of the total field generated close to the HH DW with respect to the vertical distance z from the magnetic structure. The field near HH DW is positive and is enhanced by the application of the concordant external field. b) z-component of the total field generated close to the TT DW versus z. In absence of H_z, the vertical component of H_tot is negative while upon the application of the out of plane external field, H_tot crosses the zero value at a certain distance (around 400 nm).

This leads to a modification of the magnetic potential energy and ultimately of the force exerted on a magnetic bead by the DWs in that spatial region. From the total field H_{tot}, the magnetic interaction energy is calculated via MatLab for different values of H_z. The magnetic potential energy has been calculated through the following equation:

$$E_b = -\mu_0 \int_V \mathbf{m}_b \cdot \mathbf{H}_{tot} dV \tag{4.1}$$

where m_b is the induced magnetic moment of the superparamagnetic particle of volume V. The magnetic bead, acting as a probe of the magnetic interaction, has a diameter of 1μm and a magnetic susceptibility χ of 0.39. The magnetic potential energy has been valuated in a plane at constant height h_z equal to the radius of the bead plus 50 nm, which represents the typical

experimental distance of a particle from the magnetic conduits because a capping layer of 40-50 nm is deposited on the top of the structures.

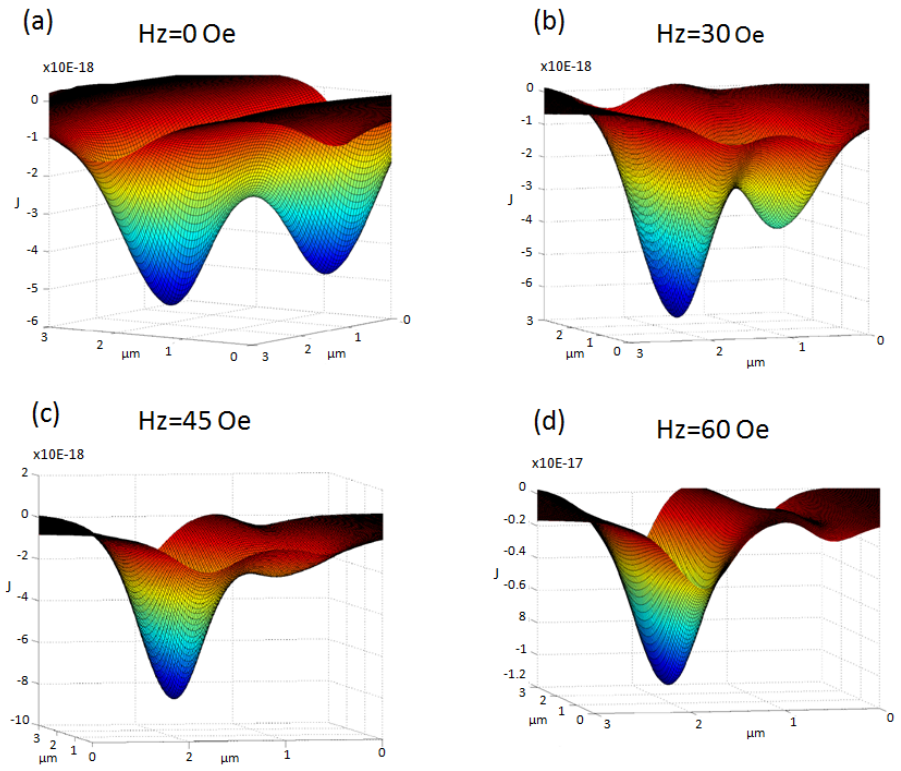

Figure 4.8: Magnetic potential energy wells felt by 1 μm superparamagnetic particle generated by the magnetic configuration illustrated in figure 4.6 for different values of H_z. When H_z is off, HH and TT DWs produce two equally deep potential wells. While, increasing H_z, HH DW becomes a stronger attractive pole and TT DW a weaker one. When H_z is equal to 60 Oe the particle is completely decoupled by TT DW.

Figure 4.8 shows the profiles of potential energy landscapes varying H_z. In the absence of H_z the two magnetic potential wells related to HH and TT DWs are almost equal in shape and intensity. At a distance of 50 nm from the surface (which is the thickness of the capping layer), the minimum of the wells is around $6.0*10^{-18}$ J. When the out-of-plane field is switched on, the

equilibrium between the DWs is broken and the potential well generated by the HH DW is greatly deepened ($1.1*10^{-17}$ J). On the contrary, the potential well created by the TT DW is weakened by the external field down to a value close to 0. Applying a H_z of 60 Oe (the optimal value) the coupling of a magnetic bead to the TT DW is unfavorable with respect to the coupling to the HH DW.

A valuation of the force exerted on the magnetic bead is simulated through Matlab according to the following equation:

$$F = -\mu_0 \chi \int_V \mathbf{H}_{tot} \cdot \nabla \mathbf{H}_{tot} dV \tag{4.2}$$

where the magnetization of the superparamagnetic bead is written as χH_{tot}.

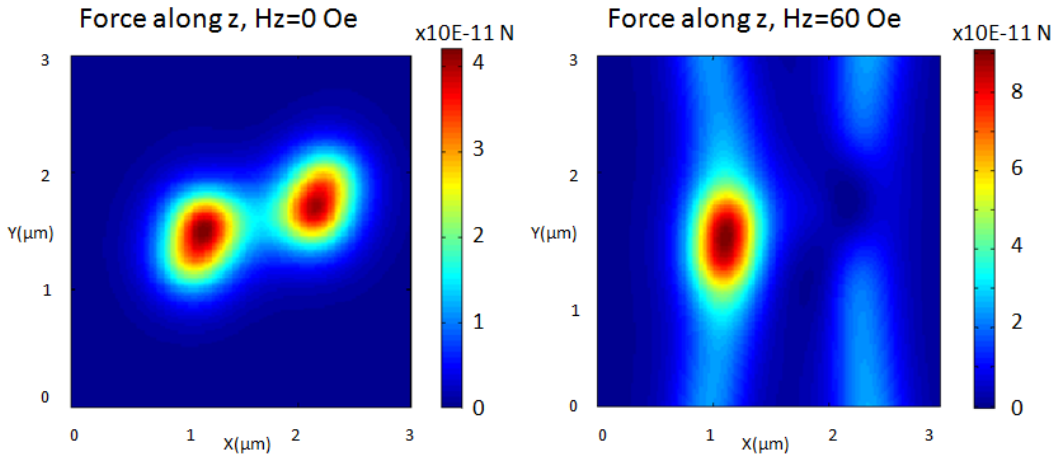

Figure 4.9: Contour plot of the z-component of the magnetic force calculated at a distance equal to the radius of the bead plus 60 nm. The left graph illustrates the situation when the out-of-plane magnetic field is off while the right graph shows the case in which the force generated by the HH DW is enhanced by a H_z field equal to 60 Oe.

Figure 4.9 shows the force value along z, comparing the situation with H_z equal to 0 Oe and 60 Oe. Without an out-of-plane field, the force suffered

by the MNP is almost the same for HH and TT DW, that is 43 pN. Instead, if H_z is 60 Oe, the HH DW produce a higher attracting force of 89 pN while the TT DW a lower force equal to 5 pN.

Finally, figure 4.10 illustrates the x-component of the magnetic force on the bead, which is the dragging force making the bead to "jump" from one ring to the other. For H_z set to 0, HH and TT DWs are attracting poles for the MNPs. Instead, if H_z is equal to 60 Oe the bead is decoupled from the TT DW and it is strongly attracted by HH DW.

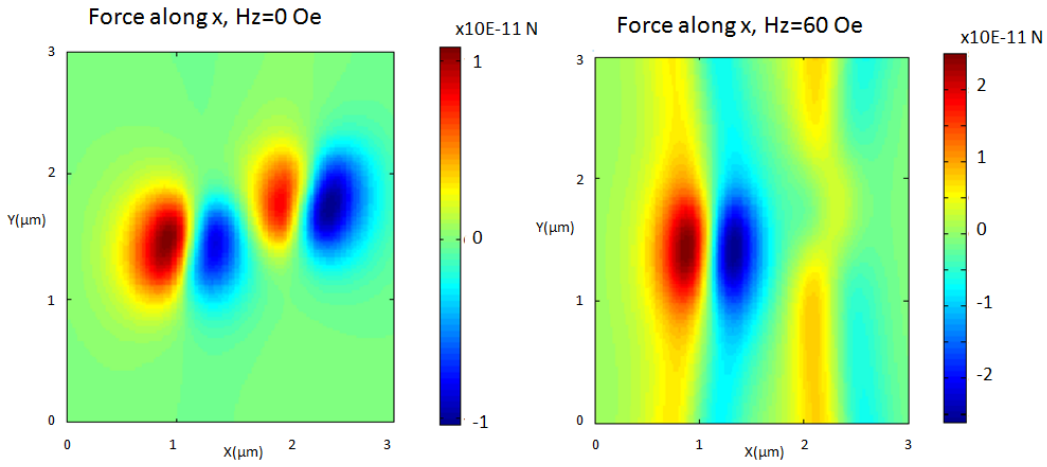

Figure 4.10: Contour plot of the x-component of the magnetic force calculated at a distance equal to the radius of the bead plus 50 nm. The left graph illustrates the situation when the out-of-plane magnetic field is off while the right graph shows the case in which H_z is equal to 60 Oe.

4.2.3 Manipulation of a particles batch on free paths

Magnetic array of rings made of Py have been employed to achieve a simultaneous and synchronized manipulation of a magnetic beads batch in solution over the patterned substrate. For all the experiments of free manipulation, superparamagnetic beads with 1 μm diameter (myOne^{TM}, Invitrogen) and COOH surface functionalization have been used. The arrays were fabricated on Si/SiO_2 chips (15 mm X 15 mm) and covered by 30-50 nm of SiO_2. Moreover an oxigen plasma has been used in a plasma asher machine to make the surface hydrophillic (see 3.1.4). The experimental setup is described in section 3.3.1. The stepper motors system is used to apply the in-plane magnetic field of 300 Oe (enough to nucleate and displace DW over the single ring). The out-of-plane magnetic field is generated by a hollow cylindrical coil placed around the objective of the the microscope and connected to a generator, controlled via a labview software. It can provide a magnetic field up to 100 Oe.

The experiments have been executed in a wet environment of D.I. water and SDS (Sodium Dodecyl Sulfate) at 0.5% (V/V) employed to reduce the friction between particles and surface. Beads are diluited to reach a concentration of 1-5 μg/ml.

The manipulation of MNPs has been monitored by the optical microscope in the Bright Field (BF) mode.

Once beads are sedimented on the surface, they are trapped by DWs and they can be displaced over the single ring by rotating the in-plane field (generated by the permanent magnets) through the stepper motors system (see 3.3.1). Figure 4.11 shows the motion of a captured bead by applying a rotating field of 300 Oe.

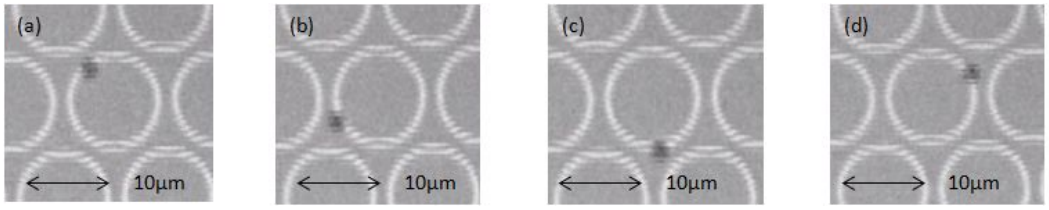

Figure 4.11: Manipulation sequence of a single 1μm bead around a magnetic ring in an hexagonal matrix by applying a 300 Oe in-plane field. The magnetic field is rotated in an anti-clockwise direction. The images are recoded from an optical microscope exploiting a 60x immersion objective.

In order to achieve the decoupling of MNPs from HH or TT DWs, a negative or positive value of H_z has been applyed. H_z is switched from a positive value of 60 Oe to a negative one of -60 Oe (or vice versa) to allow a "jump" of the particles from one ring to the adjacent one, as deeply discussed in the previous sections. Note that there is an intrinsic uncertainty on the value of H_z ($\pm$30 Oe) due to the out-of-plane component generated by permanent magnets which are used to apply the in-plane field. They are located just under the sample stage (see 3.3.1) so that they create a small out-of-plane field (maximum 30 Oe) which has to be compensated by the coil field in order to achieve the 60 Oe value.
However, the combination of the in-plane and the out-of-plane fields permits to manipulate the particles all over the 2-dimensional space. If more than one particle is captured by the DWs in different rings, it is possible to synchronize the motion of such particles along parallel paths. This happens because the potential energy landscape is periodic and it is the same for each ring. A modification of such landscape by an external field will simultaneously affect all the beads.

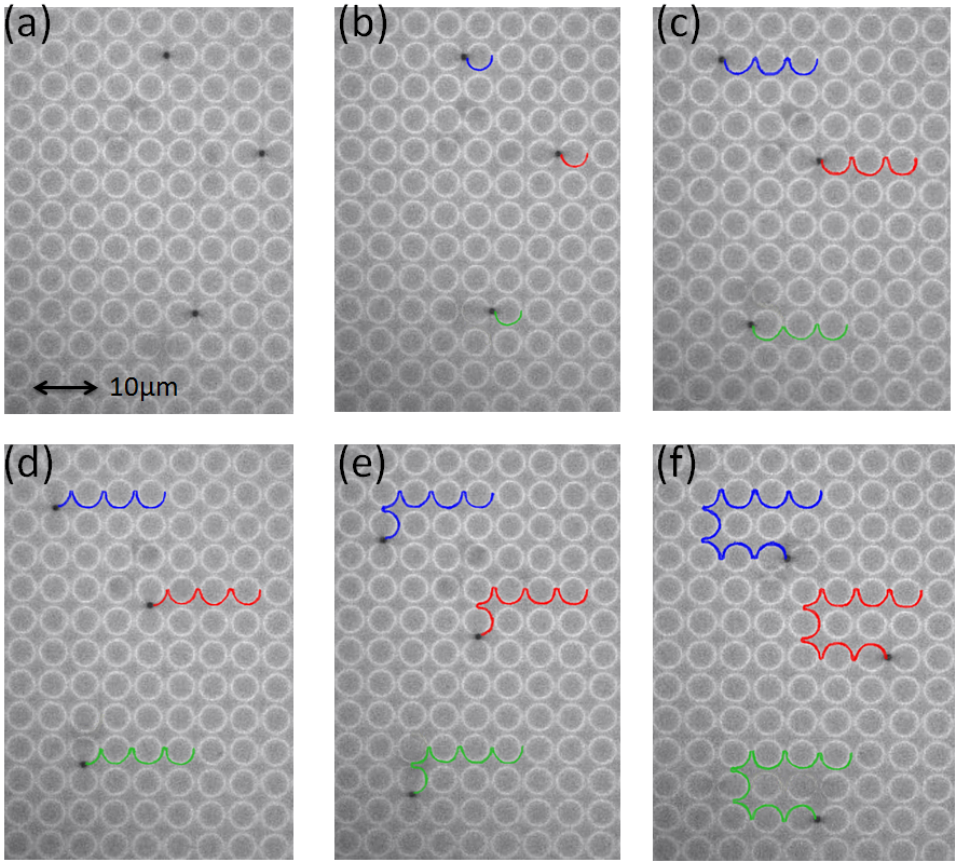

Figure 4.12: Optical microscope images of a particles batch manipulation. The particles path is highlighted with different colour. A 60x immersion objective and 1μm beads are employed.

In figure 4.12 a sequence of the synchronized manipulation of 3 beads is illustrated. Again, the in-plane field is employed to displace the DWs in the curved conduit, dragging the particles where the adjacent rings are closer. H_z is switched from a negative (-60±30 Oe) to a positive value (60±30 Oe) or vice versa, so that particles are decoupled by TT DWs and attracted by HH DWs (or vice versa). From that point the process is repeated.

4.3 Conclusions and perspectives

In this chapter a method to achieve a synchronized and controlled manipulation of many particles over curved conduits in a 2-dimensional space has been developed and demonstrated.

The future perspective could be the complete automation of such method: drawing a random path on a PC, a sequence of fields can be automatically applied to drive the particles along the desired path. Moreover, this technology should be tested and optimized for different biological applications such as drug delivery.

Chapter 5

Detection methods for magnetic nanoparticles

In this chapter a description of the results related to the detection of MNPs by means of AMR and capacitive sensors is presented. The recording of beads transit is a fundamental topic of this thesis work because it allows to count the number of particles which flow in a microfluidic channel and whose motion is activated by DWs propagating in magnetic conduits within such channel. In this way, for instance, a controlled amount of particles (loaded with specific drugs) could be administered to target cells (see chapter 6), according to the general scheme presented in the introduction of this thesis. In the first part of the chapter the performances of AMR sensors placed along a magnetic conduit to detect the transit of a single particle will be discussed. Instead, in the second part, capacitive sensors will be presented. A detailed description of the fabrication process for each class of devices can be found in chapter 3, together with an illustration of the measurements setups.

5.1 AMR sensors

AMR sensors are employed to detect the transit of MNPs, over a magnetic conduit exploiting an impedance variation on the portion of the conduit where the particle is passing due to the *Anisotropic Magnetoresistance* effect (see section 2.3)

The sensors are zig-zags shaped nanoconduits made of Py, with 200 nm of width, 25 nm of thickness and segment length of 2 μm. The injector pad is 600 nm large and 4 μm long. Additional Au electrodes, 500 nm wide, are also patterned under the magnetic conduits to perform the electrical measurements. Fig.5.1 shows a microscope image of the device.

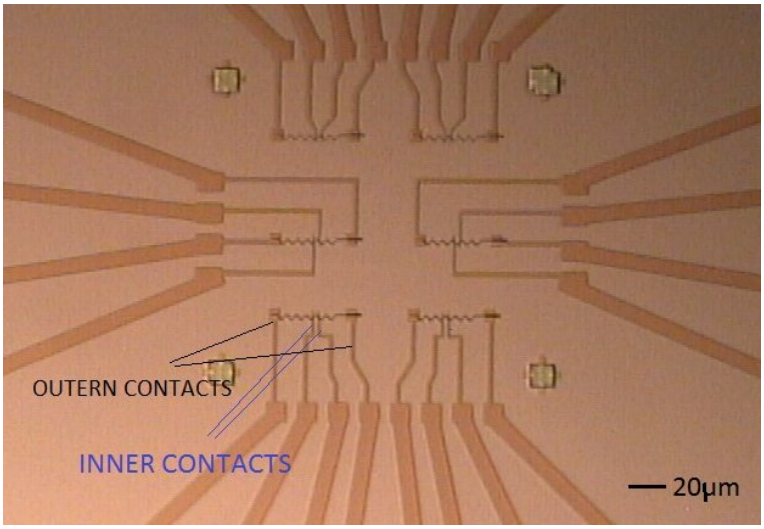

Figure 5.1: Optical microscope image of an AMR chip: the zig-zags magnetic structures are illustrated, together with the four electrical contacts for each sensor.

The fabrication has been made by EBL and optical lithography; after the evaporation of Py and Au, the lift-off procedure was employed to dissolve the resist. The chip was finally capped by 40-50 nm of Al_2O_3 or SiO_2 to prevent nanostructures from damages due to the liquid and it is equipped

with a PDMS gasket to contain the fluid. The entire fabrication process can be found in section 3.1.4.

The device presents 6 sensors, each one provided with 4 electrodes that are used to apply and record signals from the zig-zag conduit (see Fig.5.1). Two inner electrodes are used to measure the electrical signal, while the outer contacts are employed to apply the external potential.

Zig-zag conduits are used to nucleate and displace a single DW thanks to the application of external field pulses, as discussed in paragraph 4.1. The nanoparticles attracted by the stray field arising from the DW are dragged over the zig-zag structures (see Fig. 4.2).

The AMR effect allows to electrically detect the crossing of the DWs between two electrical contacts. In fact, the resistance of a magnetic and conductive material (such as Py) is affected by the relative orientation between the magnetization vector $\mathbf{M}$ and the flowing current density $\mathbf{J}$. In particular, almost the totality of materials present a resistivity for $\mathbf{M}$ parallel to $\mathbf{J}$ ($\rho_{\parallel}$) bigger than the resistance for $\mathbf{M}$ perpendicular to $\mathbf{J}$ ($\rho_{\perp}$). In this way, if the magnetization vector $\mathbf{M}$ is directed perpendicular to the flowing current density $\mathbf{J}$, a lower value of the voltage drop across a magnetic structure is measured compared to the case in which the magnetization points in the same direction of the current.

In zig-zag shaped nanostructures of Py, the magnetization vector is spontaneously oriented in the same direction of the conduit, in order to minimize the total energy of the system (shape anisotropy is the leading contribution -see section 2.1.6-). On the contrary, the DWs nucleated in such structures, are transverse Neel walls with $\mathbf{M}$ locally perpendicular to the conduit as illustrated in Fig.5.2.

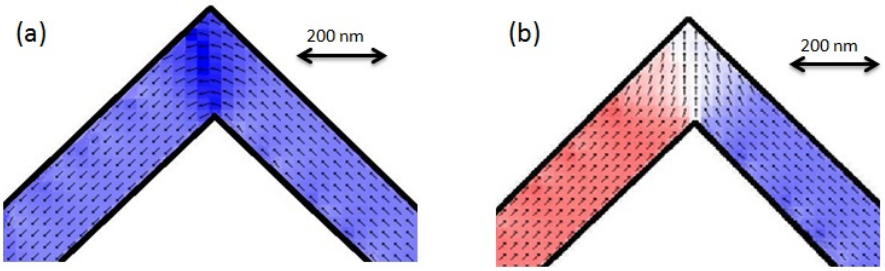

Figure 5.2: Magnetization of a zig-zags shaped conduit corner, in absence (a) or presence (b) of a DW. The arrows indicate the direction of M. Red-white-blue pixels indicate the value of M along the x-axis.

In this way, if a DW is nucleated and positioned on top of the corner located between the inner electrical contacts of our device, the resistance of the corner decreases and a lower voltage drop is measured as depicted in figure 5.3. This procedure permits to electrically detect the transit of a DW.

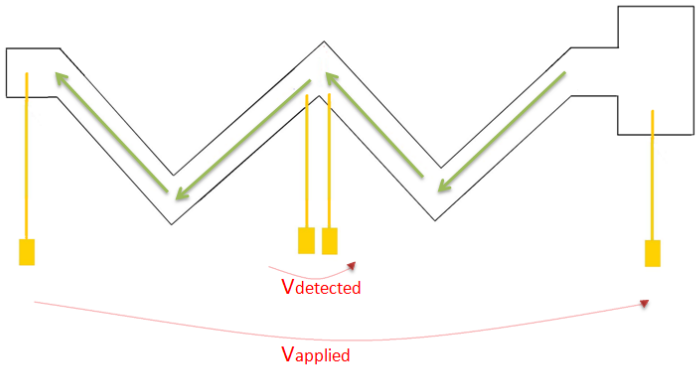

Figure 5.3: Sketch of the AMR sensor. The internal electrodes are employed to measure the voltage drop at one corner of the magnetic zig-zag conduit. The external contacts are exploited to apply the electrical signal. The green arrows represent the current which flows in the device.

The detection of the transit of a MNP bound to said DW is more complex, essentially because the variation of the DW micromagnetic configuration due to the magnetic nanoparticle is not enough to produce a measurable variation of the impedance across the corner. In this case a simple voltage measurement is not sufficient. However, when a particle is trapped over a DW, a different value of the depinning field is measured. The depinning field H_{dep} is the lowest magnetic field that is required to displace a DW from one pinning site to an adjacent one. In a zig-zag shaped structure, it is the minimum field to move a DW from one corner to another.

When a bead is placed over a DW at one corner in the zig-zag nanostructure and the magnetic field H_{dep} is applied to displace the DW along one conduit segment, an additional magnetic dipole moment field μ is generated in the superparamagnetic bead. The stray field generated by μ opposes the applied field below the bead, causing an increase in the value of the field H_{dep} required to displace the DW as illustrated in figure 5.4. This discrepancy in the value of H_{dep} can be used to distinguish the presence of a MNP over a DW.

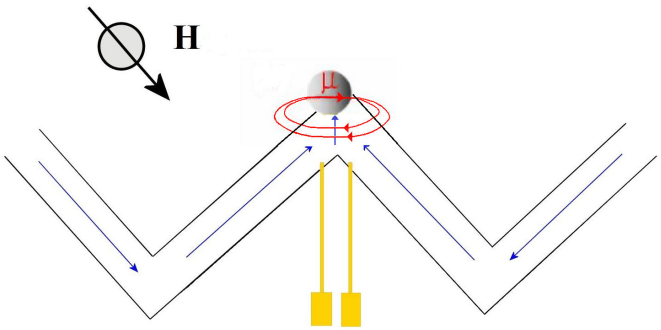

Figure 5.4: Sketch of the zig-zag conduit in an AMR sensor. A magnetized bead of moment μ produces a stray field in the upper corner of the conduit.

In this way, a synchronized measurement of the voltage drop and the H_{dep} value is employed to count the number of beads which transit between the electrodes.

5.1.1 Detection experiments

The experiments have been carried out exploiting the setup described in section 3.3.2. A four probes technique is employed. The inner contacts (see fig.5.1) are used to record the voltage drop across the corner, while the outer contacts are supplied by an AC voltage, with an amplitude of 50-200 mV and a frequency which ranges between 10-100 kHz. The output signal from the inner contacts was demodulated by a lock-in amplifier, in order to increase the signal to noise ratio.

The magnetic field is applied by means of a four poles electromagnet which generates an in-plane magnetic field that can be finely controlled in direction and absolute value (up to 700 Oe). The experiments have been executed in a wet environment of D.I. water and SDS (Sodium Dodecyl Sulfate) at 0.5% (V/V) to reduce the friction between particles and surface. Superparamagnetic beads with 1 μm diameter (myOne^{TM}, Invitrogen) and COOH surface have been used. They are diluted to reach a concentration of 1 μg/ml.

The frequency of the AC signal was set to a relative high value because it permits to better reduce the electric noise (thanks to the lock-in). Moreover, the impedantial spectra of the device shows a smooth and constant value of R for a frequency lower than 200 kHz, as shown in Fig 5.5.

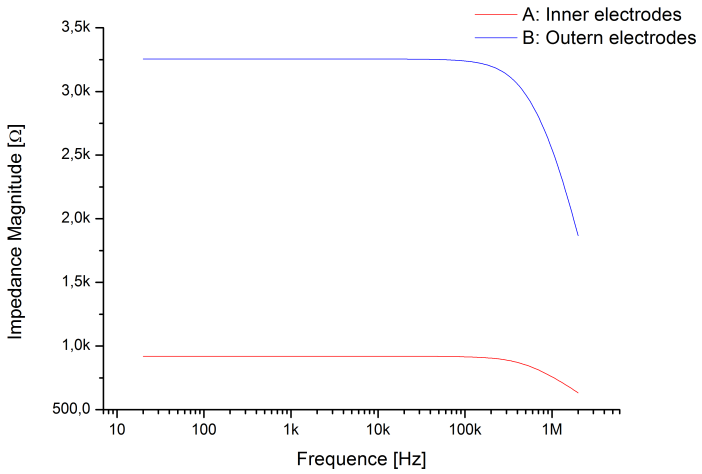

Figure 5.5: Impedantial spectra of the AMR devices, measured by LCR. Curve A represents the resistance between the inner electrodes, while B the resistance between the outer contacts.

The impedantial spectra were measured exploiting an *LCR Agilent E4980A*. The current which flows in the device ranges between 1-4 μA. The applied voltage was set not to exceed 4 μA which is the upper limit of the current, in order to avoid the disruption of contacts by Joule effect. The equivalent circuit can be found in Fig.3.15

The first part of the experiment was carried out in absence of MNPs. A single DW is nucleated and displaced by applying a sequence of field pulses as discussed in section 4.1. Once the DW is located at the corner preceding the inner electrical contacts (see Fig.5.6(a)), we made a sweep of magnetic field (0-300 Oe), applied in the direction of the segment leading to the corner surrounded by the electrodes. When the value of H_{depIN} =179.5±2 Oe is reached, the DW is depinned and jump to the corner sandwiched by inner electrodes so that a lower voltage drop is measured due to AMR.

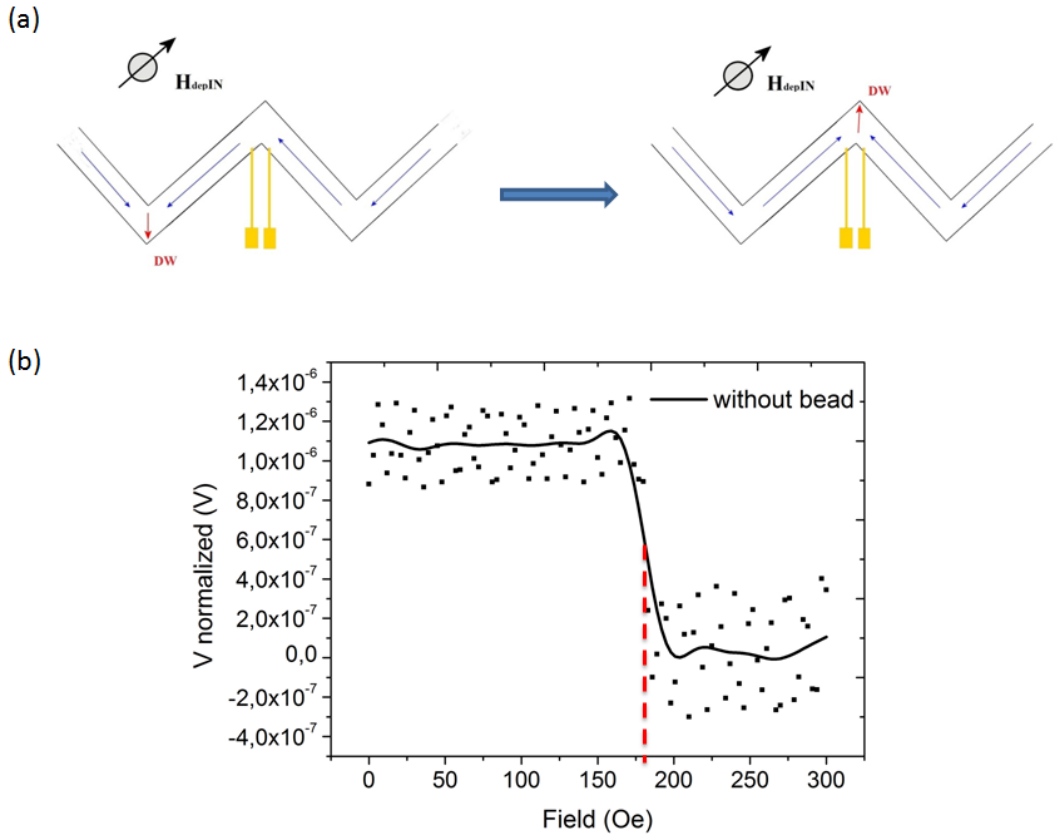

Figure 5.6: Sketch of the displacement of a DW to the corner between the inner contacts in AMR sensors (a) and plot of the voltage drop due to AMR as a function of the external field. At 179.5±2 Oe (indicated by the red-dashed line) the DW is displaced (b). The dots represent the experimental values, while the continuous line is a polynomial fit of the data.

The anisotropic magnetic resistance has been quantified for the employed device, as the maximum percentage variation of the resistance when passing from parallel to perpendicular orientation of **M** and **J**. The results show a voltage variation (V_{AMR}) of 1.1±0.2 μV over a baseline of 175±10 μV before the DW jump. It corresponds to a percentage variation of the resistance of around 0.6 %.

In figure 5.7 another field perpendicular to the previous one is applied to displace the DW to the corner beyond the electrodes. During this sweep an increase in the voltage drop is measured when the depinning field H_{depOUT} reaches a value of 180±2 Oe.

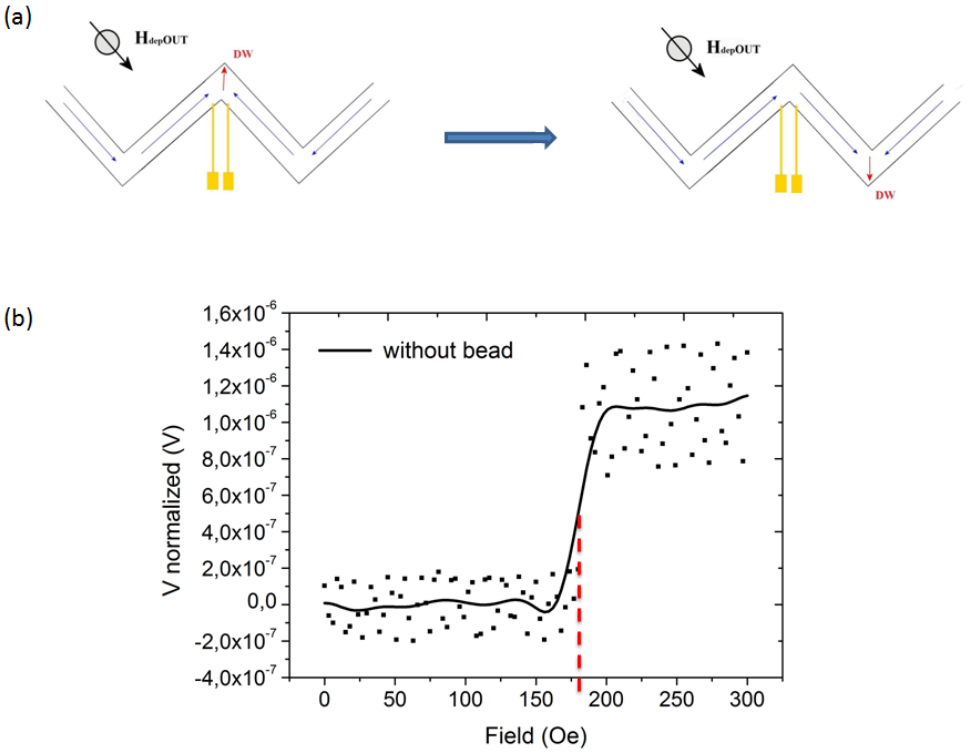

Figure 5.7: Sketch of the displacement of a DW beyond the inner contacts in AMR sensors (a) and plot of the voltage drop by AMR as function of the external field. At 180±2 Oe, (indicated by the red-dashed line) the DW is displaced (b). The dots represent the experimental values, while the continuous line is a polynomial fit of the data.

Even if the direction of H_{depIN} and H_{depOUT} is different, the absolute value is almost the same, as it can be expected by the symmetry of the conduit. The same experiments have been executed adding the MNPs (1 μg/ml) in

solution and trapping one bead over a DW. Particles are manipulated over the zig-zag shaped conduit as it is illustrated in fig.5.8. The presence of

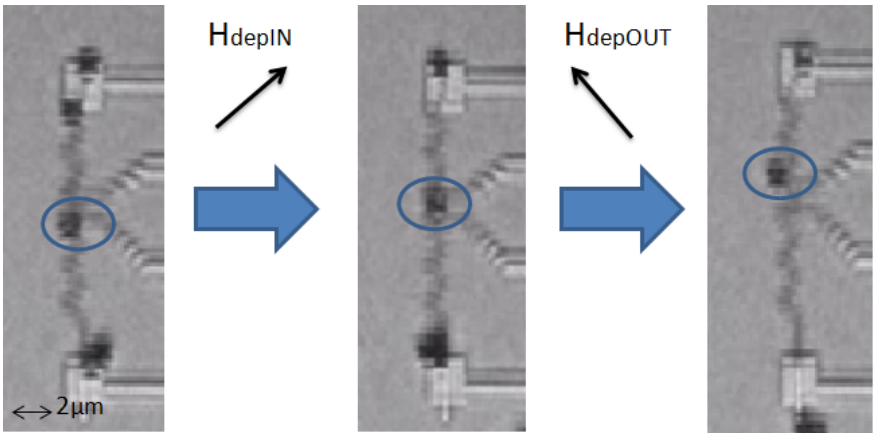

Figure 5.8: Optical microscope image of 1 μm bead transition between the inner contacts in an AMR sensor. An immersion objective 60x has been employed.

beads over DWs change the depinning field value (as discussed in the previous paragraph). Figure 5.9 shows the variation in the voltage drop as function of the applied field when a bead is displaced to the corner between the contacts (a) or outside from it (b). In this case, H_{depIN} =193.5±2 Oe and H_{depOUT} =195±2 Oe. Again, a sweep of magnetic field (0-300 Oe) is applied to move the DW. A noticeable increase of H_{depIN} and H_{depOUT} is measured in presence of beads. The variation of the depinning field is ΔH_{depIN} =14±3 Oe and ΔH_{depOUT} =15±3 Oe. This is illustrated in figure 5.9(c). In this way, if H_{dep} in presence and absence of beads is known, it is possible to precisely record and detect the number of beads crossing between the electrical contacts.

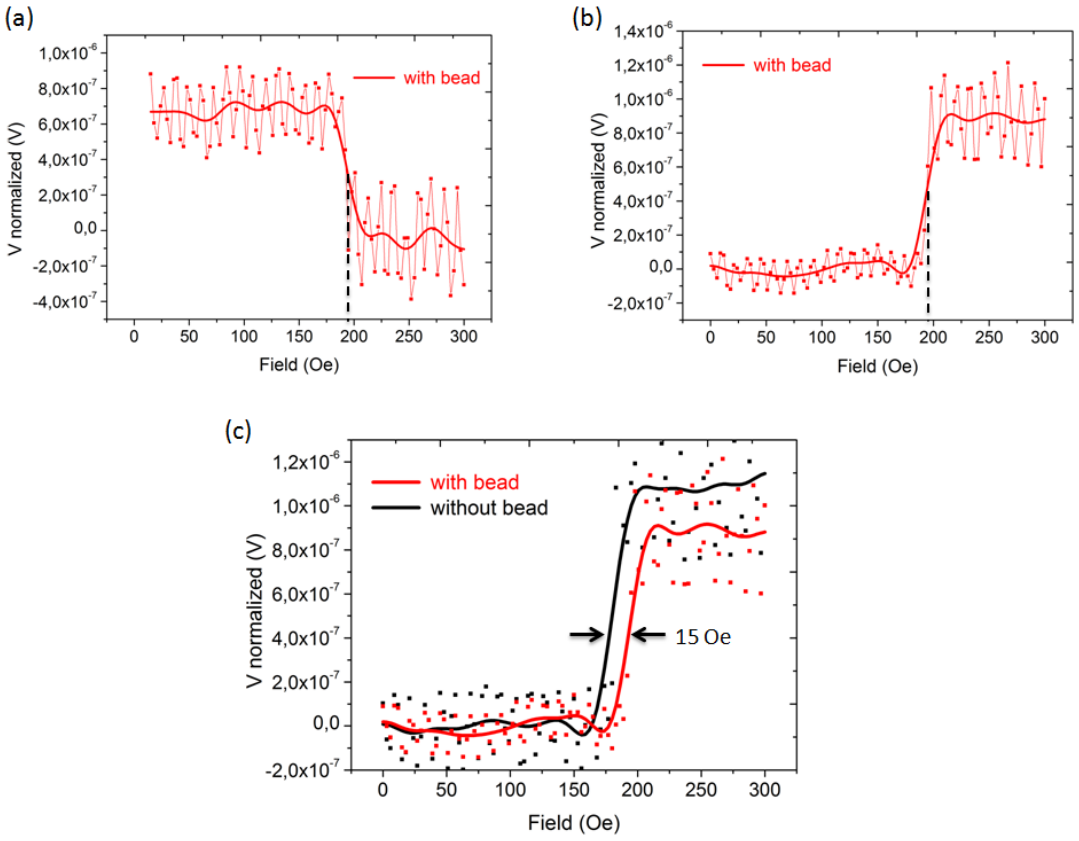

Figure 5.9: Plots of the voltage drop as function of the applied field when the bead is displaced inside (a) or outside (b) the contacts. Panel (c) compares two curves which represent the voltage variation when a DW is displaced outside from the inner contacts in presence (red line) and absence (black line) of a MNP on the top of it. The fine lines and dots represent the experimental values, while the thicker continuous line is a polynomial fit of the data.

It can be observed from the graphics how the measurements are affected by a periodic electrical noise which doesn't significantly alter the experimental results. The SNR (signal to noise ratio) is around 3, calculated as follows: $SNR = V_{AMR}/V_{NOISE}$ where V_{AMR} (1.1±0.2 μV) is the voltage variation passing from parallel to perpendicular orientation of **M** and **J** and V_{NOISE}

is the amplitude of electrical noise signal (0.35±0.1 μV). The electrical noise is a periodic signal mainly due to a spurious effect of the lock-in that can't be eliminated with the current setup. The "Electronic engineering group" is actually developing a dedicated lock-in able to reduce such noise figure.

5.2 Capacitive sensors

Capacitive sensors exploit an impedantial measurement to detect the transit of a bead between two electrical contacts. The idea behind these detectors is the following: the conductivity of magnetic beads is much smaller than PBS (Phospate Buffer Saline) conductivity (σ_{PBS} =1.5 S/m) and consequently when a bead, diluted in PBS, transits between two electrodes, a voltage drop is measured. The controlled motion of MNPs between the electrodes is achieved by means of the well known zig-zag shaped conduits which allow to trap and displace nanoparticles applying a sequence of magnetic fields.
In the next paragraph a preliminary experiment will be described; it is executed to valuate the impedantial response of beads. Finally, in the last section of this chapter, the preliminary results related to capacitive sensors will be presented.

5.2.1 Beads Impedance

A first experiment has been carried out to estimate the impedantial response of the magnetic nanoparticles. In fact, capacitive sensors are founded on the idea that beads behave as insulating body or, at least, they present a much lower conductivity compared to PBS. The goal of this paragraph is to confirm this assumption. 1μm MNPs (myOne^{TM}, Invitrogen) and 2μm (micromer-M-Streptadivin, Micromod) have been tested. The impedantial measurement is performed through a simple microfluidic device which exploits bigger electrodes compared to the capacitive sensors described in the next section and

employed for the final experiment. Once MNP, diluted in PBS, are sedimented between such electrodes an external permanent magnet is used to attract them far from the contacts and, a variation of impedance is measured through an LCR meter. A quantification of the resistance variation permits to calculate the impedantial effect of a single bead if the concentration of the particles is known. This chip is made by a glass substrate patterned with Au

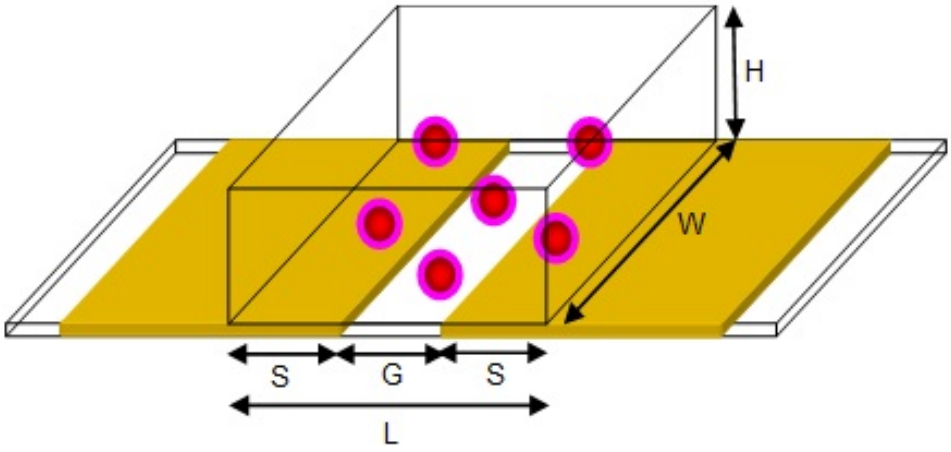

Figure 5.10: Sketch of the electrical contacts in the measurement area of a capacitive device. W=3 mm, G=4 μm, S=4 μm, H=1 mm and L=12 μm.

electrical contacts. Their extremities are 3 mm wide (W), 300 nm thick and located at a distance of 4μm (G), as illustrated in Figure 5.10. The sensitive volume can be calculated as follow:

$$V = W * H * (2S + G) \tag{5.1}$$

where S is the sensitive contacts length (4μm) and H (1 mm) is the sensitive height for the measurement (evaluated through FEM simulations). The total sensitive volume is equal to 3,6*10^{-11} m^3. The beads are diluted in a PBS solution with 0.5% of SDS to reach a concentration of 0.5 mg/ml for 1μm beads and 4 mg/ml for MNPs of 2 μm. A drop of solution is placed on

the top of the device and after 5 minutes, the beads sedimented between the electrodes are attracted away from the contacts thanks to a permanent magnet. The measurement frequency was set at 1 MHz in order to be in a spectral region not affected by the double layer capacitance. Figure 5.11 shows the measured resistance. When the beads are placed between the

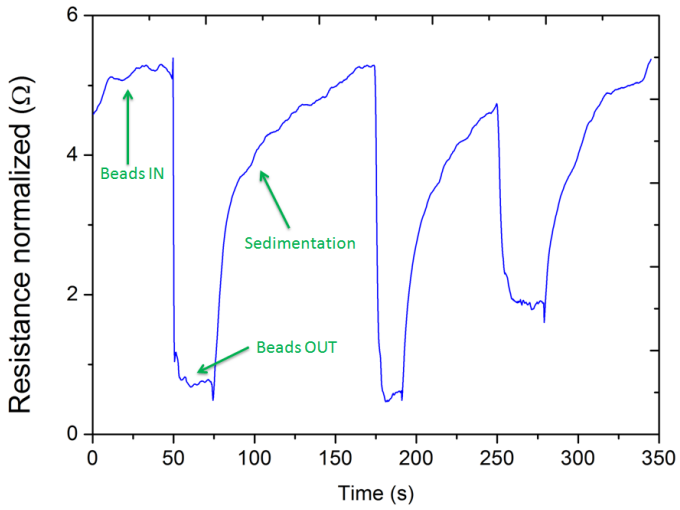

Figure 5.11: Graphic of the resistance variation as function of time when a permanent magnet is used to attract 1 μm particles away from the electrodes. Green arrows indicate respectively when the beads are between the electrical contacts (Beads IN), when they are attracted away by the magnet (Beads OUT) and while they are sedimenting (Sedimentation). A constant descending drift (-30 mΩ/s) in the resistance value is subtracted to the experimental data.

electrodes the resistance is high. Instead, when the magnetic field is applied, attracting away the beads, the resistance drops. Once the magnetic field is removed, the beads sediment and the resistance is restored to the initial value, following an exponential trend. A constant descending drift is observed

in the measurements which is related to the evaporation of the liquid which increases the ions concentration.

The conductance variation ΔG_{TOT}, when beads are attracted away, has been quantified by the experimental data. The average value is $1.67*10^{-4}$ S for 1 μm beads and $3.48*10^{-4}$ S for 2 μm MNPs.

The number of particles in the sensible volume is calculated by the following equation:

$$N = \frac{V * C}{\frac{4}{3}\pi r^3 * \rho} \tag{5.2}$$

where C is the concentration of beads, V the sensible volume, r the radius of MNP and ρ ($\sim$4 g/cm^3) the density of beads. In this way, $N_{1\mu m}$ is $8.57*10^{-4}$ and the same number is found for 2 μm MNPs because a concentration 8 times higher is balanced by a volume of a single particle 8 times larger respect with the 1μm MNPs. Finally, the value of the conductance variation associated to a single bead has been calculated. In fact $\Delta G_{bead} = \Delta G_{TOT}/N$ and it is equal to 19.4 nS for 1μm bead and 40.6 nS for 2 μm particle. A bigger difference between the values of ΔG_{bead} for 1 and 2 μm beads would be expected because the volume of the second is 8 times higher and the variation of G should be of the same order. However, the low mobility of 2 μm nanoparticles in the electric field, together with the creation of big particles clusters could affect the result.

The value of ΔG_{bead} has been compared with the result of FEM simulations. In these simulations, beads are considered perfect insulators. The simulated variation of G for 1μm bead is equal to 25 nS in good agreement with the value calculated from the experiments. Instead the simulated ΔG_{bead} for 2μm particles is 170 nS around 4 times bigger than the experimental value.

5.2.2 Experiments of single bead detection

The fabrication of capacitive sensors is described in section 3.1.4. The chip is patterned with the magnetic zig-zags nanostructures of Py and with a set of coupled electrical contacts employed for the measurements. Different electrodes geometries have been tested. Each chip is provided with 3 magnetic zig-zag conduits and 24 electrodes as illustrated in figure 5.12. One of such contacts is employed as *counter electrode* to set the potential of the solution.

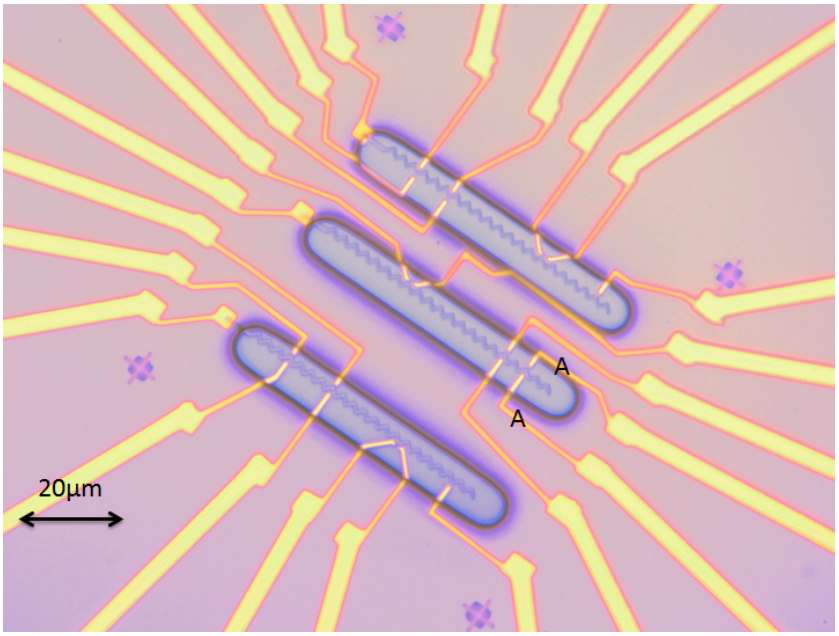

Figure 5.12: Optical microscope image of a capacitive sensor. Each chip is provided with three magnetic zig-zags conduits and 24 electrodes. One of such contacts is employed as counter electrode to set the potential in the solution. The couple of electrodes labelled by "A" represent the geometry used in the numerical simulations.

The magnetic nanostructures and the extremities of the electrical contacts are exposed to the liquid in order to permit the impedantial measurements.

This is achieved by means of 3 openings obtained by optical lithography and Lift-off process. Two different capping layers have been employed: SiO_2 (40-50 nm) or the resist exploited for optical lithography (about 2 μm). The last one is treated with an extra backing process to be hardened and it has the advantage to be thicker compared to Silica, potentially favoring the insulation of the contacts from the liquid (more details in 3.1.4).
FEM (finite element method) simulations on a 3-dimensional model of the device have been performed with COMSOL software to evaluate the theoretical electrical response of the sensor in presence and absence of bead.

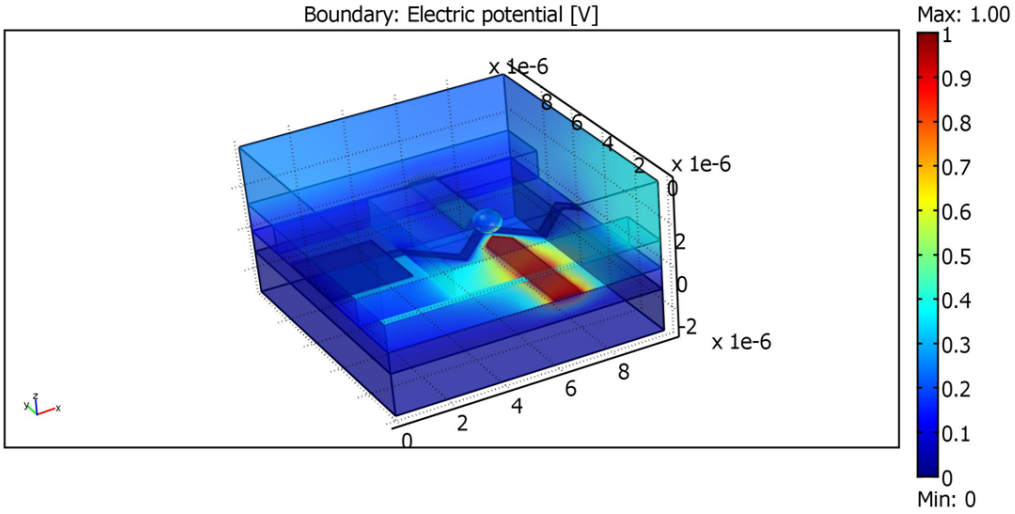

Figure 5.13: Image of the 3D geometry employed in FEM simulation. The colours indicate different value of the electrical potential.

In these simulations, electrical contacts, zig-zags shaped nanostructures and the PBS environment have been considered. An image of the 3D model is shown in figure 5.13. The simulated variation of the resistance in presence and absence of 1 μm bead between the contacts is 32 kΩ as illustrated in figure 5.14 .

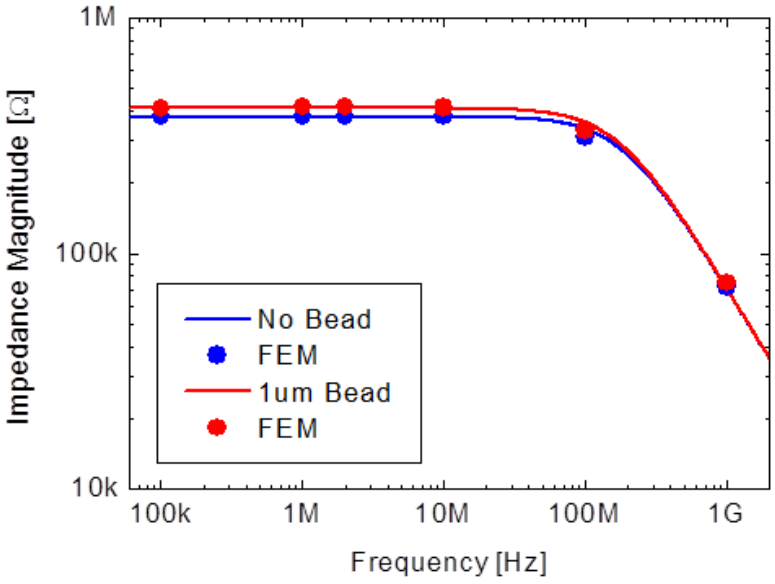

Figure 5.14: Plot from FEM simulations which shows the Resistance variation in presence and absence of bead between the electrodes. In this simulation the double layer capacitance was not considered.

The equivalent circuit for the capacitive sensor is illustrated in figure 5.15(a). C_{DL} is the double layer capacitance (9.8 pF from simulations) created at the interface between electrodes and the PBS solution; it depends on the area exposed to the liquid together with the amount of ions in solution. R_L is the resistance of the liquid. The latter depends on the ions concentration and valence in PBS together with the distance between electrodes. For standard values of PBS solution and considering the electrodes couple labelled by A in figure 5.12, the simulated value is 163 kΩ without beads. The working frequency was calculated to be in a spectral region not affected by the C_{DL} in order to valuate only the variation of R_L. It is achieved for frequencies higher than 105 KHz. C_P represents the effect of parassitic capacitances and it is related to the interfaces between the different materials in the chip. The effect of C_P has to be negligible at the working frequency in

order not to hide the detection signal. The value of C_P extimated by means of an LCR measurement is 120 pF.

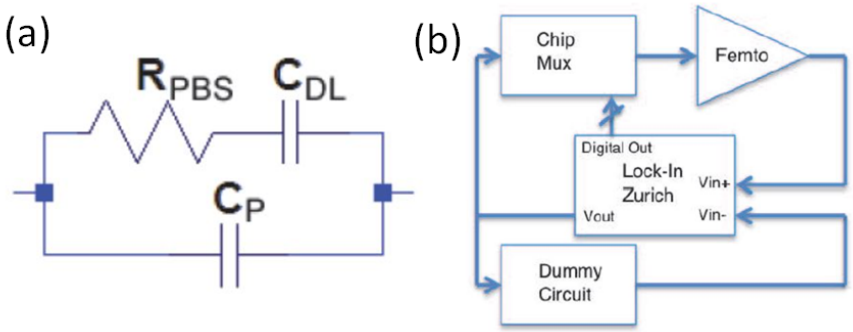

Figure 5.15: Sketches of the equivalent circuit for a capacitive sensor (a) and the electronic readout (b). C_{DL} is the double layer capacitance, R_{PBS} is the liquid resistance and C_P is the parassitic capacitance. In (b) the lock-in amplifier (Zurich), the transimpedance amplifier (Femto), the Dummy circuit and the chip mux are illustrated.

The experiments have been performed in a wet environment of PBS with 0.5% SDS (Sodium Dodecyl Sulfate) to reduce the friction between particles and surface. The external magnetic field is applied by means a four poles electromagnet (the same employed for AMR measurements). The capacitive sensor is mounted on the sample stage described in section 3.3.2. A two probes technique is exploited for the electrical measurement and the device is powered via a lock-in amplifier with an AC signal having an amplitude that ranges between 50 mV and 100 mV and a frequence set at 2 MHz. The output current from the chip is read by means of a trans-impedance amplifier through a virtual ground. The signal is then transferred to the lock-in which demodulate it and, thanks to a really narrow pass-band filter, is able to reduce the electrical noise. However, the effect of the phase noise due to

fluctuations in the input signal phase, coupled with C_P, creates a high noise in the device output which can mask the signal of interest.

In order to reduce the effect of C_P, an active compensation circuit has been introduced. It is a *Dummy circuit* which has the goal to reproduce the transfer function of the device in absence of bead. The signal generated by lock-in is splitted between the the chip and the compensation circuit. The output signals from the device and Dummy circuit are retransferred to the lock-in that subtractes them and cleans the signal of interest from all the effects related to parassitisms. The schematic view of the whole electronic setup is illustrated in figure 5.15(b).

The MNPs are monitored by means of an optical microscope trough a 60x immersion objective. The particles (myOne^{TM}, Invitrogen) have been successfully displaced between the electrical contacts applying a continuous magnetic field of 250 Oe which is rotated in a clockwise or anti-clockwise direction. In this way an alternate sequence of HH and TT DWs nucleated at the zigs-zags corners is simultaneously displaced along the structure dragging the particles on the top of DWs. Figure 5.16 illustrates the crossing of a bead between two electrical contacts in a capacitive sensor.

However, the experiments don't show an appreciable variation of the elec-

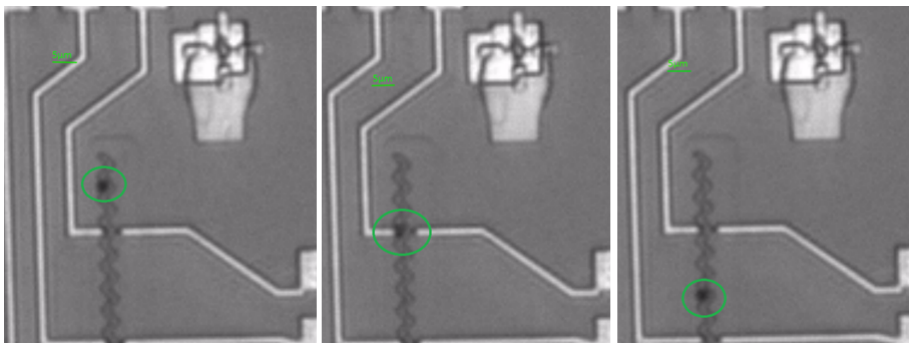

Figure 5.16: Sequence of the transit of a 1μm bead between two electrical contacts in a capacitive sensor.

trical signal when the bead is located between the electrodes. This can be related to several reasons that are actually under investigation. Firstly, the capping layer employed on the chip doesn't allow a perfect insulation of the device. If the liquid penetrates and goes in contact with the electrodes, the electrical measurements is expected to be be strongly altered by a big parassitic double layer capacitance. A second reason can be the position of the bead along the z-axis. If the bead fluctuated over the magnetic conduit above 100 nm, the electrodes (which are 65 nm thick) would not be able to efficiently detect the impedential variation due to the MNP because the electric field lines would not intercept it. Moreover, the electrical noise associated to this measurement is still not completely negligible and further work has to be done to understand its origin and to delete it. Finally, a high signal drift during the measurements is observed. It is probably due to variations in temperature or ions concentration and it could negatively affect the electrical detection.

5.3 Conclusions and perspectives

In this chapter two different sensors to detect beads have been developed and illustrated. The AMR sensors permit to achieve a precise recording of MNPs that transit over magnetic zig-zags conduits. Instead, capacitive sensors have to be further developed and improved.

The results display how the magnetic detection is much less sensitive to perturbations than capacitive measurements. The main reason is that most of the media (such as PBS or biological medium) are not magnetic (except for a negligible diamagnetism or paramagnetism), while they present an electric behavior which can disrupt the impedantial measurement.

The NaBiS group had previously demonstrated how nanometric Py corners and micrometric rings can be employed to trap and detect magnetic nanopar-

ticles through an AMR measurement [62],[41]. However, the AMR sensors fabricated and developed in this thesis work are completely innovative devices. They exploit the same magnetic conduit both for manipluation and detection, adding a new important functionality to DWTs: the integrated feedback on the manipulation, because particles can be detected while moving. In this way, we are going towards a close-loop system that clearly offers, a large amount of advantages.

Besides, the measurements have been carried out on 1 μm beads, but the SNR ratio suggests us that smaller particles can be employed. By fixing the problem of the "oscillating noise" on the base-line, a particle with 250 nm diameter or lower could be detected, considering that the calculated depinning field variation is 14-15 Oe for 1 μm bead. At the current state of the art, there is not a compact and integrated device capable to such a detection of a bead crossing thorough a constriction.

For example, Magnetic Tunnel Junction sensors (MTJs) [63] could be used to detect beads with the same (or even larger) sensitivity but their complexity is much higher compared to AMR sensors and they could not be easily integrated with a system for beads manipulation.

The future perspective for AMR measurements and setup are related with the simplification of the electronic readout system by projecting an integrated lock-in which will be also able to remove the electrical noise due to a spurious effect of the lock-in currently in use. Moreover, the sensors can be equipped by a more complex microfluidic cell to better control the flux of fluid over the chip.

Chapter 6

Controlled administration of nanoparticles to a single cell

This final chapter describes one of the most important results of this thesis work which concerns the controlled administration of magnetic nanoparticles to a target cell. The DWTs technology is employed to finely manipulate MNPs on a chip where living cells are cultured. In this way, a single particle can be displaced in close proximity to the cell membrane. This tool permits to study the interaction between a single bead with a single cell and to evaluate in which conditions the up-take of particles occur, which is a fundamental topic in the drug-delivery process (see chapter 1).

In the first part of the chapter the optimization of MNPs manipulation in the cellular medium, together with the preparation of the chip to achieve a good cellular adhesion and viability is described. In the second part, the "passive" up-take of MNPs is demonstrated. Finally, the results related to the controlled administration of nanoparticles to a target cell are described.

6.1 Manipulation of MNPs in the cellular medium

Magnetic martrix of Py rings can be employed to trap and drag magnetic nanoparticles all over a 2D space as discussed in chapter 4. Similar devices are used to perform the experiments in presence of biological entities. The first test has been made to study the efficiency of beads manipulation in the cellular medium.

The magnetic nanoparticles used for all the experiments (nanomag-CLD-redF, Micromod) have a diameter of 300 nm, they are functionalized with carbossylic acid ($COOH^-$) and they are red-fluorescent, exploiting a TRITC marker. The functionalization with $COOH^-$, that creates a positive Zeta-potential, is chosen to favor the electrostatic interaction with the cellular membrane which presents a negative Zeta-Potential as illustrated in chapter 1. The Py nanostructures are patterned over a Si/SiO_2 wafer by EBL (see section 3.1.4). Magnetic Rings are 300 nm wide with a diameter of 5-10μm and they are packaged in a square or hexagonal matrix (see Fig. 4.3). Three different capping layers have been tested in order to achieve two goals: preventing the chip from damages due to the liquid and favoring the cellular adhesion on the surface. The first one is a 50 nm SiO_2 coating, properly treated with an oxigen of plasma in a plasma asher machine to make the surface hydrophillic (see section 3.1.3). The second one is a double layer of Al_2O_3 (25 nm) and SiO_2 (25 nm) also treated with an Oxigen of plasma. The last one is a composed layer made of 10 nm of Al_2O_3 and 60 nm of nanostructured Zirconia ZrO_X (deposited through supersonic cluster beam deposition technique [64] at "Fondazione Filarete", in Milan). Nanostructured ZrO_X is a porous material which favor the cellular adhesion on the surface. The roughness of nanostructured Zirconia layer was evaluated by means of an AFM scan and it ranges between 10-20 nm (RMS) in 1 μm^2, for different samples (see Fig. 6.1).

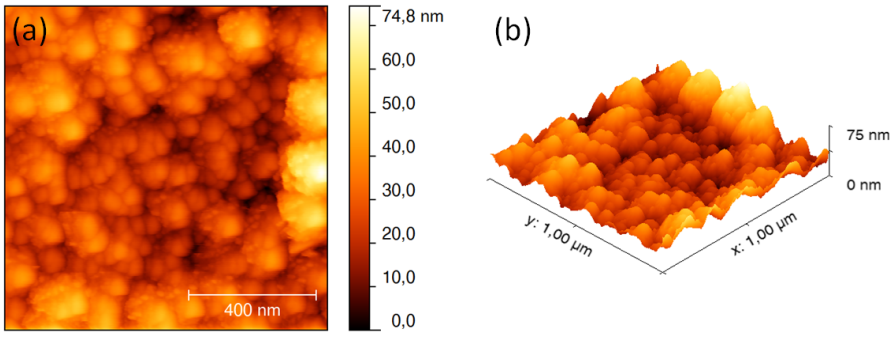

Figure 6.1: AFM image (a) and derived 3D view (b) of a sample covered by ZrO_X.

The manipulation experiments have been performed in the cell culture medium DMEM. It is a basal medium consisting of Amino Acids, Glucose, pH indicator, Salts and Vitamins. DMEM was enriched by antibiotics to increase the cellular viability and a serum that provides the nutrients for the cells.

The employed MNPs have a diameter (300 nm) which is smaller compared to the beads used in the rest of the work. The attracting magnetic force due to the stray field generated by DWs depends on the volume of the super-paramagnetic body (see eq 2.29), therefore 300 nm particles suffered a force around 27 times lower than 1μm beads. Moreover, DMEM presents a higher viscosity than PBS or water and this negatively affects the manipulation. In order to overcome these problems, a set of micromagnetic simulations have been performed to optimize the thickness of magnetic rings so that the trapping force is maximized. The next section describes the results of such simulations.

6.1.1 Micromagnetic simulations

The force generated by a single magnetic DW in a Py Ring on a 300 nm superparamagnetic bead has been simulated as function of the conduit thickness and the distance between MNP and nanostructures. By means of OOMMF simulations, the stray field generated by a DW in a Py ring with a diameter of 5 μm and width of 300 nm was calculated. Firstly, upon the application of a saturating in-plane field of 500 Oe, the magnetic configuration of a single ring has been found.

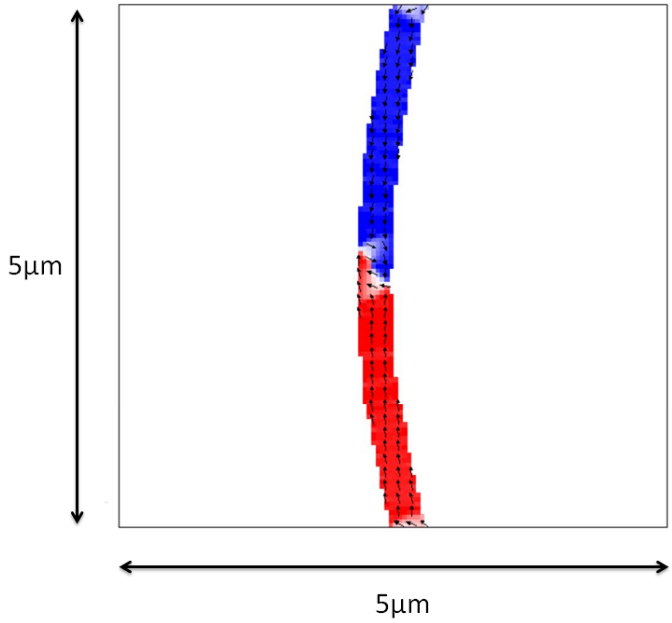

Figure 6.2: Magnetization of a portion of ring from OOMMF. The arrows show the direction of the magnetization in the xy-plane. Blue and red pixels indicate positive and negative values of the magnetization along y. HH vortex DW is nucleated by an external in-plane field (500 Oe).

A vortex configuration of magnetization in the DW is observed for all the different values of thickness simulated. It is due to the balance between the shape anisotropy of the structures and the magnetostatic energy contribution.

The figure 6.2 displays the magnetization inside the ring upon the application of a strong saturating magnetic field in the x direction. The tendency to close the field lines of the magnetization on the upper and lower part of the arch of the ring is an artifact due to the finite area of the simulation which did not consider the entire ring in order to save computation time. Starting from the magnetic configuration, the stray field generated by the DW was simulated by OOMMF. From that, the attracting force is calculated via Matlab, according to the following equation:

$$F = -\mu_0 \chi \int_V \nabla(\mathbf{H}_{dw} \cdot \mathbf{H}_{dw}) dV \tag{6.1}$$

where H_{dw} is the stray field generated by the DW and the integration is over the superparamagnetic bead volume. The 300 nm MNPs considered in this simulation have a magnetic susceptibility χ of 0.39.

The force along the z-axis was calculated for different values of ring thickness (30-80 nm) and considering a distance from the top of the ring and the bottom of the bead which ranges between 50 nm and 600 nm. The lower limit was fixed at 50 nm because it is the minimum distance if a capping layer of 50 nm is placed on the top of magnetic structures.

The results illustrated in figure 6.3 show that a maximum value of the force along z is obtained for a thickness of 60 nm, independently on the distance between bead and surface. For example, considering a distance of 50 nm, the force for a 60 nm thick structure (45.4 pN) is more than three times higher compared with the force exerted by a 30 nm thick ring (12.8 pN). For a thickness larger than 60 nm the force suffered by particles decreases. It is probably due to the rotation of magnetization also in a direction perpendicular to the xy-plane when the DW is nucleated in thicker structures. In this situation, the DW is not more a "pure" Neel wall (with the magnetization rotating only in the xy plane) and a lower stray field is generated.

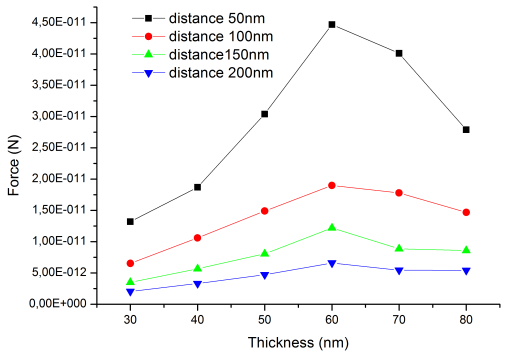

Figure 6.3: Magnetic force on a superparamagnetic bead having a diameter of 300 nm and χ equal to 0.39, as a function of the ring thickness. The distance between the top of the magnetic structure and the bottom of the bead ranges between 50 nm and 200 nm.

Figure 6.4 shows the force (z-component) trend when the distance between bead and surface ranges between 50 and 600 nm.

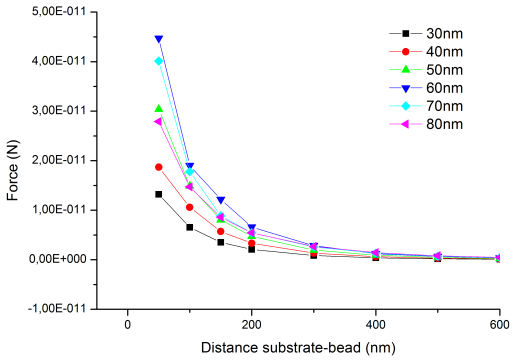

Figure 6.4: Magnetic force on a superparamagnetic bead having a diameter of 300 nm and χ equal to 0.39, as a function of the distance between the top of the Py ring and the bottom side of bead. It was calculated for different values of the ring thickness ranging between 30-80 nm.

An exponential decay is observed independently by the ring thickness.
To summarize, with these simulations two conclusions can be drawn: firstly the force suffered by 300 nm particles is maximized when the thickness of magnetic rings is 60 nm. Secondly, an efficient manipulation is possible only if beads are in close proximity to the surface, because the force exponentially decrease with the distance.

6.1.2 Manipulation experiments

In this paragraph, the manipulation experiments of 300 nm nanoparticles in DMEM medium will be described. The setup employed is presented in section 3.3.1. The temperature, set at 37 ^{o}C, is controlled by means of a thermostat connected to a thermocouple placed in contact with the medium. A small heating plate, mounted just under the sample stage, is employed to heat the sample and the medium. The stepper motors system is used to apply the rotating magnetic field in-plane. 300 nm beads (nanomag-CLD-redF, Micromod) are diluted in DMEM to reach a concentration of 0.5 μg/ml. An optical microscope with a 60x immersion objective has been used to monitor the beads displacement.
The idea behind this experiment is to understand the effect of the cellular medium on the manipulation over a period of 6 hours (which is the typical duration of a biological experiment) in which the sample remains in contact with the DMEM.
Three different devices have been tested, each one patterned with a matrix of 30 nm thick rings, with a diameter of 10 μm. Even if the force is not maximized with a nanostructures thickness of 30 nm, it has been initially preferred to have a flatter surface. The first chip is covered by Al_2O_3 (10 nm) and nanostructured ZrO_X (60 nm). The second one is capped by SiO_2 (50 nm) and the third device is coated by a composed layer of Al_2O_3 (25 nm) and SiO_2 (25 nm).

In the first 3.5 hours, despite the viscosity of the medium, it is possible to achieve such a kind of fine manipulation, for all the devices, even with a corrugated surface like nanostructured ZrO_X films. The rotating magnetic field generated by the permanent magnets controlled through the stepper motors, allows to finely displace the MNPs on a single ring as illustrated in the panels of figure 6.5 which are frames of a video taken under the optical microscope.

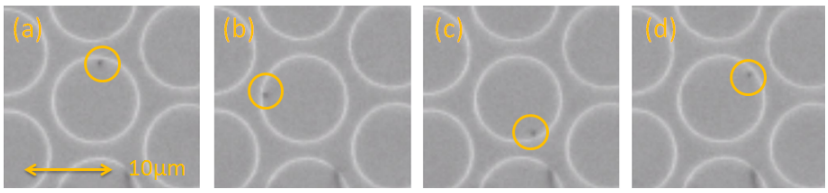

Figure 6.5: Manipulation sequence of a single 300 nm bead around a magnetic ring in an hexagonal matrix by applying a 300 Oe in-plane field. A sample covered by ZrO_X (50 nm) was employed. The magnetic field is rotated in an anti-clockwise direction. The images are recoded from an optical microscope exploiting a 60x immersion objective.

Regarding the effect of time and medium over the manipualation, for the first and the second device (terminated respectively with 60 nm of ZrO_X and 50 nm of SiO_2), between 3.5 and 5 hours the manipulation becomes less efficient; some particles appear to be only sightly bounded to DWs and they begin to fluctuate over the magnetic conduits. After 5 hours, it is not more possible to attract and displace the particles over the nanostructures.
Instead, over the chip coated with Al_2O_3 (25 nm) and SiO_2 (25 nm), an efficient manipulation of beads is possible for the first 5 hours. After 5.5 h the manipulation becomes ineffective also for this device. The reasons for the manipulation becoming less efficient after a certain time are essentially related to an ineffective insulation of the magnetic nanostructures from the

liquid. In fact, the employed capping layers do not prevent the magnetic rings from going in contact with DMEM. This produces the oxidation of Py which significantly alter the magnetic properties of the conduits whose thickness is only 30 nm.

The results show that a comparable impermeability is observed for the first chip (coated with 10 nm of Al_2O_3 and 60 nm of ZrO_X) and the second device (capped by 50 nm of SiO_2), despite the different material layers employed to coat them. Moreover, it can be observed that Al_2O_3 guarantees a better insulation from the liquid compared to SiO_2 but it is still not enough to prevent nanostructures from damages due to the liquid for a long time (6 h). In order to completely overcome the problem, we are actually developing a process to deposit Silicon Nitride (SiN) as capping layer which offers better insulating properties and impermeability to saline solutions.

6.2 Passive uptake of magnetic nanoparticles

Before performing "active" uptake experiments, one as to demonstrate that the employed magnetic nanoparticles can be internalized by cells. Tests of cellular uptake have been performed at the IFOM center where the confocal microscope *TCS-SP5 Leica* was used; its high resolution allows to visualize the relative position of particle and cell also in z-direction, so that the internalization of beads can be properly observed. Epithelial human cells from the HeLa line are employed to this purpouse. The cellular nucleus is stained with the green-fluorescent marker H2B-GFP which is a basic nuclear protein responsible for the nucleosome structure of chromatin. Cells have been incubated at 37^oC in an atmosphere of 5% CO_2, with magnetic and red-fluorescent nanoparticles (nanomag-CLD-redF, Micromod) diluted to $10\mu g/ml$.

After 4 hours, few ml of cells have been washed in PBS to remove the particles

dispersed in the medium; then, the cells have been placed on a microscope slide and investigated under the confocal microscope.

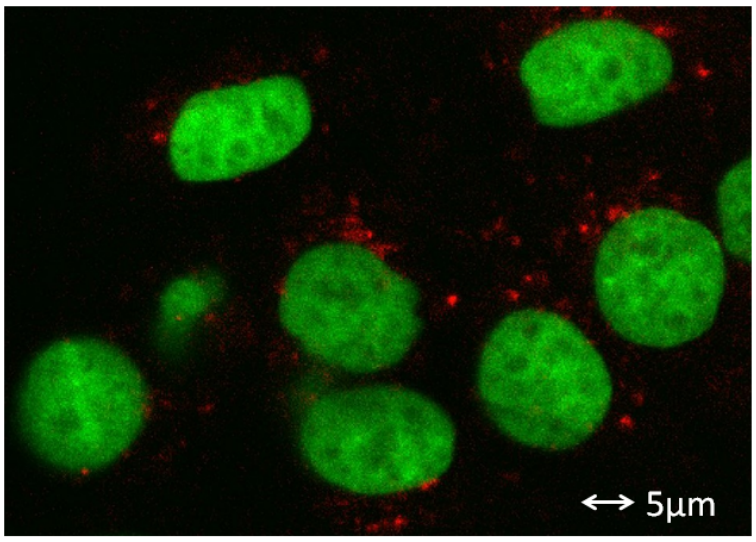

Figure 6.6: Confocal microscopy image: the green-stained cellular nucleus of an HeLa cell is surrounded by red fluorescent (TRITC) magnetic nanoparticles. It is acquired by a *TCS-SP5 Leica* microscope.

Figure 6.6 shows the green-fluorescent cell nucleus which is crowned by red-fluorescent magnetic nanoparticles. However, in this experimental condition it is not possible to unambiguously demonstrate the complete particle internalization; since it is not possible to properly see the cellular membrane, it is difficult to evaluate if the particles are inside the cytoplasm or they are bounded outside the cytoplasmic membrane.
In order to understand where nanoparticles are exactly located, cytoplasm has been labelled with a Dextran-based green fluorescent marker. Dextran is a polysaccharide made of many glucose molecules, which is quickly absorbed by cells. The cellular solution was enriched with this marker and, after 30 minutes, it has been washed in PBS and placed on a microscope slide. In

this way, the entire cell appears green and red magnetic nanoparticles are observed inside the cytoplasm as illustrated in figure 6.7.

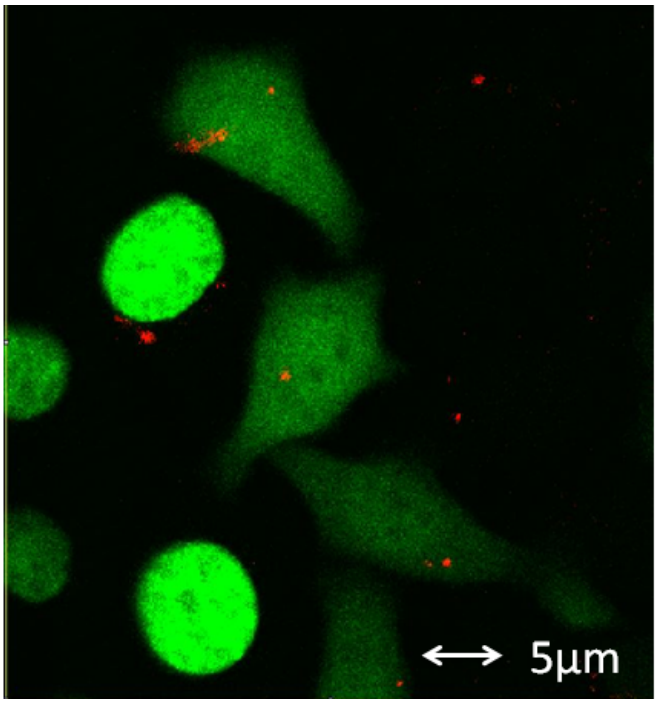

Figure 6.7: Confocal microscopy image: red-fluorescent (TRITC) magnetic nanoparticles are internalized inside the cells (HeLa). The green cytoplasm is labelled by a Dextran based marker. The brightest green circular spot on the left are two cellular nuclei (some cells have not absorbed the marker). Image acquisition via a *TCS-SP5 Leica* microscope.

In this way, the uptake of 300 nm particles functionalized with COOH has been demonstrated.

6.3 Manipulation of nanoparticles to a target cell

One of the goals of this thesis work is to manipulate nanoparticles to administrate a drug to a target cell. In this paragraph, it will be demonstrated how magnetic nanoparticles can be finely moved in close proximity to a specific cell where they interact with the cellular membrane. Two different cell types have been employed for these experiments: rat's mammalian cancer cells supplied by "Istituto Farmacologico Mario Negri" and epithelial human cells from HeLa line, provided by the "IFOM center". The samples used are the same described in section 6.1: Py rings (300 nm wide, 30 nm thick and with a diameter of 10μm) arranged in a hexagonal or square matrix and capped with SiO_2 (50 nm). The external in-plane field exploited to manipulate beads is applied by means of the stepper motors system, described in section 3.3.1 together with the entire setup used for the biological experiments. Two main tests will be described in this paragraph. In the first one, 800 μl of mammalian cells diluted in the cellular medium MEM are cultured for 2 hours on the top of the chip which is placed in the sample stage where the temperature is set at 37^{o}C by means of a PID thermostat connected to a thermo-couple and to a heating plate mounted just under the sample stage (more details in section 3.3.2). In order to compensate the evaporation of the medium, 100 μl of DMEM are added every half an hour. After 2h, magnetic nanoparticles with a diameter of 300 nm (nanomag-CLD-redF, Micromod) and functionalized by COOH are added to the cell environment, after being properly diluted to reach a concentration of 1 μg/ml.

The system is monitored by means of an optical microscope with a 60x immersion objective. The beads, trapped on the DWs generated by an in-plane field of 300 Oe, are successfully manipulated on a single ring by rotating the magnetic field (see section 4.2); a single bead can be driven in contact with

the membrane of a target cell, as illustrated in figure 6.8.

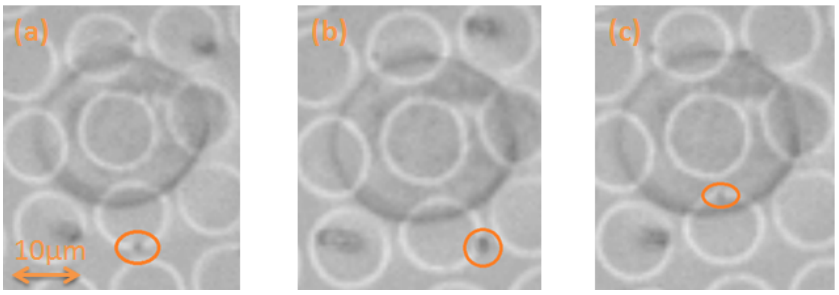

Figure 6.8: Manipulation sequence of a 300 nm MNP to a target cell (mammalian-cancer cell). A continuous magnetic field of 300 Oe is rotated in a clockwise direction to displace the bead. An immersion 60x objective is used.

Once the bead is in contact with the cell, the magnetic field can be even removed because, also in absence of the attracting force generated by the DW, nanoparticles are attracted to cells by electrostatic interactions (due to the opposite values of the Zeta-potential). A detailed study of the effect of the magnetic force applied to the bead on the uptake has not been fully accomplished during this thesis work. Generally speaking, the magnetic force exercised by the DW could unfavor the internalization mechanisms since it attracts the beads on the chip surface outside the cell.
In some cases, it has been possible also to manipulate the particles under the cell membrane, in contact with the surface. This means that the cellular adhesion on the chip is not optimal. Besides, exploiting a normal optical microscope, it is difficult to evaluate the height of the particle relative to the cell and the chip surface; consequently the internalization process is not easily detected.
In these experimental conditions, without a CO_2 incubator and in DMEM medium, after some hours (4-5 h) from the cells culturing, the viability of cells decrease and they begin to show signs of apoptosis. This can be due

to two main factors: firstly the cells employed are not suitable to live in the CO_2 deficent environment like that imposed by the experimental setup (the CO_2 amount inside the body of a living mammal is around 5%) and secondly the SiO_2 surface preparation on the chip could not guarantee an adequate sterilization.

In order to solve these problems, a second experiment has been executed at the IFOM center. In this test, epithelial cells from HeLa line are used. They can be cultured on various surfaces maintaining a high viability. Moreover, a confocal microscope (TCS-SP5 Leica) which offers a high spatial resolution along z-direction, has been used. The same setup described in the previous experiment is employed for manipulation, except for the microscope. In order to obtain a good cellular adhesion on the chip, the cells are cultured for 5 h. During this time, the chip is incubated at 37^oC in an atmosphere with 5% of CO_2. Then, it is placed on the sample stage where beads are added to reach a concentration of $1\mu g/ml$ in a DMEM medium.

In this experimental condition the cell viability is optimal also after 4-5 hours, and we indeed observed an excellent cellular adhesion on the surface. However, the long incubation compromises the manipulation efficiency of the nanoparticles, due to the aforementioned problem of magnetic structure degradation due to medium penetration in the capping layer. Nevertheless, in the first hour after the incubation it was still possible to work. So, it has been possible to trap and manipulated MNPs on a single Py ring applying a rotating magnetic field of 300 Oe. Therefore, beads are dragged in contact with the cellular membrane as illustrated in figure 6.9.

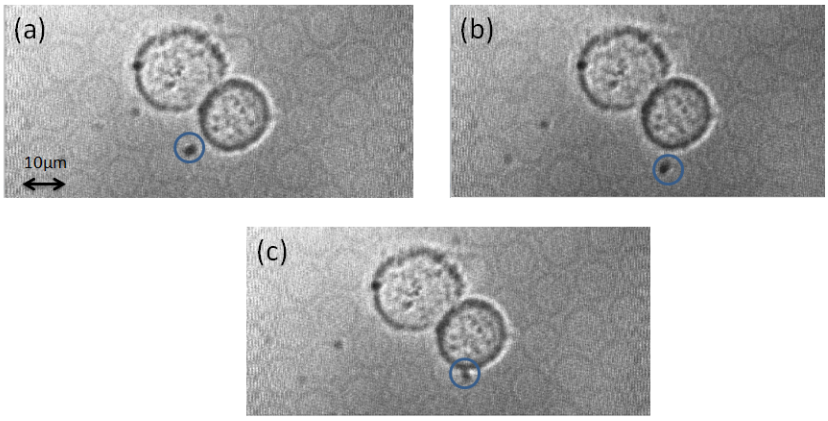

Figure 6.9: Frames from a video showing the manipulation of a 300 nm bead dragged to a target cell (epithelial HeLa cell) through a rotating magnetic field of 300 Oe. Image acquisition via a *TCS-SP5 Leica* microscope.

Once the MNP is placed in contact with the cell, the particle is attracted to the cellular membrane by the electrostatic interaction due to the opposite value of the Zeta-potential and the magnetic field can be removed.

6.4 Conclusions and perspectives

In this chapter, it is described how the DWTs technology can be exploited to achieve a controlled administration of MNPs to a target cell, manipulating the beads in close proximity to the cellular membrane. The next step, currently under development, is to demonstrate the internalization of MNPs loaded with specific drug and to investigate the final details of uptake using our magnetic tweezers. This technology can be potentially used for a large amount of biological and medical applications as described in chapter 1.

Conclusions and Perspectives

In this thesis work, it has been developed the building blocks of a microfluidic on-chip platform for controlled drug-delivery to a single cell through magnetic nanoparticles. Three main results have been obtained. The first one concerns the implementation of the DWTs domain wall tweezers technology to achieve a synchronized manipulation of a magnetic nanoparticles batch in a 2-dimensional space over a matrix of magnetic rings.

The second one is the development of on-chip sensors for the detection of beads transit over magnetic conduits in lab on chip for controlled drug delivery. Two different sensors have been employed: the AMR and capacitive detectors.Concerning the first ones, the effective and successful detection of beads in manipulation experiments has been demonstrated, while the capacitive sensors need to be further developed, since only the preliminary results have been presented.

Finally, the controlled administration of magnetic nanoparticles to a target cell has been demonstrated. The particles are efficiently manipulated in the cellular medium and they are moved in contact with cell membrane.

The future perspectives are related, first of all, with the fine optimization of devices and measurement setup already developed in this thesis work. For the DWTs technology, a complete automation could permit to draw a random path on a PC which controls and actuates a sequence of magnetic field to displace the magnetic nanoparticles along the chosen direction.

For AMR sensors, the perspectives are related with the integration of the

electronic readout system by projecting an integrated lock-in with better performances in terms of noise rejection respect the instruments currently in use. Moreover, the sensors can be equipped by a more sophisticated microfluidic cell to better control the fluxes over the chip.

Both the sensors and the chip with the magnetic nanostructured used to achieve the controlled administration of magnetic nanoparticles to a target cell need further works in order to optimize their impermeability to the biological medium, also after a long exposure time to it. Moreover, it has to be unequivocally demonstrated how nanoparticles carrying drugs, controlled by means of the DWTs technology, can be efficiently internalized by cells.

The final perspective is the integration of the sensors and the devices for 2D manipulation in a single on-chip platform. Such system would be able to count and transport magnetic nanoparticles in a microfluidic channel in order to displace a controlled amount of functionalized particle, to the target cells (through the 2D manipulation devices). The schematic principle of such platform is illustrated in figure 6.10.

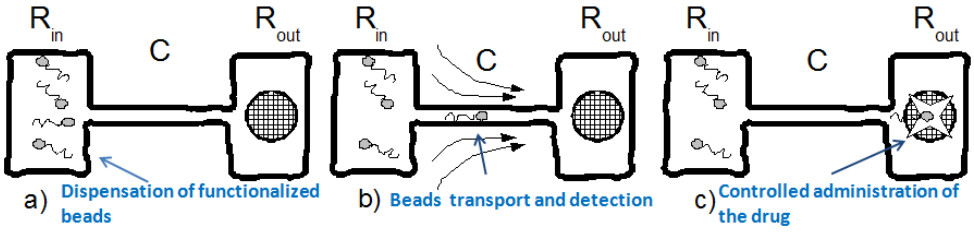

Figure 6.10: Scheme of the platform made of two reservoirs (R_{IN} and R_{OUT}) connected by a channel (C). Functionalized MNPs are dispensed in the reservoir R_{IN} (a). From there, beads are manipulated along the channel (C) and detected by means of an AMR (or capacitive) device (b). At the end of the channel, a second reservoir (R_{OUT} where cells are cultured is located. Beads are manipulated by means of the DWTs to the target cell to administrate the drug.

This platform could be employed for a large number of biological and medical assays, such as testing the effectiveness of a certain drug on a target cell or studying the bio-chemical mechanisms that occcur when a cell interact with other biological entities.

Bibliography

[1] Ruth Nussinov, and Carlos Aleman, *Nanobiology: from physics and engineering to biology*, Physical biology, (2006); 3

[2] Freitas Jr RA, *What is nanomedicine?*, Nanomedicine: Nanotechnology, Biology and Medicine. 2005, pag. 2-9

[3] LaVan DA, McGuire T, Langer R. *Small-scale systems for in vivo drug delivery*, Nat Biotech. 2003; 21(10), pag. 1184-1191.

[4] Adriano Cavalcanti and Bijan Shirinzadeh and Robert A Freitas Jr and,Tad Hogg. *Nanorobot architecture for medical target identification*, Nanotechnology. 2008; 19(1): 015103.

[5] Muller RH, Mader K, Gohla S. *Solid lipid nanoparticles (SLN) for controlled drug delivery - a review of the state of the art*, Eur J Pharm Biopharm. 2000;50(1) pag.161-177.

[6] M. Pernia Leal, A. Torti, A. Riedinger, R. La Fleur, R. Cingolani, R. Bertacco and T. Pellegrino, *Controlled release of Doxorubicin loaded within magnetic thermo-responsive nanocarriers under magnetic and thermal actuation in a microfluidic channel*, ACS Nano (2012), 6; (12):10535

[7] R.M. Sawant, J.P. Hurley, S. Salmaso, A. Kale, E. Tolcheva, T.S. Levchenko, and V.P. Torchilin, *"smart" drug delivery stems: double*

targeted pH responsive pharmaceutical nanocarriers, Bioconjug Chem. (2006); 17(4): 943-949.

[8] Petros RA, DeSimone JM. *Strategies in the design of nanoparticles for therapeutic applications*, Nat Rev Drug Discov. 2010; 9(8) pag.615-627

[9] Gao X, Cui Y, Levenson RM, Chung LWK, Nie S.*In vivo cancer targeting and imaging with semiconductor quantum dots*, Nat Biotech. 2004;22(8) pag.969-976.

[10] Salvati, E. (2013) *Multi-functionalized nanoparticles for therapy and diagnosis of alzheimer's disease.*, PhD thesis

[11] Kim C, Pisano AP, Muller RS.*Silicon-processed overhanging microgripper* Microelectromechanical Systems, Journal of. 1992;1(1) pag.31-36.

[12] Claes Thelander and LS. *AFM manipulation of carbon nanotubes: Realization of ultra-fine nanoelectrodes* Nanotechnology. 2002;13(1) pag.108

[13] Wheeler AR, Throndset WR, Whelan RJ, et al. *Microfluidic device for single-cell analysis*, Anal Chem. 2003; 75(14) pag.3581-3586

[14] Fu AY, Chou HP, Spence C, Arnold FH, Quake SR. *An integrated microfabricated cell sorter*, Anal Chem. 2002;74(11) pag.2451-2457

[15] Ashkin A. *Acceleration and trapping of particles by radiation pressure*, Phys Rev Lett. 1970;24(4)pag.156-159

[16] SC Kuo, MP Sheetz *Force of single kinesin molecules measured with optical tweezers*, Science. 260; 5105 pag. 232-234

[17] Ashkin A. *Forces of a single-beam gradient laser trap on a dielectric sphere in the ray optics regime*, Methods in cell biology. Vol Volume 55. Academic Press; 1998 pag.1-27

[18] Pohl H.A. *Some effects of nonuniform fields on dielectrics* J Appl Phys. 1958;29(8) pag.1182-1188

[19] Q. A. Pankhurst and J. Connolly and S. K. Jones and,J.Dobson. *Applications of magnetic nanoparticles in biomedicine*, J Phys D. 2003;36(13): R167

[20] Yu Zhang, Mo Yang, Nathaniel G. Portney, Daxiang Cui, Gurer Budak, Ekmel Ozbay, Mihrimah Ozkan, Cengiz S. Ozkan, *Zeta potential: a surface electrical characteristic to probe the interaction of nanoparticles with normal and cancer human breast epithelial cells*, Biomed Microdevices (2008) 10: 321-328

[21] Riccardo Di Corato, Nadja C. Bigall, Andrea Ragusa, Dirk Dorfs, Alessandro Genovese, Roberto Marotta, Liberato Manna, and Teresa Pellegrino, *Multifunctional Nanobeads Based on Quantum Dots and Magnetic Nanoparticles: Synthesis and Cancer Cell Targeting and Sorting* ACS Nano (2011) 5(2) pag.1109-1121

[22] Tore-Geir Iversena, Tore Skotlanda, Kirsten Sandvig, *Endocytosis and intracellular transport of nanoparticles: Present knowledge and need for future studies* , Nano Today (2011) 6, pag.176-185

[23] Tiantian Wang, Jing Bai, Xiue Jiang, and G. Ulrich Nienhaus, *Cellular Uptake of Nanoparticles by Membrane Penetration: A Study Combining Confocal Microscopy with FTIR Spectroelectrochemistry*, ACS Nano (2012) 6(2) pag.1251-1259

[24] Khin Yin Wina, Si-Shen Feng, *Effects of particle size and surface coating on cellular uptake of polymeric nanoparticles for oral delivery of anticancer drugs*, Biomaterials 26 (2005) pag.2713-2722

[25] *Endosomes and endocytosis*, from http:// micro.magnet.fsu.edu/

[26] Weigl BH, Bardell RL, Cabrera CR, *Lab-on-a-chip for drug development*, Adv Drug Deliv Rev. (2003); 55(3):349-377

[27] Dittrich PS, Tachikawa K, Manz A, *Micro total analysis systems. Latest advancements and trends*, Anal Chem. (2006); 78(12):3887

[28] Tucker T, Marra M, Friedman JM, *Massively parallel sequencing: The next big thing in genetic medicine*, The American Journal of Human Genetics, (2009); 85(2): 142-154

[29] *Gene-quantification* from http://www.gene-quantification.de/lab-on-chip.html

[30] Sanders GHW, Manz A. *Chip-based microsystems for genomic and proteomic analysis*, TrAC Trends in Analytical Chemistry. (2000); 19(6): 364-378

[31] Terry SC, Jerman JH, Angell JB. *A gas chromatographic air analyzer fabricated on a silicon wafer*, Electron Devices, IEEE Transactions on. 1979;26(12):1880-1886

[32] Gijs MAM, *Magnetic bead handling on-chip: New opportunities for analytical applications*, Microfluidics and Nanofluidics. 2004;1(1):22-40

[33] Gunnarsson K, Roy PE, Felton S, et al. *Programmable motion and separation of single magnetic particles on patterned magnetic surfaces*, Adv Mater. (2005); 17(14): 1730-1734

[34] Vieira G, Henighan T, Chen A, et al. *Magnetic wire traps and programmable manipulation of biological cells*, Phys Rev Lett, (2009); 103(12): 128101

[35] Donolato M, Vavassori P, Gobbi M, et al. *On-chip manipulation of protein-coated magnetic beads via domain-wall conduits* Adv Mater, (2010); 22(24): 2706

[36] Neuman KC, Nagy A. *Single-molecule force spectroscopy: Optical tweezers, magnetic tweezers and atomic force microscopy*, Nat Meth, (2008); 5(6): 491-505

[37] P. P. Freitas, R. Ferreira, S. Cardoso, and F. Cardoso. *Magnetoresistive sensors*, Journal of Physics: Condensed Matter, (2007) 19:165221-42

[38] M. Donolato, E. Sogne, B. T. Dalslet, M. Cantoni, D. Petti, J. Cao, F. Cardoso, S. Cardoso, P. P. Freitas, M. F. Hansen, and R. Bertacco *On-chip measurement of the Brownian relaxation frequency of magnetic beads using magnetic tunneling junctions* Appl. Phys. Lett. 98, 073702 (2011).

[39] L. Ejsing, M. F. Hansen, a. K. Menon, H. a. Ferreira, D. L. Graham, and P. P. Freitas. *Planar Hall effect sensor for magnetic micro- and nanobead detection*, Applied Physics Letters, (2004) 84(23):4729

[40] S Yuasa and D D Djayaprawira. *Giant tunnel magnetoresistance in magnetic tunnel junctions with a crystalline MgO(001) barrier*, Journal of Physics D: Applied Physics, (2007), 40(21): R337-R354,

[41] P. Vavassori,V. Metlushko,B. Ilic, M. Gobbi, M. Donolato, M. Cantoni, and R. Bertacco *Domain wall displacement in Py square ring for single nanometric magnetic bead detection*, APL, (2008)

[42] Weiss P. *La variation du ferromagnetisme du temperature.* Comptes Rendus. 1906; 143:1136.

[43] Landau L, Lifshitz E.*On the theory of the dispersion of magnetic permeability in ferromagnetic bodies.* Physik Z. 1935; 8:153.

[44] Blundell S. *Magnetism in condensed matter.* Oxford University Press; 2001

[45] McMichael RD, Donahue MJ.*Head to head domain wall structures in thin magnetic strips.* Magnetics, IEEE Transactions on. 1997;33(5):4167-4169.

[46] Schryer NL, Walker LR. *The motion of 180 [degree] domain walls in uniform dc magnetic fields.* J Appl Phys. 1974;45 (12):5406-5421.

[47] Subhankar Bedanta et al. *Supermagnetism.* J Phys D. 2009; 42 (1)013001.

[48] Einstein A. *Investigation on the theory of brownian movement.* New York: Dover; 1956.

[49] Donolato M, Vavassori P, Gobbi M, et al. *On-chip manipulation of protein-coated magnetic beads via domain-wall conduits.* Adv Mater. 2010;22(24):2706.

[50] Kelly PJ, Arnell RD. *Magnetron sputtering: A review of recent developments and applications*, Vacuum. (2000);56(3):159-172.

[51] Martin Y, Wickramasinghe HK. *Magnetic imaging by "force microscopy" with 1000 A resolution*, Appl Phys Lett. (1987) ;50(20):1455-1457.

[52] Kjoller KJ, Prater B, Maivald PG, Heaton MG. *Tapping mode TM imaging: Applications and technology*, Santa Barbara: Digital instruments.

[53] Liptak, Bela G. *Instrument Engineers' Handbook: Process Control and Optimization*, CRC Press. (2005) ISBN 978-0-8493-1081-2.

[54] Digital instruments CP-II user guide.

[55] James B.Pawely, *Handbook of biological confocal microscopy*, Springer, (1995),1,1:632

[56] Allwood DA, Xiong G, Faulkner CC, Atkinson D, Petit D, Cowburn RP. *Magnetic domain-wall logic*, Science. 2005;309(5741):1688-1692.

[57] Ono T, Miyajima H, Shigeto K, Mibu K, Hosoito N, Shinjo T.*Propagation of a magnetic domain wall in a submicrometer magnetic wire.* Science. 1999;284(5413):468-470.

[58] Vavassori P, Metlushko V, Ilic B, et al. *Domain wall displacement in py square ring for single nanometric magnetic bead detection*, Appl Phys Lett. 2008;93(20):203502.

[59] Donolato M, Vavassori P, Gobbi M, et al. *On-chip manipulation of protein-coated magnetic beads via domain-wall conduits.* Adv Mater. 2010;22(24);2706-2710.

[60] Bertacco R, Donolato M, Gobbi M, et al, inventorspatent PCT/EP2010/000879. 2009.

[61] A. Torti, V. Mondiali, A. Cattoni, M. Donolato, E. Albisetti, A. Haghiri-Gosnet, P. Vavassori and R. Bertacco *Single particle demultiplexer based on domain wall conduits* Appl. Phys. Lett 101, 142405, (2012)

[62] M. Donolato, M. Gobbi, P. Vavassori, M. Cantoni, V. Metlushko, B. Ilic, M. Zhang, S. X. Wang and R Bertacco *Nanosized corners for trapping and detecting magnetic nanoparticles*, Nanotechnology 20, 2009, 385501.

[63] M. Donolato, E. Sogne, B. T. Dalslet, M. Cantoni, D. Petti, J. Cao, F. Cardoso, S. Cardoso, P. P. Freitas, M. F. Hansen, and R. Bertacco, *On-chip measurement of the Brownian relaxation frequency of magnetic beads using magnetic tunneling junctions* Appl. Phys. Lett. 98, 073702 (2011).

[64] E. Barborini, I. N. Kholmanov, A. M. Conti, P. Piseri, S. Vinati, P. Milani, C. Ducati, *Supersonic Cluster beam depostion of nanostructured*

Titania, The European Physical Journal Atomic, Molecular, Optical and Plasma Physics June 2003, Volume 24, Issue 1, pp 277-282